FORMING A MORE PERFECT UNION: FABRICATING BIOINSTRUCTIVE SCAFFOLDS TO MIMIC THE OSTEOGENIC NICHE FOR BONE REPAIR

A Dissertation

by

ELI MONDRAGON

Submitted to the Office of Graduate and Professional Studies of
Texas A&M University
in partial fulfillment of the requirements for the degree of

DOCTOR OF PHILOSOPHY

Chair of Committee,	Roland Kaunas
Committee Members,	Sarah Bondos
	Akhilesh K. Gaharwar
	Carl A. Gregory
Head of Department,	Michael McShane

August 2020

Major Subject: Biomedical Engineering

ABSTRACT

Engineered bone graft designs have been largely inspired by adult bone despite significant deviation from the composition of anabolic bone. Highly osteogenic extracellular matrix (ECM) secreted by human mesenchymal stem cells (hMSCs) derived from bone marrow or induced pluripotent stem cells was combined with inorganic bone components from natural (Mg-doped hydroxyapatite) and synthetic (nanosilicates) sources to generate next-generation bone grafts ranging from lyophilized collagen slabs to 3D-printed nanocomposite scaffolds. A drug-eluting system was utilized to stimulate similar levels of the osteogenic ECM as that of previously employed techniques. Furthermore, while direct deposition of the ECM onto scaffolds by cultured hMSCs under static conditions was effective, perfusion culture increased the volumetric distribution of ECM. To provide greater flexibility and simplification to ECM surface modification of scaffolds, metabolically-labeled ECM with azide functional groups was solubilized and covalently tethered to functionalized scaffolds via strain-promoted azide-alkyne cycloaddition (SPAAC). These studies demonstrate a range of approaches to biofabricating grafts using hMSC-derived osteogenic matrices for bone healing.

DEDICATION

To Abraham and Gregoria Mondragon; I could not have asked for better parents.

ACKNOWLEDGEMENTS

I would like to thank my committee chair, Dr. Kaunas, and committee members, Dr. Bondos, Dr. Gaharwar, and Dr. Gregory, for their help and guidance throughout the course of this research. I would also like extend my gratitude to past and current members of the Kaunas Lab for their friendship and for enriching my research experience. Finally, I want to thank my parents and siblings, who supported and encouraged me as I pursued my PhD, despite missing the occasional family event.

CONTRIBUTORS AND FUNDING SOURCES

Contributors

This work was supervised by a dissertation committee consisting of Dr. Roland Kaunas (chair), Dr. Akhilesh K. Gaharwar (member), and Dr. Carl. A. Gregory (member) from the Biomedical Engineering Department, and Dr. Sarah Bondos (member) from the Molecular and Cellular Medicine Department.

The scaffolds presented in Section 2 were fabricated by Dr. Francesca Taraballi, currently an Assistant Professor at Houston Methodist. The drug release profile presented in Section 2 was performed by Dr. Francesca Taraballi.

Funding

Graduate study was funded in part by the TAMU Diversity Fellowship. Graduate research work was funded by the National Institute of Arthritis and Musculoskeletal and Skin Diseases (R01 AR066033 and R21 AR072292), and the National Science Foundation (NSF) Award (CBET 1264848 and 1264832).

TABLE OF CONTENTS

Page

ABSTRACT ii

DEDICATION iii

ACKNOWLEDGEMENTS iv

CONTRIBUTORS AND FUNDING SOURCES v

TABLE OF CONTENTS vi

LIST OF FIGURES ix

LIST OF TABLES xv

1. INTRODUCTION 1

1.1. Non-Union Defects, A Growing Problem 1
1.2. Biology of Bone Development and Fracture Repair 2
1.2.1. Fracture Repair 2
1.2.2. Endochondral and Intramembranous Ossification 2
1.2.3. Post-Natal Bone Growth: Epiphyseal Growth Plate, Grooves of Ranvier, and Appositional Bone Growth 3
1.3. Design Considerations for Engineering Anabolic Bone Grafts 6
1.3.1. Recapitulating the Inorganic Environment of Nascent Bone 6
1.3.2. Recapitulating the ECM of the Anabolic Bone Niche 7
1.3.3. Bioconditioning of Established Scaffolds 8
1.3.4. 3D Printing: An Avenue to Tune Scaffold Microarchitecture 9
1.4. Considerations During Biomanufacturing 11
1.4.1. Stem Cell Source for Production of Anabolic Bone ECM 11
1.4.2. In vitro 3D Culture for Generating Bone Graft Substitutes 12
1.5. Dissertation Overview and Approaches 13
1.5.1. Section 2: Mimicking the Organic and Inorganic Composition of Anabolic Bone 13
1.5.2. Section 3: Clay Nanoparticles in Collagen Nanocomposite Hydrogel Sequester hMSCs Secreted Factors in 3D Microenvironment 14
1.5.3. Section 4: Metabolically Labeled iP-hMSCs Derived Anabolic Bone ECM for Bio-Orthogonal Click Reaction 14

2. MIMICKING THE ORGANIC AND INORGANIC COMPOSITION OF ANABOLIC BONE ENHANCES HUMAN MESENCHYMAL STEL CELL OSTEOINDUCTION AND SCAFFOLD MECHANICAL PROPERTIES 16

2.1. Introduction 16
2.2. Methods 18
2.2.1. Preparation of GW9662-Loaded PLGA/pSi Microspheres 18
2.2.2. Particle Characterization and Evaluation of GW9662 in vitro Release 19
2.2.3. Scaffold Fabrication 19
2.2.4. Structural and Compositional Characterization of Scaffolds 20
2.2.5. Expansion and Seeding of hMSCs 21
2.2.6. Culture in Static and Perfused Conditions 23
2.2.7. Cell Migration on Scaffolds 23
2.2.8. Immunostaining of Deposited Matrix Proteins 24
2.2.9. Gene Expression via Quantitative RT-PCR (qRT-PCR) 25
2.2.10. Microcomputed Tomography (μCT) Analysis of Cultured Scaffolds 26
2.2.11. Uniaxial Compression Test 27
2.2.12. Immunoblotting 27
2.3. Results 28
2.3.1. Morphology and Composition of Scaffolds 28
2.3.2. Cell Number and Infiltration in Static and Perfused Conditions 31
2.3.3. Microsphere Characterization and in vitro release of GW9662 33
2.3.4. Deposition of Anabolic Bone ECM 34
2.3.5. In vitro Osteogenic Differentiation in Osteoinductive Scaffolds 37
2.3.6. In-vitro Mineralization and Scaffold Compressive Strength 39
2.4. Discussion 42
2.5. Conclusion 50

3. CLAY NANOPARTICLES IN COLLAGEN NANOCOMPOSITE HYDROGEL SEQUESTER HMSC SECRETED FACTORS IN 3D MICROENVIRONMENT 51

3.1. Introduction 51
3.2. Methods 53
3.2.1. Cell Culture 53
3.2.2. 2D Cultures Containing nSi and Osteoprotegerin (OPG) ELISA Assay 53
3.2.3. 3D Cultures in Coll-nSi Hydrogels 54
3.2.4. Bioactivity of nSi in Coll and Coll-nSi Hydrogels 55
3.2.5. Alkaline Phosphatase Kinetic Assay and Staining 56
3.2.6. Cell Number Quantification 57
3.2.7. Immunoblotting 58
3.2.8. In vitro Mineralization 59
3.2.9. Physical and Chemical Characterization 60
3.2.10. Metabolically Labeled Proteins and Actin Staining 60
3.3. Results 61

3.3.1. Dose-dependent effects of nSi in hMSC Monolayers 61
3.3.2. Characterization of Collagen-nSil Network 64
3.3.3. Mechanical Characterization 65
3.3.4. Hydrogel Compaction and Actin Staining 67
3.3.5. ALP Activity and Mineralization of hMSCs in 3D Coll-nSi Hydrogels 68
3.3.6. Immunoblotting of BMP2 and Osteopontin 73
3.3.7. Metabolically-Labelled ECM and Secreted Factors 77
3.4. Discussion 81
3.5. Conclusion 90

4. METABOLICALLY LABELED IP-HMSC-DERIVED ANABOLIC BONE ECM FOR BIO-ORTHOGONAL CLICK REACTIONS 92

4.1. Introduction 92
4.2. Methods 94
4.2.1. Synthesis of DBCO-Modified GelMA 94
4.2.2. Fluorescent Labeling of DBCO-GelMA Hydrogels and Swelling Test 96
4.2.3. iP-hMSC Culture and Production of Anabolic Bone ECM 97
4.2.4. Immunoblotting AHA-Modified ECM 99
4.2.5. Immunostaining of AHA-Modified ECM 101
4.2.6. In Gel Detection of AHA-Modified Proteins 102
4.2.7. Bone Marrow Derived hMSCs Cultured on ECM-coated Tissue Culture Plates 103
4.2.8. Alkaline Phosphatase Kinetic and Osteoprotegerin (OPG) ELISA Assays 103
4.2.9. Cell Number Quantification 104
4.3. Results 104
4.3.1. Characterization of DBCO-GelMA Hydrogels 104
4.3.2. Expression of Anabolic Bone ECM 106
4.3.3. Deposition of AHA Incorporated Anabolic Bone ECM 109
4.3.4. AHA Modified Anabolic Bone ECM Retains Osteoinductive Properties 112
4.4. Discussion 113
4.5. Conclusion 119

5. CONCLUSION 121

5.1. Summary of Dissertation and Future Work 121

REFERENCES 125

APPENDIX A 151

A.1 Supplementary Figures and Tables for Section 2 151
A.2 Supplementary Figures and Tables for Section 3 167
A.3 Supplementary Figures and Tables for Section 4 168

LIST OF FIGURES

Page

Figure 1.1: Illustration of adult and growing femur. 4

Figure 1.2: A) Illustration of the epiphyseal growth plate. Reprinted from [21]. B) Comparison of endochondral ossification in the epiphyseal growth plate and fracture calluses. Representative histological sections of a distal femur epiphyseal growth plate and a mid-diaphysial femur fracture at 14 days after injury are presented. Sections were stained with safranin O and fast green, and micrographic images are at 100x magnification. Arrows denote potential sites of interactions with the various tissue types. Reprinted from [15]. 5

Figure 1.3: Effects of decellularization process on the mechanical properties of NICE hydrogels. A) Representative stress–strain response of scaffolds undergoing cyclic compression to 70% strain. B) Analysis on the average compressive modulus and toughness (n = 3, Student's t -test, $p < 0.05$) demonstrated a decrease in response to the decellularization process. Bioconditioned scaffolds upregulate expression of key osteogenic markers. Quantitative RT-PCR analysis showed an increase at the transcription level of C) BMP2, D) osteopontin, and E) osteocalcin was observed after 21 days of culture on bioconditioned scaffolds. Fold changes were normalized to the expression levels of uninduced hMSCs after 8 or 21 days of 2D culture. A one-way ANOVA, followed by a Tukey's multiple comparison test was performed on $\Delta\Delta C_T$ values (* $p < 0.05$). F) After 21 days of culture, calcium content from cultured NICE and bNICE scaffolds were significantly different, with higher mineralization detected on bioconditioned scaffolds. Statistical analysis was performed using Student's t -test (* $p < 0.05$). Reprinted from [59]. 11

Figure 2.1: Morphological characterization of MgHA and MgHA/pSi scaffolds. Representative A) SEM and B) micro-computed tomography (μCT) images of MgHA and MgHA/pSi scaffolds. C) Pore size distribution is shown to be similar between the two scaffolds. D) Specific bone surface ratio and E) percent porosity were unaffected by the addition of drug-eluting microspheres. 29

Figure 2.2: Characterization of the composition of the MgHA and MgHA/pSi scaffolds via TGA A), FTIR B), XRD C), and ICP-MS D). 31

Figure 2.3: A) hMSCs seeding efficiency on scaffolds (n=3). B) Representative cross-sectional images of live-dead staining of hMSCs after 8 days of culture in MgHA scaffolds in static and perfused conditions, with direction of flow

indicated by the white arrow. C) Average depth at which stacked live-dead images decreased to 50% of maximum fluorescence intensity (Student's t-test, * $p<0.05$, n=3, error bars depict standard deviation). D) hMSCs population, as quantified by GAPDH expression via qRT-PCR, shows significant increase in cell number in response to perfusion in various scaffold and culture media combinations. Statistical testing was performed by two-way ANOVA, followed by a Tukey's multiple comparison between all scaffold/media combinations. Columns with matching letters indicate the comparison was not significant. ($p<0.05$, n=3, error bars depict standard deviation). 32

Figure 2.4: A) Confocal imaging of FITC-labeled PLGA/pSi show pSi are uniformly distributed within PLGA spheres. B) Cumulative release of GW9662 from PLGA/pSi microspheres show controlled release of GW9662 up to 21 days (n=3, error bars depict standard deviation). 33

Figure 2.5: qRT-PCR analysis for the expression of anabolic bone ECM components. A) Coll VI and B) Coll XII relative fold expression in hMSCs after 8 days of culture in various scaffold/media combinations. Columns with matching letters indicate all possible comparisons were not significant (n=3, error bars depict standard deviation, $p<0.05$, two-way ANOVA, Tukey's multiple comparison test). 35

Figure 2.6: Immunostaining of Coll VI A-F) and XII G-L) after 8 days under static and perfused conditions for various scaffold/culture media combinations reveals similar levels of matrix deposition between GW-pSi and GW-media. Perfusion increased matrix deposition in all scaffold and culture media combinations relative to their static counterparts. 36

Figure 2.7: qRT-PCR analysis for the expression of osteogenic markers in hMSCs after A) and B) 8 days or C) and D) 21 days of culture in various scaffold/media combinations. Fold changes were normalized to the expression levels of uninduced hMSCs after 8 or 21 days of 2D culture. Columns with matching letters indicate all possible comparisons were not significant. (n=3, error bars depict standard deviation, $p<0.05$, two-way ANOVA, Tukey's multiple comparison test). 38

Figure 2.8: A-F) Representative μCT reconstructions of scaffolds after 21 days of culture (scale bar 500 μm). G) Bone mineral density increases in response to both perfusion and GW9662. Columns with matching letters indicate all possible comparisons were not significant (n=3, error bars depict standard deviation, $p<0.05$, two-way ANOVA, Tukey's multiple comparison test). 40

Figure 2.9: A-C) Representative compressive tests of scaffolds after 21 days of culture. D) Average compressive modulus of scaffolds after 21 days of

culture. Columns with matching letters indicate all possible comparisons were not significant (n=3, error bars depict standard deviation, $p<0.05$, two-way ANOVA, followed by Tukey's multiple comparison test). E) High degree of correlation between observed bone mineral density and compressive modulus for the compiled 18 samples (Pearson's correlation r value of 0.695, $p<0.05$). 41

Figure 3.1: A) Fabrication of Collagen-nSi (Coll-nSi) nanocomposite hydrogels. Three different precursor hydrogel solutions with varying nSi percentage were pipetted into silicone mold seated on a silicone sheet (white arrow indicates dried collagen used for anchoring). B) Illustration of the four different culture condition; half of hMSCs cultures were pretreated with nSi, while half of the gels were kept in the silicone mold as a mechanical support. 56

Figure 3.2: Effects of nSi treatment on hMSCs in monolayer culture. A) hMSCs population over 8 days of osteogenic culture. B) OPG secreted by hMSCs over 8 days of osteogenic culture. C) Immunoblotting against BMP2 of hMSCs lysates after 8 days of culture (left) and normalized band signals (right). D) Representative images of ALP-stained monolayers after 8 days of osteogenic culture. E) ALP activity after 8 days of osteogenic culture in monolayer. F) Representative ARS-stained hMSCs monolayers after 21 days of osteogenic culture. E) Spectrophotometric quantification of recovered ARS staining. Statistical testing was performed by one-way ANOVA, followed by a Tukey's multiple comparison. Asterisks depict statistically significant (n=3, error bars depict standard deviation). 63

Figure 3.3: Chemical and rheological characterization of Coll-nSi nanocomposite hydrogels A) FTIR analysis of lyophilized nanocomposite hydrogels indicate presence of both protein (amides 3300 cm^{-1}, 1650 cm^{-1}, 1530 cm^{-1}, and 1250 cm^{-1}) and nSil (~1000 cm^{-1}). B) Confocal reflectance reveals nSil are heterogeneously distributed in collagen gels and disrupt fibril microstructure (scale bar 50 μm). Representative data shown for C) strain sweep and E) frequency sweeps. D) Average yield strain for the collagen and collagen-nSi hydrogels defined as a 10% deviation in G'. F) Average storage modulus Statistical testing was performed by one-way ANOVA, followed by a Tukey's multiple comparison. Asterisks depict statistically significant (n=3, error bars depict standard deviation). 66

Figure 3.4: A) Representative images of hydrogels with and without silicone support after 4 days of culture. B) Quantified hMSCs-mediated compaction of hydrogels cultured without silicone support determined by changes in area. Statistical testing was performed by one-way ANOVA within individual days, followed by a Tukey's multiple comparison (n=3, error bars depict

standard deviation, $p<0.05$). C) Hydrogel compaction results in arched stress fibers in collagen and 0.1% nSi hydrogels. hMSCs cultured in the 1% nSi hydrogels without the use of the silicone support did not have the arched stress fibers. D) hMSCs alignment is observed in silicone-supported gels; crimped stress fibers no present. 68

Figure 3.5: A) ALP activity of hMSCs after 8 days of 3D culture. B) Calcium content after 21 days of 3D culture. For ALP activity and calcium content, statistical analysis was performed by three-way ANOVA, followed by a Tukey's multiple comparison test (n=3). Error bars depict standard deviation. Four types of comparisons are emphasized in the figure and were assigned unique symbols when a significant difference ($p<0.05$) was discovered. These include: * when comparing gels with varying nSi percentage within the same culture condition, # when comparing to the culture condition without silicone support and no pretreatment, ¶ when comparing to the culture condition with the silicone support and no pretreatment, and ‡ when comparing to the culture condition pretreated with nSi but lacking silicone support. The comparisons between culture conditions (#, ¶, ‡) was performed between gels of the same Coll-nSi formulation. 70

Figure 3.6: Immunoblotting against BMP2 after 8 days of 3D culture in Coll and Coll-nSIl hydrogels A) without the silicone support or nSi pretreatment, B) with silicone support and no nSi pretreatment, C) without silicone support and nSi pretreatment, and D) with both silicone support and nSi pretreatment; corresponding densiometric analysis are shown on the right. Two distinct isoforms of BMP2 were detected (46 kDa, 13 kDa), which were consistently upregulated in the Coll-1% nSi hydrogels. Statistical analysis was performed by one-way ANOVA within each BMP2 isoform, followed by a Tukey's multiple comparison. Error bars depict standard deviation (n=3), and asterisks signify a significant difference ($p<0.05$). 74

Figure 3.7: Immunoblotting against osteopontin (OPN) after 8 days of 3D culture in Coll and Coll-nSi hydrogels A) without the silicone support or nSi pretreatment, B) with silicone support and no nSi pretreatment, C) without silicone support and nSi pretreatment, and D) with both silicone support and nSi pretreatment. Three distinct isoforms of OPN were detected (72 kDa, 40 kDa, and 32 kDa), which were consistently upregulated in the Coll-1% nSi hydrogels. E-H) Corresponding densiometric analysis of the bands. Statistical analysis was performed by one-way ANOVA within each Osp isoform, followed by a Tukey's multiple comparison. Error bars depict standard deviation (n=3), and asterisks signify a significant difference ($p<0.05$). 76

Figure 3.8: Visualization of metabolically-labeled intra- and extracellular proteins after 4 (left column) and 8 (middle and right column) days of 3D culture using fluorophore-conjugated DBCO (DBBCO-488) propidium iodide. Representative images of proteins and hMSCs encapsulated in A) Coll hydrogels, B) Coll-0.1% nSi, and C) Coll-1%nSi nanocomposites. White arrows indicate visible extracellular vesicles, red arrows indicate location of nSi, teal arrows indicate cell body, and purple arrow points to secreted ECM. 78

Figure 3.9: A) Representative images of acellular and hMSCs-laden Coll-1% nSi nanocomposites indicate an increase in metabolically-labelled proteins sequestered by nSi with increasing culture time. B) Quantification of fluorescence intensities of metabolically-labeled proteins on nSi confirmed significant increase in protein-nSi tethering with culture time (Kruskal-Wallis non parametric test, followed by Dunn's multiple comparison test, * $p<0.05$). C) Metabolic labelling of secreted proteins after 4 (top row) and 8 (bottom) days of 3D culture in Coll-1% nSi nanocomposites. Red arrows indicate woven structure of metabolically-labeled ECM, while white arrows indicate regions with dense fibrillar mesh in collagen network. 80

Figure 4.1: A) Schematic illustrating the development iP-hMSC derived AHA-ECM. The methionine analogue added to culture media is metabolically incorporated into the anabolic bone ECM over the course of 10 days, after which it is decellularized. B) GelMA hydrogels functionalized with the DBCO moiety (DBCO-PEG-Sulfo-Amine) through EDC/NHS chemistry. C) Anabolic bone ECM covalently tethered to DBCO-GelMA hydrogels through strain-promoted azide-alkyne cycloaddition. D) BM-hMSCs will be seeded on ECM-coated GelMA hydrogels and evaluated for in vitro osteogenic differentiation after 21 days of culture. 98

Figure 4.2: Fluorescent labeling of DBCO-GelMA hydrogels. A) Photopatterned DBCO-GelMA^{BC} hydrogel in GelMA. B) Fluorescently labeled DBCO-GelMA^{BC} and DBCO-GelMA^{AC} with an azide-488 tag. GelMA hydrogels modified by EDC/NHS chemistry used as a control (Scale bar 1 cm). C) Degree of DBCO functionality on DBCO-GelMA^{BC} and DBCO-GelMA^{AC} hydrogels approximated by their relative fluorescent intensity. GelMA hydrogels modified by EDC/NHS chemistry used as a control. Statistical analysis was performed by one-way ANOVA, followed by a Tukey's multiple comparison. Error bars depict standard deviation (n=3), and asterisks signify a significant difference ($p<0.05$). 106

Figure 4.3: Immunoblotting against Coll VI and XII after 10 days of culture for A) intracellular and C) extracellular protein fractions. B) and D) Corresponding densiometric analysis are shown on the right. E) Cumulative band intensity

for intracellular and extracellular protein fractions. F) Protein content of iP-hMSCs monolayers after 10 days of culture. Statistical analysis was performed by one-way ANOVA within insoluble and soluble fractions, followed by a Tukey's multiple comparison. Error bars depict standard deviation (n=3), and asterisks signify a significant difference ($p<0.05$). 108

Figure 4.4: iP-hMSCs uptake and incorporate AHA into deposited ECM. Representative images of iP-hMSCs monolayers after 10 days of culture in the presence of 0, 100, and 300 μM of AHA and 10 μM of GW9662. Monolayers were labeled with DBCO-488 fluorescent tag, counterstained with DAPI, and either A) Coll VI or C) Coll XII. Cyclo-addition reaction between DBCO and AHA-containing proteins was performed. Red squares indicate bone-line nodules. The corresponding B) and D) mean fluorescence intensity for the DBCO-stained monolayers are shown on the right. Statistical analysis was performed by one-way ANOVA on the mean fluorescence of the DBCO-stained monolayers, followed by a Tukey's multiple comparison. Error bars depict standard deviation (n=4), and asterisks signify a significant difference ($p<0.05$).....111

Figure 4.5: Inclusion of AHA into the anabolic bone ECM does not interfere with osteoinductive properties of the ECM. Bone marrow derived hMSCs cultured on tissue culture plates coated with standard and AHA-modified ECM show comparable A) ALP activity and B) OPG secretion. ECM derived from GW9662 treated cells accelerates expression of early osteogenic markers. Columns with matching letters indicate all possible comparisons were not significant. (n=3, error bars depict standard deviation, $p<0.05$, two-way ANOVA, Tukey's multiple comparison test).....113

LIST OF TABLES

Page

Table 2.1: Scaffold composition and cultured media used for osteogenic assays. All possible permutations of scaffold/media formulations were cultured in both static and perfused conditions. 22

1. INTRODUCTION

1.1. Non-Union Defects, A Growing Problem

Approximately 15.3 million fractures receive treatment annually in the United States, 5-10% of which will require additional surgical intervention due to delayed or non-union[1] . Due to age-related comorbidities, people over the age of 65 are not only at an increased risk for fracture[2,3], but are also more likely to experience non-union[3]. The leading surgical intervention in functionally restoring damaged bone in these cases has been the use of bone grafting material[4,5]. Although autologous bone grafts, or autografts, are largely considered the gold standard, limited grafting material and donor-site morbidity are well documented limitations[4–6]. Allografts, or donor bone tissue, provide an alternative bone graft material. Allografts are heavily manipulated (e.g. decellularized, freeze dried, irradiated) to reduce disease transmission, and are available in various forms, e.g. demineralized bone matrix (DBM), cancellous cuboid blocks or chips, and cortical struts[7]. However, a reduction in the osteoinductive, osteogenic, and mechanical properties[5,7,8] of allografts is likely responsible for the longer healing time and higher revision rates[6] compared to autografts. Furthermore, the supply of donated cadaveric allograft material has not kept up with the increase in bone grafting procedures performed in the United States[8]. Understandably, there has been extensive work in developing bone graft substitutes and optimizing their osteoregenerative outcome. Engineered bone graft approaches have relied heavily on mimicking key compositional and physical properties of adult homeostatic bone[9,10]. Unfortunately, this approach has failed to yield an

engineered bone graft with the regenerative potential equal to that of autologous bone grafts.

1.2. Biology of Bone Development and Fracture Repair

1.2.1. Fracture Repair

Recently, "developmental engineering" or drawing inspiration from developmental biology, has emerged as new approach in designing engineered tissues[11]. Unlike most adult tissues, bone has the capacity to undergo true regeneration, returning to a pre-injury without a fibrous scar[12]. This is has been attributed to the fact that bone repair recapitulates several ontological events that occur during both skeletal development and post-natal bone growth[12,13]. For example, during the anabolic phase of bone repair, a cartilaginous callus tissue is deposited by recruited progenitor cells[12,14]. The de-novo tissue undergoes extensive remodeling and mineralization akin to both embryonic endochondral and intramembranous ossification[12,14,15]. An understanding of the anabolic microenvironment and the mechanisms governing these processes in bone development and in fracture repair is thus expected to inform the designing of novel bone repair therapies.

1.2.2. Endochondral and Intramembranous Ossification

Despite the large diversity in bone size and shape, the development of bones occur through either endochondral or intramembranous ossification[16]. Flat bones, e.g craniofacial bones, develop via intramembranous ossification, while long bones in limbs develop via endochondral ossification[13,16]. In intramembranous ossification, mesenchymal cells migrate and condense at the appropriate location, and differentiate directly to osteoblasts. These in turn deposit a rich ECM template that is subsequently mineralized[16].

Analysis of the mineral content of rat calvaria, which undergoes intramembranous ossification, at different developmental stages revealed unique, non-stoichiometric HA with ionic substitutions in the earlier stages[17]. Regarding the ECM content, rare collagens, e.g. collagen type XII (Coll XII), have been found to regulate the organization and osteogenic potential of progenitor cells in the periosteum[15]. This would implicate the importance of Coll XII in the formation of the periosteal callus "shell", an intramembranous ossification process[15]. Similarly, collagen type VI Coll VI), have been in the primary osteons of the femoral diaphysis, which are constructed via intramembranous ossification during growth periods[18]

For endochondral ossification, the condensed mesenchymal cells differentiate into chondrocytes that deposit an avascular, hyaline ECM template that is gradually remodeled and mineralized[15]. The extensive remodeling, mineralization, vascularization of the cartilage template is accomplished by coordinated efforts of recruited osteoclasts, osteoblasts, and endothelial cells, respectively. Rare collagens have also been found to play a crucial role during endochondral ossification. For example, Coll VI has been found to regulate trabecular bone structure[19].

1.2.3. Post-Natal Bone Growth: Epiphyseal Growth Plate, Grooves of Ranvier, and Appositional Bone Growth

Post-natal bone growth in the epiphyseal growth plate strongly resembles fetal endochondral ossification. Long bones consist of the diaphysis in the center, epiphysis at both ends, and the metaphysis region in between (**Figure 1.1).**

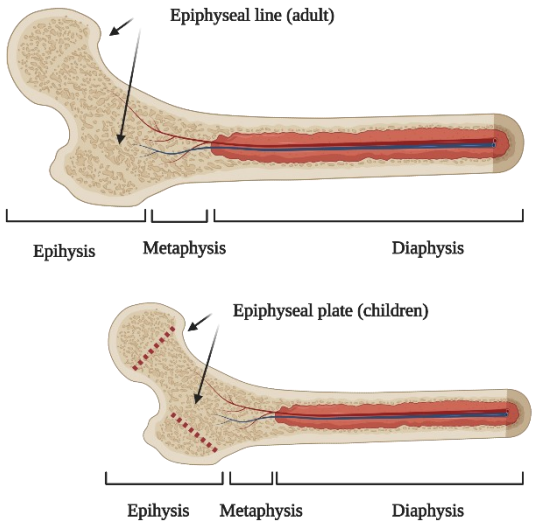

Figure 1.1: Illustration of adult and growing femur.

The epiphyseal growth plates, responsible for growth in childhood/adolescence, are layers of cartilage tissues sandwiched between the epiphysis and diaphysis[13]. Elongation of long bones is driven by the proliferation and hypertrophy of chondrocytes and their ECM deposition in regions near the epiphysis[20,21]. Older ECM closest to the metaphysis is subsequently mineralized and replaced by trabecular bone by osteoblasts origination from the metaphysis[20] (**Figure 1.2**). The groove of Ranvier (GOR), is a perichondrial ossification layer surrounding the epiphyseal growth plate[22,23]. To accommodate the growth of the epiphyseal growth plate, catabolic (bone resorption) and anabolic (bone forming) processes occur in the inner and outer layer, respectively, of GOR[22,23]. High expression of unique collagens, e.g. Coll VI , have been reported in the

middle layer of the Groove of Ranvier, and are reported to play a regulatory role in pre-osteoblasts maturation[24]. Similarly, appositional bone growth (thickening) in the diaphysis of long bones, is a post-natal process that involves the coordinated removal of bone from the lining the medullar cavity by osteoclasts and osteoblast-mediated thickening on the outer surface[25].

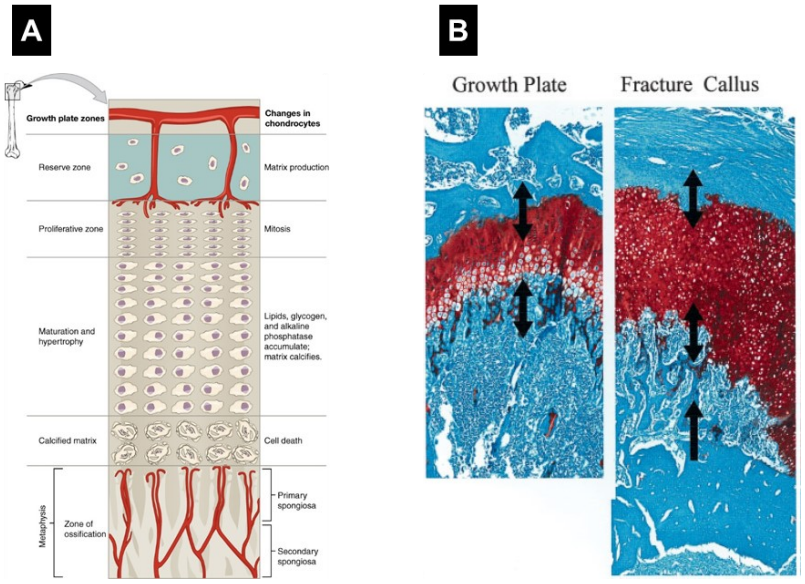

Figure 1.2: A) Illustration of the epiphyseal growth plate. Reprinted from [21]. B) Comparison of endochondral ossification in the epiphyseal growth plate and fracture calluses. Representative histological sections of a distal femur epiphyseal growth plate and a mid-diaphysial femur fracture at 14 days after injury are presented. Sections were stained with safranin O and fast green, and micrographic images are at 100x magnification. Arrows denote potential sites of interactions with the various tissue types. Reprinted from [15].

1.3. Design Considerations for Engineering Anabolic Bone Grafts

1.3.1. Recapitulating the Inorganic Environment of Nascent Bone

Inspired by the inorganic composition of native bone tissue, ceramics have been used as void fillers[7], coatings for fixation devices[26,27], and as vehicles for drug delivery[28]. With a chemical composition similar to the mineral phase of bone, calcium phosphate-based ceramics are an attractive bone substitute, e.g. hydroxyapatite[29,30], tricalcium phosphates[31]. Synthetic HA possess excellent osteoconductive properties, but can be slower to resorb than their endogenous counterparts due to relatively high Ca/P ratio and crystallinity[28]. In contrast, tricalcium phosphate ($Ca_3(PO_4)_2$) ceramics are resorbed faster[32], and have been employed as resorbable screws for fracture fixation[33].

Although HA is typically depicted stoichiometrically as $Ca_{10}(PO_4)_6(OH)_2$, cationic and anionic substitutions in the crystalline structure of biological HA have been reported[34]. For example, Zn^{2+}, Mn^{2+}, Mg^{2+} may substitute for Ca^{2+}, HPO_4^{2-} and CO_3^{2-} may substitute for PO_4^{3-}, and CO_3^{2-}, Fl^-, Cl^- for may substitute OH^-. In addition, the nonstoichiometric biological HA has a CA/P ratio below many synthetic HA (~1.67)[35,36]. Interestingly, these ionic substitutions are more common in recently ossified bone tissue in fracture calluses and in developing bone[17,37]. For example, Mg^{2+} is the most abundant cationic substitution in bone during development and repair, at about 5-6% molar ratio[34]. It is surmised that nascent biological HA consists of a relatively stable apatite core surrounded by the more reactive, non-stoichiometric domain[35,36]. At the superficial hydrated layer, reversible exchange of ions occurs with the possible cations (Zn^{2+}, Mn^{2+}, Mg^2) and anions (HPO_4^{2-} and CO_3^{2-} Fl^-, Cl^-). As the bone mineral matures, however, it contains less ionic

substitutions and its composition resembles more to that of the stoichiometric HA[35,36]. The existence of a labile and reactive surface in HA allows partially mineralized nascent bone (e.g. ossified fracture callus) to be easily remodeled during bone development and repair. The effects of these ionic substitutions on HA stability and on osteogenic differentiation have been investigated in both *in vivo*[34] and *in vitro*[38]. Generally, an increase the dissolution of ions is observed in ion-substituted HA[38], confirming the in-vivo results of higher resorption rates. Specifically, Mg-substituted HA granules were shown to have superior osteoconductivity and higher resorption rate compared to stoichiometric HA granules[34]. Thus, recapitulating the inorganic composition of nascent bone may be a key design parameter in development of new scaffolds for bone repair.

1.3.2. Recapitulating the ECM of the Anabolic Bone Niche

Native ECM is a highly hydrated network of soluble and insoluble proteins, and polysaccharides, that regulate cellular adhesion, migration, proliferation, and differentiation[39]. While collagen type I is a major component of the organic phase of homeostatic bone, there are a number of other collagen types that are found in relative abundance in embryonic and regenerating bone that play a major regulatory role[24,40–43]. For example, Coll XII is abundantly present in both cortical and trabecular regions of developing femurs[42,43]. In transgenic Coll XIIα1 -/- mice, significant reductions in femur length/thickness, cortical bone mass, and long bone mechanical properties compared to wild-type controls were observed[43]. In addition, Coll XII regulates osteoblastic terminal differentiation as well as their organization polarity in the periosteum[43]. Coll VI is highly expressed in the primary osteons of the femoral diaphysis, where it supports the

proliferation and maturation of pre-osteoblasts[18]. Coll VI is also highly expressed in the middle layer of the Groove of Ranvier , and helps regulate the differentiation of pre-osteoblasts prior to maturation[24]. Thus, Coll VI and Coll XII could be leveraged to mimic the anabolic bone niche in engineered tissues.

Previous work from our collaborator has shown that the propensity of human mesenchymal stem cells (hMSCs) to differentiate into osteoblasts can be accelerated by inhibiting peroxisome proliferator activating receptor-γ (PPARγ) with the antagonist GW9662[44,45], during which cells generate an anabolic bone extracellular matrix (ECM) rich in Coll VI and XII. The purified anabolic bone ECM has shown a remarkable capacity to regenerate bone even when administered to lesion sites without hMSCs[45]. However, a lack of structural form does limit its practicality for bone repair.

1.3.3. Bioconditioning of Established Scaffolds

Direct deposition of the anabolic bone ECM onto established scaffolds ("biocondition") has been explored as a means to imbue structural form to the anabolic bone ECM. For example, gelatin foam scaffolds bioconditioned with the anabolic bone ECM was shown to accelerate bone healing in mice[46,47]. Similar strategies (cell-to-scaffold ECM deposition) have been employed by others on alloplastic[48,49] and metallic implants[50,51]. These materials are either non-resorbable or have slow degradation rates (~years), and are unable to be incorporated and replaced by newly formed bone. A bone graft substitute would ideally be biodegradable, with a rate of degradation similar to the rate of bone deposition and integration. However, the devitalization methods employed on bioconditioned scaffolds can be detrimental to scaffold properties. Thus, a technique that

allows established biodegradable scaffolds, to be functionalized with this anabolic bone ECM without undergoing the decellularization process could facilitate its translation to clinical use.

1.3.4. 3D Printing: An Avenue to Tune Scaffold Microarchitecture

Biomimetic approaches entail mimicking not only the composition of the tissue of interest but the architecture as well. The majority of synthetic bone graft substitutes have aimed to replicate the highly porous architecture of cancellous (trabecular) bone[7]. In addition to supporting cellular viability and encouraging a homogenous distribution of seeded cells *in-vitro*, an interconnected pore network enhances tissue ingrowth and vascularization *in-vivo* [52]. Pore diameter between 100-300 μm have been found to be ideal to encourage both vascularization and endochondral ossification[53]. Common techniques to establish porosity include particle leaching, freeze-drying, and gas foaming[54].

Recent developments in additive manufacturing provide an opportunity to design and 3D print scaffolds with tunable architectures[55]. Our collaborator has recently introduced a new class of hydrogel ink, Nanoengineered Ionic-Covalent Entanglement (NICE), capable of printing high aspect ratio structures with high fidelity thanks a dual reinforcement strategy utilizing two interpenetrating polymer networks (IPN) with Laponite nanosilicates (nSi)[56]. Laponite, a synthetic 2D nanosilicate (nSi), are a particularly exciting class of nanomaterial as they not only modulate rheological properties of hydrogels, but have also been shown to induce osteogenic differentiation in bone marrow hMSCs[57,58] and adipose-derived MSCs[59] in 2D culture. However, the mechanism by which nSi impart their osteoinductive influence in 2D culture has not been

entirely characterized, less so in 3D culture. We have recently augmented the osteoinductive ability of 3D printed NICE scaffolds by depositing the an anabolic bone ECM on the surface of the scaffolds[60]. Despite a robust increase in the expression of osteogenic markers (**Figure 1.3C-E**) and mineralization (**Figure 1.3F**), the decellularization process was shown to have a deleterious effect on mechanical properties of the bioconditioned 3D-printed scaffold (**Figure 1.3A-B**)[60]. Thus, a technique that allows established biodegradable scaffolds to be functionalized with this anabolic bone ECM without undergoing the decellularization process could facilitate translation to clinical use.

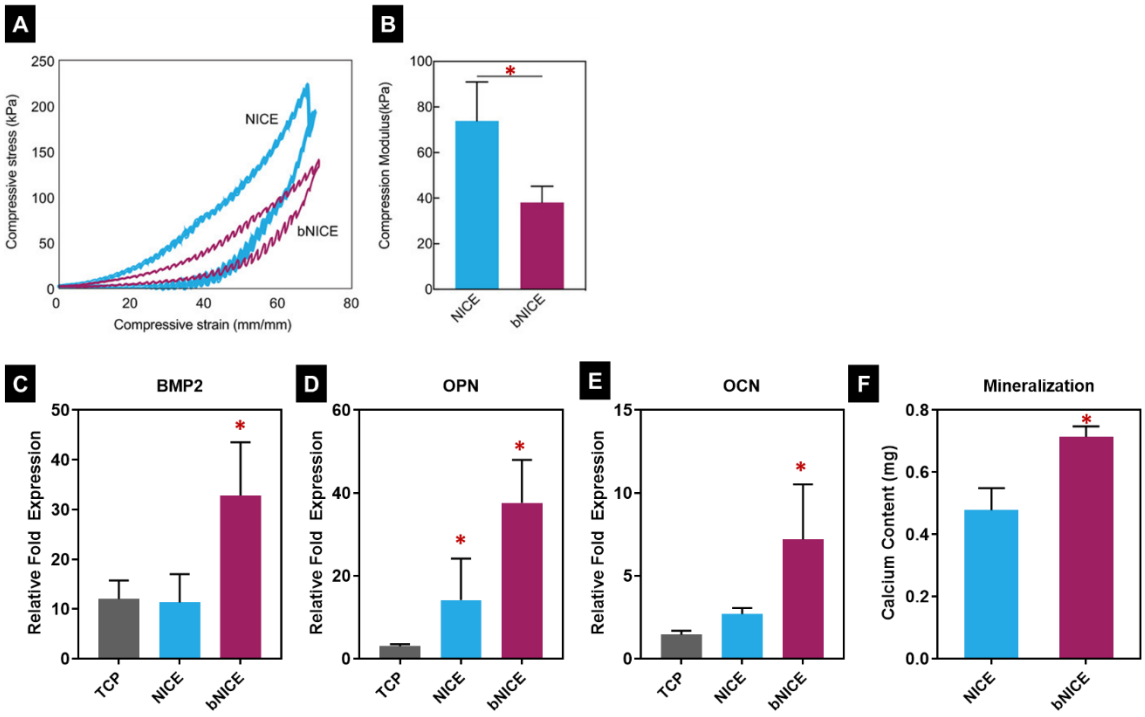

Figure 1.3: Effects of decellularization process on the mechanical properties of NICE hydrogels. A) Representative stress–strain response of scaffolds undergoing cyclic compression to 70% strain. B) Analysis on the average compressive modulus and toughness (n = 3, Student's t -test, $p < 0.05$) demonstrated a decrease in response to the decellularization process. Bioconditioned scaffolds upregulate expression of key osteogenic markers. Quantitative RT-PCR analysis showed an increase at the transcription level of C) BMP2, D) osteopontin, and E) osteocalcin was observed after 21 days of culture on bioconditioned scaffolds. Fold changes were normalized to the expression levels of uninduced hMSCs after 8 or 21 days of 2D culture. A one-way ANOVA, followed by a Tukey's multiple comparison test was performed on $\Delta\Delta C_T$ values (* $p < 0.05$). F) After 21 days of culture, calcium content from cultured NICE and bNICE scaffolds were significantly different, with higher mineralization detected on bioconditioned scaffolds. Statistical analysis was performed using Student's t -test (* $p < 0.05$). Reprinted from [59].

1.4. Considerations During Biomanufacturing

1.4.1. Stem Cell Source for Production of Anabolic Bone ECM

The regenerative success of autologous bone grafts has been partially attributed to the delivery of progenitor cells. As a result, stem cells of various sources and potency have been explored for the fabrication of bone grafts. Bone marrow derived hMSCs, in

particular, have been heavily utilized for bone engineering purposes as they are functionally involved in bone development and fracture repair[61]. Bone marrow derived hMSCs can be easily isolated from marrow aspirate as they are capable of adhering and growing on tissue culture plates[62]. Despite their benefits, bone marrow hMSCs are constrained by their limited long-term proliferative ability[63,64], high degree of heterogeneity[65,66], a decrease in osteogenic potential with successive population doublings[67] and increasing age[68]. For the purpose of developing clinically-relevant engineered bone tissues in a biomanufacturing setting, a stem cell line should be highly proliferative with low risk of senescence and tumorigenicity. Human induced pluripotent stem cell-derived mesenchymal stem cells (iP-hMSCs) meet these criteria. Unlike donor-derived hMSCs, undifferentiated induced human pluripotent stem cells (iPSCs) can divide without senescence until they are differentiated into iP-hMSCs[69], providing a theoretically limitless supply of reproducible biomaterial for the production of the anabolic bone matrix. This provides a potential strategy to produce large quantities of the anabolic bone ECM generated from a genetically identical source of iP-hMSCs in a reproducible manner.

1.4.2. In vitro 3D Culture for Generating Bone Graft Substitutes

A major translational hurdle in the development of viable bone grafts for clinical applications has been poor gas and nutrient transport to inner regions of 3D scaffolds, limiting the viability and migration of implanted progenitor cells into scaffolds[70]. Although designing porous scaffolds can improve viability and cell migration, poor cell distribution can be an issue at seeding. As a result, a variety of bioreactors have been

developed to improve the mass transport, e.g. stirred flasks, rotating bioreactors, perfusion bioreactors. Both stirred flasks and rotating bioreactors can enhance mass transport near the surfaces of cultured tissue constructs. Mass transport to the core regions are still governed by diffusion in these systems, and dense cell layers near scaffold surfaces is not uncommon, even in highly porous scaffolds[71–73]. In perfusion bioreactors, culture media flows through the interconnected pores of the scaffolds, resulting in improved gas and nutrient transport[74,75]. Culture under these conditions results in improved cellular distribution[76], increase in ECM deposition[75], as well as improved osteogenic differentiation of seeded progenitor cells[74]. However, pore architecture (e.g. size distribution) may result in preferential flow paths, leading to inhomogeneous cellular distribution[77]. A perfusion bioreactor that encourages homogenous cellular distribution and augments the deposition of the anabolic bone ECM would be vital for the production of clinically relevant engineered bone grafts.

1.5. Dissertation Overview and Approaches

1.5.1. Section 2: Mimicking the Organic and Inorganic Composition of Anabolic Bone

Biomimetic approaches to designing engineered bone grafts have been largely inspired by adult bone despite functionally significant differences from the composition of anabolic bone in both the mineralized and non-mineralized fractions. In this section, a previously reported[78] biologically inspired osteoinductive scaffold—a macroporous collagen scaffold coated with Mg-doped HA (Coll/MgHA)—was used as a launching point. To mimic the organic fraction of nascent bone, hMSCs were stimulated with

GW9662 to deposit Coll VI and Coll XII through either supplemented media or via composite microspheres embedded in the scaffolds for localized delivery. Furthermore, hMSCs and scaffolds were cultured in both static and perfuse conditions to investigate the interaction between GW9662 treatment and perfusion and their effects on ECM deposition trends. The work presented here will show perfusion culture enhanced deposition of Coll VI and Coll XII, as well as osteogenic differentiation. In addition, local delivery of GW9662 with drug-eluting microspheres had comparable effects to systemic delivery in the perfusate.

1.5.2. Section 3: Clay Nanoparticles in Collagen Nanocomposite Hydrogel Sequester hMSCs Secreted Factors in 3D Microenvironment

In this section, I investigate the mechanism by which nSi induce osteogenic differentiation of hMSCs in a collagen-nSi (Coll-nSi) nanocomposite hydrogel. I will demonstrate that while matrix stiffening and nSi internalization does influence the osteogenic differentiation of hMSCs in 3D culture, a strong interaction between nSi and the hMSCs secretome in the extracellular space could be playing a larger, more significant regulatory role.

1.5.3. Section 4: Metabolically Labeled iP-hMSCs Derived Anabolic Bone ECM for Bio-Orthogonal Click Reaction

Here, we report an approach for covalently tethering the anabolic bone ECM onto established scaffolds. A significant drawback to using hMSCs to produce the anabolic bone ECM is their limited proliferation potential and variability in cell behavior between donors. In addition, the process of bioconditioning established scaffolds requires

decellularization, which has been proven to be detrimental to mechanical properties of established scaffolds. To address these limitations, hMSCs generated from human induced pluripotent stem cells (iP-hMSCs) were instead utilized to produce the anabolic bone ECM. Further, azide functionality was metabolically incorporated into iP-MSCs-derived ECM, so to it could participate in a strain-promoted azide-alkyne cyclo addition (SPACC). Gelatin-methacryloyl (GelMA) hydrogels were functionalized with dibenzocyclooctyne (DBCO), which can participate in SPAAC chemistry. In this section I will demonstrate that azide iP-hMSCs-derived ECM can be fabricated with azide-functional groups that partake in SPAAC click reaction without negatively impacting the ECM composition. Furthermore, I will demonstrate that a GelMA, a well-established hydrogel, can be modified with DBCO and participate in SPAAC click reaction. These results provide evidence of the feasibility of covalently tethering metabolically labeled ECM to hydrogels via a copper-free click reaction.

2. MIMICKING THE ORGANIC AND INORGANIC COMPOSITION OF ANABOLIC BONE ENHANCES HUMAN MESENCHYMAL STEL CELL OSTEOINDUCTION AND SCAFFOLD MECHANICAL PROPERTIES *

2.1. Introduction

Bone repair recapitulates several ontological events that occur during both skeletal development and post-natal bone growth[12,13]. The anabolic environment is characterized by the recruitment of progenitor cells and the deposition of *de-novo* tissue that undergoes extensive remodeling[12–15]. While collagen type I is a major component of the organic phase of homeostatic bone, there are a number of other collagen types that are found in relative abundance in embryonic and regenerating bone[40–42]. Collagen types VI (Coll VI) and XII (Coll XII) are upregulated in developing bone, where they play crucial roles in regulating bone growth[18,24,42]. Furthermore, approximately 70% of the dry weight of mature bone is composed of impure, low crystallinity hydroxyapatite (HA). Although HA is typically depicted stoichiometrically as $Ca_{10}(PO_4)_6(OH)_2$, cationic and anionic substitutions in the crystalline structure are quite common[34]. Specifically, Mg^{2+} is abundant in bone during the initial phases of osteogenesis and disappears in mature bone[34]. Despite the known differences in composition between anabolic and homeostatic bone,

* This chapter has been adapted from Mondragon *et al*. Mimicking the Organic and Inorganic Composition of Anabolic Bone Enhances Human Mesenchymal Stem Cell Osteoinduction and Scaffold Mechanical Properties. *Frontiers of Bioengineering and Biotechnology* **8,** 753 (2020) in accordance with the Creative Commons Attribution 4.0 International (CC BY 4.0) license.

engineered bone grafts have not previously been designed to resemble both the organic and inorganic composition of regenerating bone.

Cationic (e.g. Zn^{2+}, Mn^{2+}, Mg^{2+}) and anionic (e.g. CO_3^{2-}, Fl^-, Cl^-, SiO_4^{4-}) substitutions in the lattice structure of bone mineral have motivated the development of a wide range of ion-substituted HA for bone repair[79]. Among these ions, Mg is unique in that it is relatively abundant in bone during development and repair. Mg-containing biomaterials have shown promise when applied to bone repair. Mg-based ceramics enhanced the osteogenic[80] and resorption properties of scaffolds[81]. In fracture fixation, Mg stimulated new bone formation when incorporated into degradable screws and plates[82]. However, tailoring the mineral content of scaffolds can only recapitulate the inorganic fraction of the anabolic niche.

ECM deposited by rat mesenchymal stem cells (MSCs) onto titanium mesh[83] or human MSCs (hMSCs) onto tissue culture plastic[49] promote osteogenic differentiation of freshly seeded MSCs. We have developed a protocol that uses GW9662, a PPAR-γ inhibitor, to induce osteogenic differentiation of hMSCs, during which time the cells generate an ECM rich in Coll VI and XII[45,46]. Depositing this ECM onto gelatin foam followed by decellularization results in a graft that accelerates bone healing in mice[46,60]. Translation of this technology to the clinic would be facilitated by a strategy that allows the ECM to be generated after implantation through sustained local delivery of GW9662 within the scaffold.

For the purpose of this study, we utilized a biologically inspired osteoinductive scaffold—a macroporous collagen scaffold coated with Mg-doped HA (Coll/MgHA)—as previously reported[78]. To mimic the organic fraction of nascent bone, seeded hMSCs were stimulated with GW9662 to deposit Coll VI and Coll XII on the scaffolds. We hypothesized that incorporating a drug delivery system capable of controlled release of GW9662 into the Coll/MgHA scaffold would stimulate seeded hMSCs to deposit similar levels of the anabolic bone ECM as that of induced with GW9662 added directly to the media. To achieve prolonged GW9662 release, a drug-eluting platform consisting of porous silica particles (pSi) encapsulated in poly(lactide-co-glycolic acid) (PLGA) microspheres was used[84–86]. Furthermore, a bioreactor was used to perfuse the scaffold to mimic the gas and nutrient transport environment observed during neovascularization of callus tissue[13].

2.2. Methods

2.2.1. Preparation of GW9662-Loaded PLGA/pSi Microspheres

The drug-eluting composite microspheres consist of porous silica (pSi) suspended in poly(lactic-co-glycolic) (PLGA) microspheres using methods previously described[87]. Unless stated otherwise, the reagents were purchased from Sigma-Aldrich (St. Louis, MO, USA). Briefly, 300 µl of tetraethyl orthosilicate was added dropwise to a mixture of 0.36% (w/v) tannic acid, 66% (v/v) ethanol, and 33% (v/v) ammonium hydroxide. The mixture was stirred continuously for 3 hours before the pSi were washed and centrifuged three times in a 1:1 solution of ethanol:water. The pSi particles were then lyophilized and stored at -20ºC until needed. To load the pSi with GW9662, 5 mg of lyophilized pSi were

incubated in 1 mL of GW9662 (300 μg/mL) dissolved in DMSO with constant stirring for 20 min at 37 ºC. The GW9662-loaded pSi were washed and lyophilized before proceeding to encapsulation in PLGA microspheres. Briefly, GW9662-loaded pSi were added to a 5% (w/v) PLGA (50:50) (Lactel Absorbable Polymers, Pelham, AL, USA) solution dissolved in dichloromethane (DCM). The PLGA/pSi/DCM mixture was then added dropwise to a 2.5% poly(vinyl alcohol) (PVA) aqueous solution and stirred continuously for 6 hours. The resulting microspheres were then centrifuged and washed several times with DI water before they were lyophilized and stored at -20°C until needed.

2.2.2. Particle Characterization and Evaluation of GW9662 in vitro Release

To verify the presence of pSi in PLGA microspheres, fluorescein isothiocyanate (FITC)-labeled pSi were encapsulated in PLGA microspheres and imaged by confocal microscopy (Nikon D Eclipse C1, Nikon Corporation, Japan). Liquid chromatography-mass spectrometry was used to measure the release of GW9662 from the PLGA-pSi microspheres suspended in an aqueous buffer over the course of 21 days.

2.2.3. Scaffold Fabrication

Porous Coll/MgHA scaffolds with and without PLGA-pSi microspheres were fabricated as described previously with minor modifications[78] (**Figure Appendix 1**). Type I bovine collagen (Nitta Casings, Bridgewater, NJ, USA) was chosen as the organic matrix upon which Mg-doped HA nanocrystals would nucleate during collagen fibrils self-assembly. Briefly, 200 mg of collagen was dissolved in 20 mL of acetic acid buffered at a pH of 3. To the collagen solution, 190 μL of 85% H_3PO_4 (Sigma-Aldrich) and 20 mL of DI water were added. Collagen fibrils containing HA and MgHA were reconstituted by

adding the acidic collagen solution dropwise to a basic suspension consisting of 0.35 g of $Ca(OH)_2$ and 0.166 g of $MgCl_2 \cdot 6H_2O$ (Thermo Fisher, Waltham, MA, USA) in 20 mL of water. The ratio of $Ca(OH)_2$ and $MgCl_2 \cdot 6H_2O$ in the basic suspension was set to 15% as a higher ratio was needed in the precursor solution to achieve the 5-6% molar substitution of Mg^{2+} in the final lattice structure. The mixture was aged for 24 h at 37 °C followed by wet crosslinking with 1,4 butanediol diglycidyl ether (BDDGE) (2.5 mM) (Sigma-Aldrich) at 4 °C for 48 h at a pH of 8. The mixture was then centrifuged and washed several times with DI water to remove crosslinking solution, leaving behind a slurry-like mixture. In some cases, drug-eluting microspheres were added to achieve approximately 0.52 μg GW9662/scaffold. To fabricate a porous structure, the slurry was aliquoted into 96-well plates (70μL/well) and lyophilized after undergoing controlled freezing[78]. The resulting Coll/MgHA scaffolds, referred to either MgHA or MgHA/pSi for brevity, were then stored at -20°C until needed.

2.2.4. Structural and Compositional Characterization of Scaffolds

Fourier-transformed Infrared (FTIR) was performed using an Alpha-Platinum Bruker Spectrometer (Billerica, MA, USA)**.** Prior to acquiring their FTIR spectra, the porous scaffolds were flattened into thin disks using a mortar and pestle and were then kept at 100°C in a heating block for an hour to remove residual water. Thermogravimetric analysis (TGA) was performed on a Q50 (TA Instrument, New Castle, DE, USA) by heating scaffolds (<10 mg) from 25°C to 1000 °C at a rate of 10 °C/min. The molar ratio of Mg^{2+} to Ca^{2+} present in the mineral phase of the scaffolds was determined through inductively coupled plasma-mass spectrometry (ICP-MS) (PerkinElmer NexION 300D,

Waltham, MA, USA), using a multi-element reference standard of Ca^{2+} and Mg^{2+} (ICP CAL-STD EARTH ALKALI, Inorganic Ventures, Christiansburg, VA, USA) in 1% nitric acid. For ICP-MS, scaffolds were digested overnight in 1% nitric acid. The supernatant was collected after a brief centrifugation, filtered using a 0.22 μm syringe filter, and diluted in 1:1200 in 1% nitric acid to ensure ion concentration were within standard curves. Finally, the morphology and distribution of surface pore size of the scaffolds were assessed by scanning electron microscopy (SEM) on a JCM 5000 (JEOL, Peabody, MA, USA) and analyzed using ImageJ (NIH Image). Lyophilized scaffolds stored in -20 °C were kept overnight in a desiccator and were then gold sputter coated (20 mA, 60 sec) to remove accumulated water prior to SEM imaging. Approximately 146 and 119 pores were analyzed for the MgHA and MgHA/pSi scaffolds, respectively

2.2.5. Expansion and Seeding of hMSCs

Bone marrow-derived hMSCs were acquired from the adult stem cell distribution center at Texas A&M Health Science Center Institute for Regenerative Medicine in accordance with institutionally approved protocols. Bone marrow-derived hMSCs were expanded in complete culture media (CCM) consisting of alpha minimal essential medium (α-MEM, Invitrogen, Carlsbad, CA, USA), 20% (v/v) FBS (Atlanta Biologicals, Flowery Branch, GA, USA), 2 mM L- glutamine (Invitrogen), and 100 U/ml penicillin plus 100 μg/ml streptomycin (HyClone™ , Marlborough, MA, USA) at a seeding density of 500 cells/cm^2. Culture media was changed every 2-3 days until cells reached 70-80% confluency. Expanded cells were then recovered by brief trypsinization (Corning, Corning, NY, USA) and seeded at the top of each scaffold (200,000 cells/scaffold) using

a 20 µL aliquot. After incubating for 10 minutes, scaffolds were flipped 180° and an additional 5 µL of CCM was added to achieve a more uniform distribution of cells. Scaffolds were then incubated for an additional 10 minutes before CCM was added to well plates, keeping track of the area in which cells were initially seeded. The cells were incubated overnight before scaffolds were switched to different culture media formulations or placed in the perfusion bioreactor. The other culture media formulations included: 1) osteogenic basal media (OBM) consisting of CCM supplemented with 50 µg/mL of ascorbic acid and 5 mM β-glycerol phosphate, 2) OBM supplemented with 10 µM GW9662 dissolved in DMSO as a positive control, and 3) OBM supplemented with an equal volume of DMSO as a vehicle control. A table depicting the scaffold/media formulation used for osteogenic assays can be found in **Table 2.1.**

Scaffold	Media Formulation	Denoted As
Collagen/MgHA	OBM + DMSO (vehicle control)	DMSO
Collagen/MgHA	OBM + 10 µM GW9662 (positive control)	GW-media
Collagen/MgHA + PLGA/pSi	OBM (controlled GW9662 delivery)	GW-pSi

Table 2.1: Scaffold composition and cultured media used for osteogenic assays. All possible permutations of scaffold/media formulations were cultured in both static and perfused conditions.

2.2.6. Culture in Static and Perfused Conditions

Scaffolds were placed in the wells of the bioreactor (**Figure Appendix 1, B&C**), positioning them so that surface in which cells were initially seeded faced down towards the channels. A silicone rubber gasket with a diameter similar to the scaffolds was placed on top to block perfusate from flowing around, instead of through, the scaffolds. Once placed in the perfusion bioreactor, a multichannel peristaltic pump (Cole-Palmer, Vernon Hills, IL, USA) was used to adjust the culture media flow rate to achieve a superficial velocity through the scaffolds of approximately 116 μm/sec, resulting in an estimated shear stress of about 7 mPa. Shear stress experienced by the cells was estimated using a previously described equation[76]:

$$\boldsymbol{\tau_w = \frac{8\,\mu_m u}{d_p}}$$

where τ_w is the fluid wall stress within the pores of the scaffold, μ_m is the viscosity (~0.77 cPa) of the culture media, u is the interstitial velocity, and d_p is the average pore diameter observed in the scaffolds by SEM imaging. Scaffolds were perfused up to 21 days, with media changes occurring every 2-3 days.

2.2.7. Cell Migration on Scaffolds

Seeding efficiency was approximated by recovering hMSCs attached to the well plates rather than the scaffolds the day after seeding using standard cell counting procedure with a hemacytometer. To evaluate hMSCs viability and migration into the scaffolds without the influence of soluble factors, live-dead staining—5 μM of Calcein AM and 0.1% Propidium Iodide—was performed after 8 days of static and perfused culture in MgHA/CCM scaffolds. Confocal Z-stack images of the scaffolds were captured

with a Nikon D Eclipse C1 upright microscope (Nikon Corporation, Japan) from upstream face of the scaffold to a depth of 200 μm using 10 μm slices. The relative fluorescent intensity units for z-stacked images were evaluated as a function of depth using ImageJ (NIH Image). The depth at which stacked live-dead images decreased to 50% of maximum fluorescence intensity was quantified for both static and perfused samples. Afterwards, scaffolds were cut to acquire cross-sectional images.

2.2.8. Immunostaining of Deposited Matrix Proteins

GW9662-treated hMSCs have been previously shown to deposit a unique ECM rich in collagens that are highly expressed in anabolic bone, specifically Coll VI and Coll XII. To evaluate the efficacy of the PLGA-pSi microspheres, immunostaining for Coll VI and XII was performed on scaffolds after 8 days of culture. Briefly, scaffolds were fixed overnight at 4°C in in 4% formaldehyde in PBS and washed three times with PBS. Scaffolds were then blocked with 5% goat serum (MP Biomedical) and 0.3% Triton-X (Sigma Aldrich) for 1 hour at room temperature before being incubated overnight at 4°C in blocking buffer supplemented with either rabbit anti-Human Coll VI or Coll XII (1:200, Novus Biological, Littleton, CO, USA). Scaffolds were then washed with PBS and were incubated at room temperature for 2 hours in blocking buffer with fluorescein-conjugated goat anti-rabbit (1:500, Millipore, Burlington, MA, USA). Z-stack images were taken as described above. Maximum intensity projections was performed on the EZ-C1 software (Nikon Corporation, Japan).

2.2.9. Gene Expression via Quantitative RT-PCR (qRT-PCR)

After 8 and 21 days of culture, total RNA was extracted from the scaffolds with RNeasy Mini Kit (Qiagen, Hilden, Germany) supplemented with Trizol (Life Technologies, Carlsbad, CA, USA). After quantifying the purity and concentration of RNA (Infinite M200 Pro, Tecan, Männedorf, Switzerland), isolated RNA with a purity (A260/A280) above 1.9 was used for cDNA synthesis in 21 µL reaction (Superscript III kit, Invitrogen). Approximately 6.5 ng of cDNA was amplified in a 20 µL reaction containing Brilliant III Ultra-Fast SYBR Green QPCR Master Mix with Low ROX (Agilent, Santa Clara, CA, USA) on an Agilent Aria Mx Real-Time PCR System. The primer list and their sequences can be found in the supplementary information (**Table Appendix 1**). Relative expression was calculated using the $\Delta\Delta C_T$ method normalized to human glyceraldehyde-3-phosphate dehydrogenase (GAPDH) levels, using hMSCs cultured for either 8 or 21 days in 2D monolayer on tissue culture plate with CCM as the calibrator control. Relative fold change in gene expression was calculated using $2^{-\Delta\Delta Ct}$ method described by Livak and Schmittgen[88].

Statistical comparisons were performed on GraphPad Prism software (San Diego CA, USA). Briefly, a Bartlett's test was performed on the C_t values for each gene, for each scaffold/culture condition (**Table Appendix 5**) to confirm homogeneity prior to running a two-way ANOVA. A two-way ANOVA was performed on the calculated $\Delta\Delta C_T$ values, followed by a Tukey's multiple comparison test (n=3), whose results can be found in the supplementary information (**Table Appendix 5-17**). In addition, the number of hMSCs present in the scaffolds was measured via GAPDH expression after 8 days of static and

perfused culture in all scaffold/culture conditions using known cell number standards. RNA was extracted from the cell standards in the presence of MgHA scaffolds to mimic the RNA extraction efficiency from the cultured scaffolds. Statistical testing as described above was performed on the calculated cell number (**Table Appendix 2-4**).

2.2.10. Microcomputed Tomography (μCT) Analysis of Cultured Scaffolds

After 21 days of static and perfused cultures, scaffolds were washed with PBS and fixed overnight at 4°C with 4% formaldehyde in PBS. After washing with and aspirating excess PBS, samples were allowed to dry overnight in a desiccator. Samples were stored at -80°C until needed. Uncultured scaffolds were used as controls and were prepared as described above. Prior to acquiring μCT scans on a SkyScan 1275 X-Ray Microtomograph (Bruker, Billerica, MA, USA), samples were gently wrapped in Parafilm for easier handling during imaging on the SkyScan's rotating stage. Scaffolds were imaged over 360 degrees with a camera resolution of 18 μm, with images taken every 0.5 degrees using a 28 kV beam and a frame averaging of 3. The cross-sectional images of the scaffolds were reconstructed using NRecon (Micro Photonics) software, keeping the smoothing and beam-hardening compensation settings the same between samples at 0 (Gaussian Kernel) and 41%, respectively. Thresholding was done to better distinguish between Parafilm and the scaffolds. Calcium hydroxyapatite phantoms (0.25 and 0.75 g/cm^3; Bruker) were scanned using the settings described above and analyzed in the Bruker-MicroCT CT-Analyser (CTan) software to determine their attenuation coefficient values in order to predict the bone mineral density (BMD) of the scaffolds. After confirming equal variances (**Table Appendix 18**), a two-way ANOVA followed by a Tukey's multiple comparison

test were performed on the bone mineral density values (n=3). Both the ANOVA table and the results for the multiple comparison test can be found in the supplementary information (**Table Appendix 19-20**). CTan software was also utilized to measure morphological characteristics of the scaffolds, specifically percent porosity and the specific bone surface (BS/BV)[89] of the scaffolds. The CTVox software was utilized to reconstruct images of the cultured samples. Identical opacity thresholding was utilized for all reconstructions. Maximum intensity projection (MIP) was enabled to highlight dense regions of mineralization.

2.2.11. Uniaxial Compression Test

After acquiring μCT scans, scaffolds were gently removed from the parafilm wrapping and stored at -80°C until needed for mechanical testing. The diameter and thickness of the scaffolds were measured with calipers, and underwent a uniaxial compression test to 15% strain at a rate of 5 μm/s on a DMA 850 (TA Instruments). The compressive modulus was calculated through linear fitting of the slope. Statistical comparisons were performed on the compressive modulus using two-way ANOVA followed by a Tukey's multiple comparison test (n=3). The ANOVA table and its corresponding multiple comparison results can be found in the supplementary information (**Table Appendix 22-23**).

2.2.12. Immunoblotting

After 8 days of static and perfused culture, scaffolds were washed with warm followed by ice-cold PBS. Proteins were extracted using ice-cold RIPA buffer (50 mM Tris HCl, 150 mM NaCl, 1% Triton-X-100, 0.1% SDS, 0.5% Sodium Deoxylcholate, 1

mM EDTA, 1 mM Sodium Pyrophosphate) supplemented with SIGMAFAST^{TM} protease inhibitors (Sigma-Aldrich) through vortexing followed by centrifugation at 12,000g for 10 min. The supernatant was recovered and stored at -80°C until total protein content was quantified through Pierce BCA Protein Assay kit (Thermo Fisher Scientific). Protein samples (15 μg) were resolved in hand-casted 10% SDS-PAGE gel (Bio-Rad, Hercules, CA, USA) and transferred to a PVDF membrane (Millipore). The membrane was blocked in 5% milk in TBST buffer (20 mM Tris-base, 150 mM NaCl, 0.2% Tween 20) for one hour before being incubated overnight at 4 ºC with mouse anti human BMP2 antibody (R&D Systems, Minneapolis, MN, USA) diluted (1:500) in blocking buffer. After 3 washes in TBST buffer, the membrane was incubated for 1 hour with an HRP-conjugated goat anti mouse secondary antibody (Protein Tech, Rosemont, IL, USA). The membrane was developed for 5 minutes in WesternSure Chemiluminescent Substrate (LI-COR, Lincoln, NE, USA) and imaged on a C-Digit Blot Scanner (LI-COR). After imaging, the membrane was stripped using Restore Stripping Buffer (Thermo Fisher Scientific) following the manufacturer's instructions. The membrane was then blocked, incubated with mouse-anti-human GAPDH (1:4000, Protein Tech), and imaged as previously described.

2.3. Results

2.3.1. Morphology and Composition of Scaffolds

The microstructure of MgHA and MgHA/pSi scaffolds were evaluated via SEM and μCT. SEM imaging of the scaffold surfaces revealed an isotropic porous structure (**Figure 2.1A**). Cross-sectional μCT scans of the scaffolds internal microstructure

indicated interconnected pores (**Figure 2.1B**). When quantifying surface pore size, a wide distribution of pore diameter of 50-200 µm was observed, **(Figure 2.1C**). Analysis of morphological characteristics showed that inclusion of the drug-eluting microspheres had no effect on either specific bone surface ratio (**Figure 2.1D**) or porosity (**Figure 2.1E**).

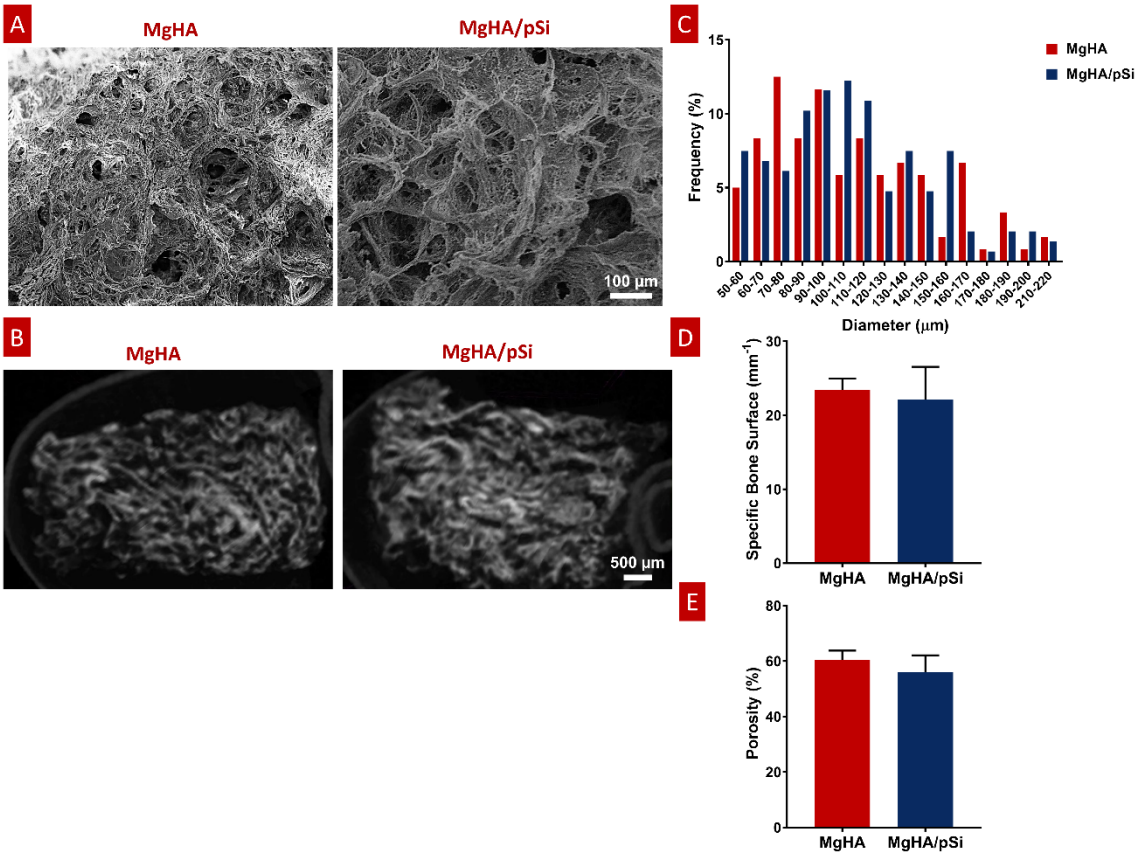

Figure 2.1: Morphological characterization of MgHA and MgHA/pSi scaffolds. Representative A) SEM and B) micro-computed tomography (µCT) images of MgHA and MgHA/pSi scaffolds. C) Pore size distribution is shown to be similar between the two scaffolds. D) Specific bone surface ratio and E) percent porosity were unaffected by the addition of drug-eluting microspheres.

TGA analysis was performed to quantify the mineral-to-protein ratio of the scaffolds. The initial loss in mass observed, approximately 10%, was attributed to residual

water in the scaffolds. Thus, the collagen matrix and the mineral phase contributed approximately 33% and 66% of the scaffolds dry weight (**Figure 2.2A**). Scaffold composition was further characterized using FTIR (**Figure 2.2B**). Large bands were observed in 550 cm^{-1} and 1000 cm^{-1}, corresponding to phosphates in hydroxyapatite. For the organic component, vibrational bands characteristic to amide groups were observed around 1250 cm^{-1}, 1540 cm^{1}, 1650 cm^{-1}, and 3300 cm^{-1}. Carbonate ion substitutes within the crystalline structure were also detected, as indicated by the small single peak at 870 cm^{-1} and the double bands around 1430 cm^{-1} and 1450 cm^{-1}, which indicate a type-B carbonated substitution in the PO_4^{3-} position[34,90]. XRD analysis showed both scaffolds shared a similar profile to that of native bone tissue reported in the literature, specifically large peak at 32 degrees and a smaller peak at 26 degrees (**Figure 2.2C**). The Mg/Ca substitution ratio was evaluated to be approximately 4.8% and 4.2% for MgHA and MgHA/pSi scaffolds, respectively (**Figure 2.2D**).

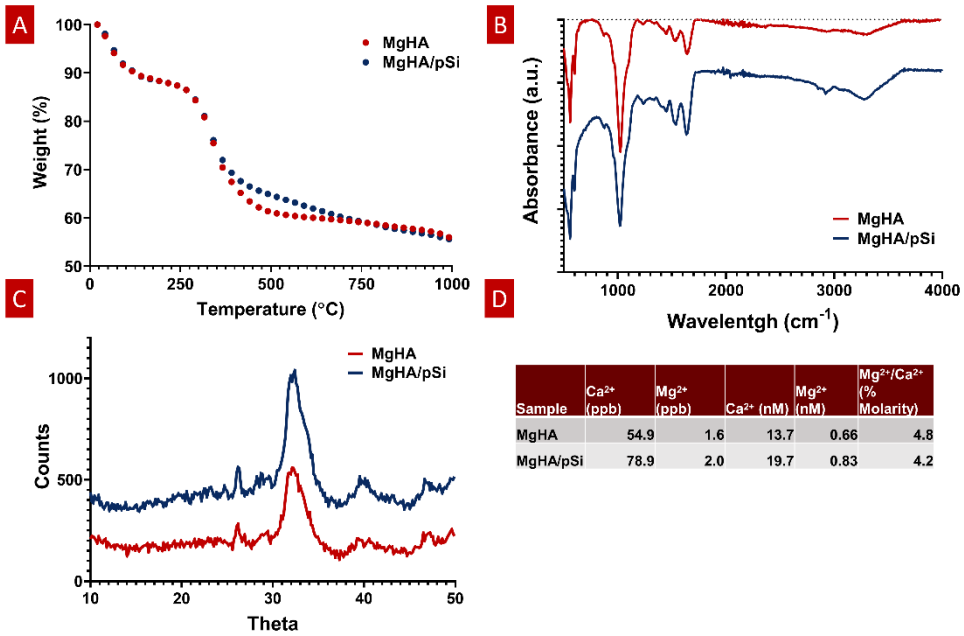

Sample	Ca^{2+} (ppb)	Mg^{2+} (ppb)	Ca^{2+} (nM)	Mg^{2+} (nM)	Mg^{2+}/Ca^{2+} (% Molarity)
MgHA	54.9	1.6	13.7	0.66	4.8
MgHA/pSi	78.9	2.0	19.7	0.83	4.2

Figure 2.2: Characterization of the composition of the MgHA and MgHA/pSi scaffolds via TGA A), FTIR B), XRD C), and ICP-MS D).

2.3.2. Cell Number and Infiltration in Static and Perfused Conditions

A seeding efficiency above 93% was observed for each scaffold composition (**Figure 2.3A**). After 8 days of static culture in MgHA scaffold with CCM, live-dead staining revealed closely packed cells near the surface of the scaffolds, with a majority of cells staying within 100 µm from the surface of the scaffolds. In contrast, hMSCs perfused for 8 days invaded more deeply into the scaffold (**Figure 2.3B**). Semi-quantitative analysis of confocal images showed a rapid drop in fluorescence in the static samples, with a 50% reduction approximately 60 µm into the scaffold, as compared to 150 µm for perfused scaffolds (**Figure 2.3C**).

Next, cell number was quantified by GAPDH expression for the eight culture conditions (**Figure 2.3D**). Two-way ANOVA indicated that perfusion increased the average cell number in all scaffolds and a lack of interaction between perfusion and the scaffold/culture media formulation (**Table Appendix 3**). Multi-comparison testing indicated that, in perfused cultures, GW9662 administered locally increased cell number significantly relative to the DMSO control (**Table Appendix 4**).

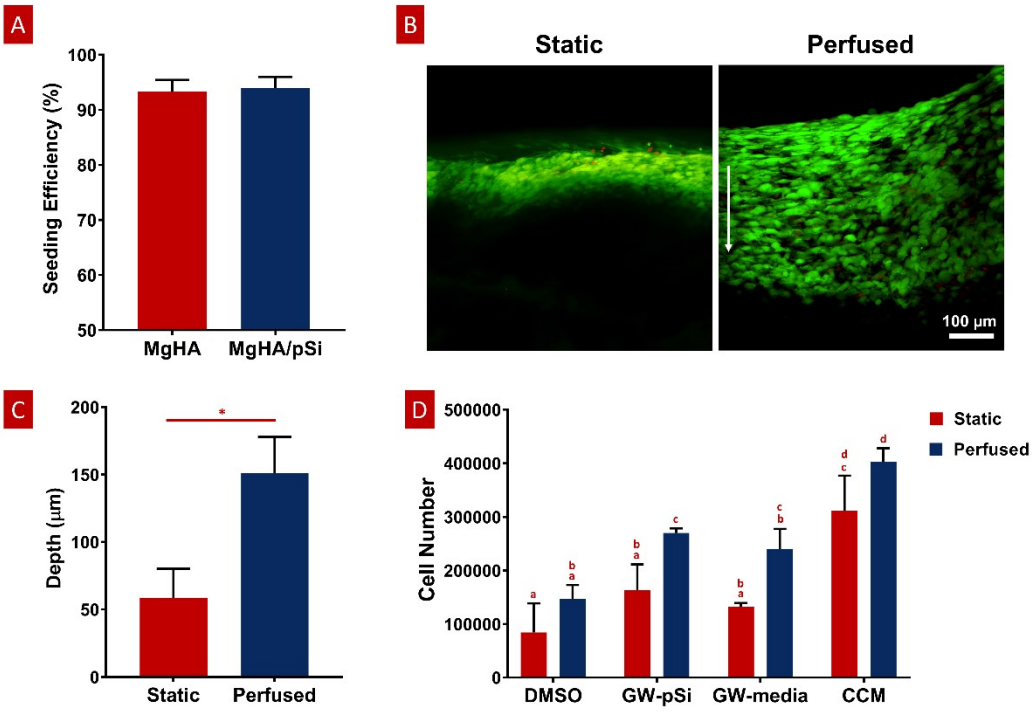

Figure 2.3: A) hMSCs seeding efficiency on scaffolds (n=3). B) Representative cross-sectional images of live-dead staining of hMSCs after 8 days of culture in MgHA scaffolds in static and perfused conditions, with direction of flow indicated by the white arrow. C) Average depth at which stacked live-dead images decreased to 50% of maximum fluorescence intensity (Student's t-test, * $p<0.05$, n=3, error bars depict standard deviation). D) hMSCs population, as quantified by GAPDH expression via qRT-PCR, shows significant increase in cell number in response to perfusion in various scaffold and culture media combinations. Statistical testing was performed by two-way ANOVA, followed by a Tukey's multiple comparison between all scaffold/media combinations. Columns with matching letters indicate the comparison was not significant. ($p<0.05$, n=3, error bars depict standard deviation).

2.3.3. Microsphere Characterization and in vitro release of GW9662

Fluorescently-labelled pSi were used to characterize their distribution within PLGA microspheres (**Figure 2.4A**). Images indicated that the pSi were distributed uniformly within individual microspheres and that pSi content appeared uniform when comparing different PLGA microspheres.

The rate of release of GW9662 from the composite pSi/PLGA microspheres was quantified over a 21-day period since osteogenic differentiation of hMSCs using GW9662 involves continuous application of GW9662 for this duration[44]. A 14% burst release occurred in the first 24 hours, followed by a constant rate of release over the remainder of the experiment, with 82% of the drug released after 21 days (**Figure 2.4B**).

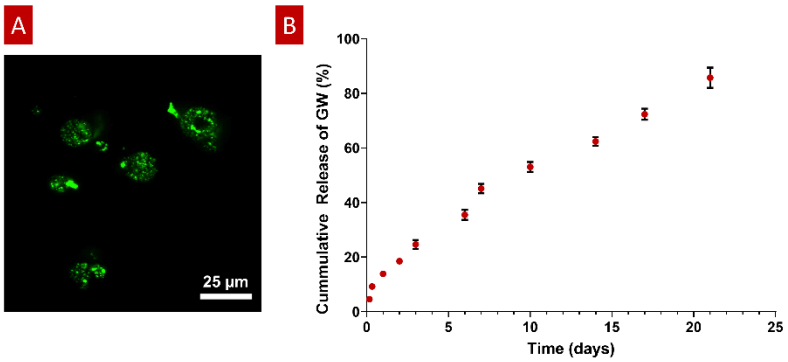

Figure 2.4: A) Confocal imaging of FITC-labeled PLGA/pSi show pSi are uniformly distributed within PLGA spheres. B) Cumulative release of GW9662 from PLGA/pSi microspheres show controlled release of GW9662 up to 21 days (n=3, error bars depict standard deviation).

2.3.4. Deposition of Anabolic Bone ECM

It has been previously shown that hMCSs treated with GW9662 secrete an anabolic bone ECM rich in Coll VI and XII, which not only improves retention of hMSCs at an injury site, but also upregulates various osteogenic and angiogenic factors[46]. To validate the efficacy of the controlled release of GW9662 from PLGA/pSi microspheres and to explore the effects of the fluid shear stress on the expression and deposition of this anabolic bone matrix, qRT-PCR analysis and immunostaining for Coll VI and Coll XII was performed after 8 days of static and perfused culture. The length of culture time was chosen to coincide with the formation of fibrocartilaginous callus seen during fracture repair[5].

Consistent with previous findings[46], hMSCs cultured under static conditions in media supplemented with GW9662 expressed Coll VI in significantly higher amounts than in the absence of GW9662 and cultures in which GW9662 was provided using microspheres (**Figure 2.5A**). Interestingly, the expression for Coll VI was increased by perfusion culture for each condition, though this difference was not significant in the cultures in which GW9662 was added directly to the media. Furthermore, perfusion resulted in comparable levels of Coll VI expression between DMOS, GW-pSi, and GW-media scaffolds. The simple interaction—diminishing returns of GW9662-treatment on Coll VI gene expression by perfusion—was confirmed to be significant by two-way ANOVA (**Supplementary Table 6**). Immunostained samples indicated comparable amounts of Coll VI in the cultures in which GW9662 was administered via controlled release (**Figure 2.6B**) or direct addition to the media (**Figure 2.6C**), while the Coll VI was

barely detectable in the cultures lacking GW9662 (**Figure 2.6A**). Perfusion increased amount of Coll VI detected by immunostaining in each condition, with the levels noticeably higher for samples containing GW9662 **(Figure 2.6E & F**) than samples lacking GW9662 (**Figure 2.6D**).

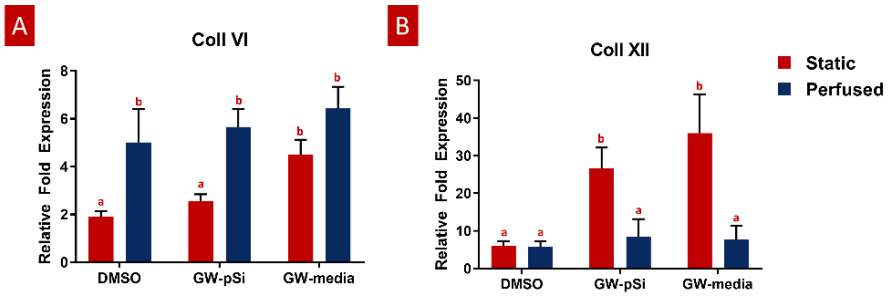

Figure 2.5: qRT-PCR analysis for the expression of anabolic bone ECM components. A) Coll VI and B) Coll XII relative fold expression in hMSCs after 8 days of culture in various scaffold/media combinations. Columns with matching letters indicate all possible comparisons were not significant (n=3, error bars depict standard deviation, $p<0.05$, two-way ANOVA, Tukey's multiple comparison test).

Under static conditions, Coll XII gene expression was significantly higher in hMSCs cultured in media supplemented with GW9662 than in cultures lacking GW9662 (**Figure 2.5B**). In addition, controlled release of GW9662 from microspheres resulted in comparable expression levels to exogeneous GW9662 administration, highlighting the utility of the composite microspheres as an in-situ drug release platform capable of replacing traditional media treatments. It was also noted that despite the lack of GW9662, Coll XII gene expression was positively expressed in DMSO scaffolds (**Figure 2.5B**). Furthermore, in contrast to the trend observed for Coll VI gene expression, Coll XII gene

expression either stayed consistent or decreased in response to perfusion, suggesting at a suppressive interaction between perfusion and GW9662 treatment on Coll XII gene expression (**Table Appendix 8**). Immunostaining of samples cultured under static conditions confirmed comparable deposition of Coll XII between cultures in which GW9662 was administered directly to the media (**Figure 2.6I**) and controlled release (**Figure 2.6H**). In contrast, Coll XII deposition was scarce in samples lacking GW9662 (**Figure 2.6G**). Perfusion increased the amount of Coll XII detected via immunostaining in all conditions, with noticeably higher depositions in samples treated with GW9662 (**Figure 2.6K & L**) than in samples lacking GW9662 (**Figure 2.6J**).

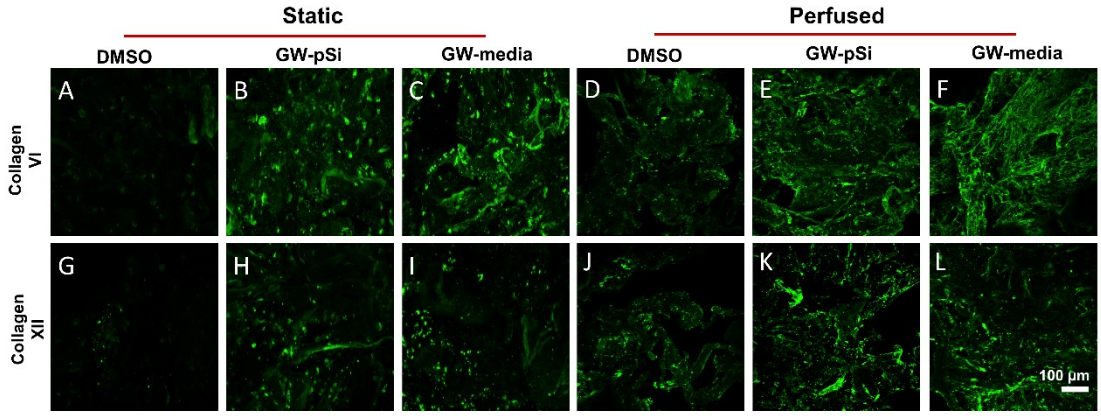

Figure 2.6: Immunostaining of Coll VI A-F) and XII G-L) after 8 days under static and perfused conditions for various scaffold/culture media combinations reveals similar levels of matrix deposition between GW-pSi and GW-media. Perfusion increased matrix deposition in all scaffold and culture media combinations relative to their static counterparts.

2.3.5. In vitro Osteogenic Differentiation in Osteoinductive Scaffolds

To assess the osteoinductive potency of the scaffolds, the relative expression of the early osteogenic markers ALP and BMP2 were examined after 8 days of culture, while the late markers osteocalcin (OCN) and osteopontin (OPN) were investigated after 21 days of culture by qRT-PCR analysis. Briefly, no significant difference was observed in ALP expression between GW-media and DMSO scaffolds under static conditions. In contrast, ALP expression increased significantly in GW-pSi scaffolds in comparison to both the DMSO and GW-media scaffolds (**Figure 2.7A**). Perfusion further upregulated ALP expression in all scaffold compositions (**Figure 2.7A**). No significant interaction between the effects of perfusion and media/scaffold formulation on ALP expression was observed (**Table Appendix 10**). BMP2 gene expression in the absence of perfusion increased in response to GW9662 treatment, with both GW-pSi and GW-media scaffolds having significantly higher expression than the DMSO scaffolds (**Figure 2.7B**). A significant increase in BMP2 gene expression was observed in the vehicle controls in response to perfusion compared to its static counterpart. In contrast, BMP2 gene expression was negatively impacted in both exogenous and drug-eluting GW9662 samples under perfusion (**Figure 2.7B**). The interaction between perfusion and media/scaffold formulation was found to be significant (**Table Appendix 12**). To further investigate these trends at the protein level, immunoblotting against BMP2 was performed. Immunoblotting revealed GW9662 treatment and perfusion had a synergistic effect on BMP2 expression at the translational level (**Figure Appendix 2**).

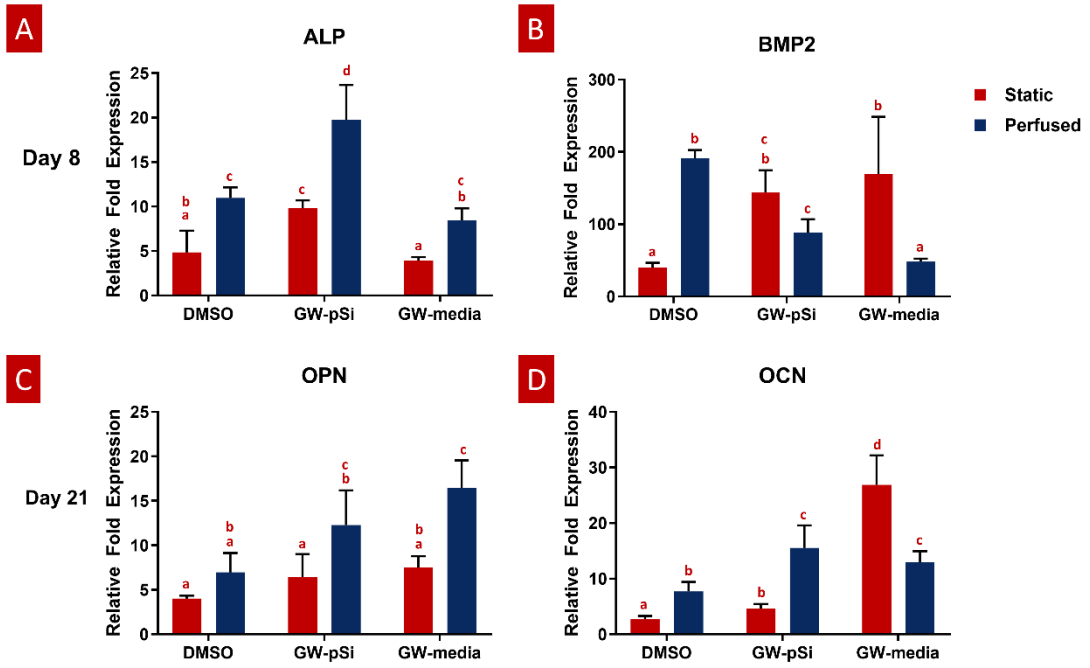

Figure 2.7: qRT-PCR analysis for the expression of osteogenic markers in hMSCs after A) and B) 8 days or C) and D) 21 days of culture in various scaffold/media combinations. Fold changes were normalized to the expression levels of uninduced hMSCs after 8 or 21 days of 2D culture. Columns with matching letters indicate all possible comparisons were not significant. (n=3, error bars depict standard deviation, $p<0.05$, two-way ANOVA, Tukey's multiple comparison test).

A trademark of terminally differentiated hMSCs is the expression of late osteogenic markers. Thus, expression of osteopontin (OPN) and osteocalcin (OCN) at the transcription level was investigated after 21 days of culture. OPN was positively expressed in all scaffolds and media conditions, with the lowest level expressed in the DMSO scaffolds (**Figure 2.7C**). Although OPN expression increased in both the exogeneous and GW9662-eluting microspheres scaffolds relative to the DMSO control under static conditions, the trend was not significant. Perfusion significantly upregulated OPN expression in both GW-pSi and GW-media scaffolds relative to the static DMSO

scaffolds. The interaction between perfusion and scaffold/media formulation and their effects on OPN expression was not significant (**Table Appendix 14**). OCN expression was positively expressed in DMSO scaffolds and responded strongly in a dose-depended manner to GW9662 treatment. Briefly, GW-media and GW-pSi had significantly higher levels of expression relative to the DMSO control (**Figure 2.7D**). The application of perfusion stimulated higher levels of OCN expression in GW-pSi and DMSO scaffolds while decreasing OCN expression in GW-media scaffolds. However, fold expression in perfused GW-media scaffolds were still significantly higher than the static vehicle control. The interaction between perfusion and scaffold/media formulation on OCN was found to be significant (**Table Appendix 16**).

2.3.6. In-vitro Mineralization and Scaffold Compressive Strength

Mineralization within the scaffolds was detected with μCT. The degree of radio-opacity of reconstructed μCT images of the scaffolds harvested after 21 days of culture (**Figure 2.8A-F**) is summarized in **Figure 2.8G**. DMSO (**Figure 2.8A**) scaffolds cultured under static conditions were largely radiolucent, while larger volume of GW-pSi (**Figure 2.8B**) and GW-media (**Figure 2.8C**) scaffolds were detected. Furthermore, denser regions, which correlate to degree of mineralization, were detected in all perfused samples, with larger regions detected in the GW-pSi (**Figure 2.8E**) and GW-media (**Figure 2.8F**) scaffolds. When quantified using the attenuation coefficient method, significantly higher levels in bone mineral density were detected in scaffolds cultured under perfusion relative to their static counterparts in all three scaffolds/media conditions (**Figure 2.8G**). The interaction between perfusion and scaffold/media formulation and their effects on BMD

was not significant (**Table Appendix 19**). Under static conditions, GW9662 treatment resulted in significantly higher BMD levels compared to the DMSO scaffolds, regardless of GW-source. A similar trend was observed under perfusion. (**Figure 2.8G**).

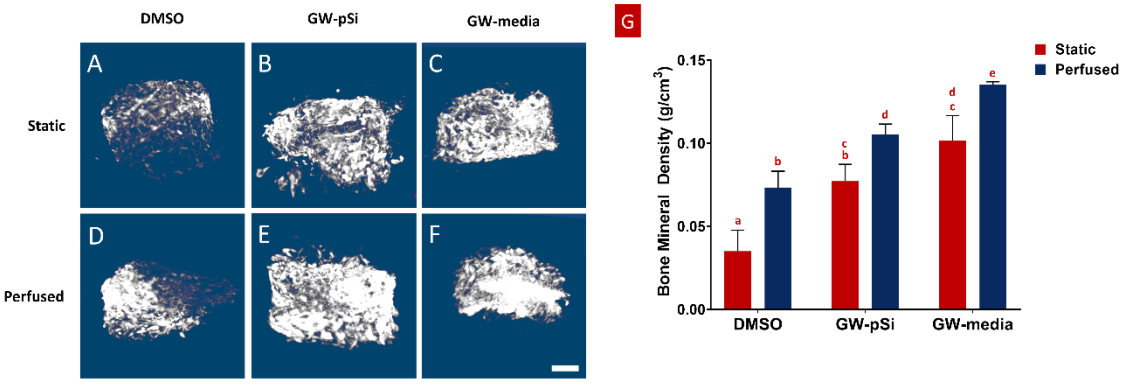

Figure 2.8: A-F) Representative µCT reconstructions of scaffolds after 21 days of culture (scale bar 500 µm). G) Bone mineral density increases in response to both perfusion and GW9662. Columns with matching letters indicate all possible comparisons were not significant (n=3, error bars depict standard deviation, $p<0.05$, two-way ANOVA, Tukey's multiple comparison test).

We then evaluated whether the augmented bone mineral density translated to improved mechanical properties. Although the variances in scaffold compressive moduli were not homogenous due in part to an outlier in GW-pSi perfused samples, a two-way ANOVA and Tukey's multiple comparison test was still performed to ensure similar analysis could be performed between assays (**Table Appendix 21**). Mechanical testing revealed a general trend in improved compressive modulus in response to perfusion (**Figure 2.9A-C**). Although the compressive modulus increased in response to perfusion in DMSO and GW-media scaffolds in comparison to their static counterparts, the trend

was not significant. (**Figure 2.9D**). In contrast, a significant difference was observed between perfused and static GW-pSi scaffolds (**Figure 2.9D**). Furthermore, the combined treatment of GW9662, through either exogenous means or microspheres, and perfusion resulted in compressively stiffer scaffolds compared to the static MgHA/DMSO scaffold (**Figure 2.9D**). Lastly, a strong correlation between bone mineral density and compressive modulus was observed for the 18 pooled samples, with a Person's correlation r value of 0.696 and a two-tailed p-value of 0.014 (**Figure 2.9E**).

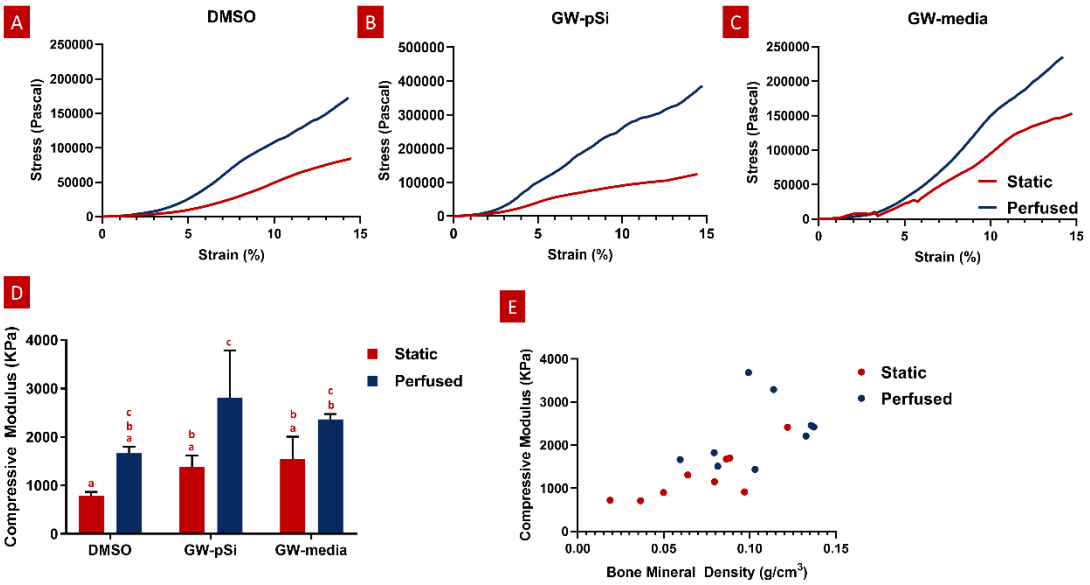

Figure 2.9: A-C) Representative compressive tests of scaffolds after 21 days of culture. D) Average compressive modulus of scaffolds after 21 days of culture. Columns with matching letters indicate all possible comparisons were not significant (n=3, error bars depict standard deviation, $p<0.05$, two-way ANOVA, followed by Tukey's multiple comparison test). E) High degree of correlation between observed bone mineral density and compressive modulus for the compiled 18 samples (Pearson's correlation r value of 0.695, $p<0.05$).

2.4. Discussion

Several key morphogenetic pathways, e.g. Wnts, BMPs, active during embryonic skeletal development are observed during bone repair, allowing bone tissue to be restored to its uninjured state[12,91]. During the anabolic phase of bone repair, a callus tissue is deposited by recruited progenitor cells and is partially mineralized[12,14]. This anabolic bone tissue is characterized by high levels of unique types of collagens, such as Coll VI and XII, that play a major regulatory role[24,43]. Furthermore, nascent ossified bone tissue in both fracture calluses and in developing bone contain ionic substitutions[17,37], specifically Mg^{2+}, in the hydroxyapatite crystalline structure that allows for rapid ion exchange. Thus, the key to the development of new scaffolds for bone repair lies in recapitulating both the inorganic and organic phases of the anabolic bone niche. The response of hMSCs cultured in a macroporous Coll/MgHA scaffold with GW9662-eluting microspheres for the purpose of depositing an ECM rich in Coll VI and XII demonstrates the feasibility of producing a scaffold that resembles both mineral and collagen content of regenerating bone.

The fabrication of the scaffolds was inspired by the biomineralization process of trabecular bone, which can be described as a poorly crystalline biological apatite with ionic substitutions coating an underlying macroporous protein structure[34,36]. Through controlled freezing and lyophilization, it was possible to fabricate a highly porous composite scaffold, which lends itself to high cell infiltration when coupled with a perfusion bioreactor. Upon evaluation, the scaffolds showed a close similarity in their morphology and mineral composition to that of trabecular bone tissue. Briefly, the specific

bone surface ratio (BS/BV) of our scaffolds (*cf*. **Figure 2.1D**) was similar to values (17.03±4.06 mm^{-1}) reported for trabecular bone in the human femur [92]. Analysis of the scaffolds' composition revealed additional substitutions in the apatite structure other than Mg^{2+} substituting for Ca^{2+}. Carbonate ion substitutes, specifically type-B (870 cm^{-1}), were also detected within the lattice structure. The presence of Mg^{2+} and carbonate ions are particular noteworthy as they are typically found in younger, more reactive bone, as they allow for reversible exchange of ions [34–36], which is lost as bone matures. Thus, the presence of Mg^{2+} and type-B carbonate ions reaffirms that the scaffolds were effectively recapitulating the mineral features of immature bone, a highly osteogenic environment.

Although the fabricated scaffolds mimicked key mineral features of newly formed bone, its sole use of Coll I in the underlying protein structure fails to mimic the cocktail of rare collagens that are upregulated in developing and regenerating bone. Specifically, Coll XII is abundantly present in the outer and inner layers of the periosteum of developing long bones[42], and has been shown to play an important regulatory role in osteoblast differentiation and bone matrix formation[43]. Coll VI is highly expressed in the primary osteons of the femoral diaphysis, where it supports the proliferation and maturation of pre-osteoblasts[18]. Coll VI is also highly expressed in the middle layer of the Groove of Ranvier, and important ossifying region in long bone development, and helps regulate the differentiation of pre-osteoblasts prior to maturation[24]. We have previously shown that hMSCs treated with GW9662 secrete a complex cocktail of ECM that contains high levels of Coll VI and Coll XII, which can be used to extend the retention of hMSCs at a lesion site, resulting in superior bone healing[45]. Although the ECM generated from GW9662-

treated hMSCs have shown a remarkable capacity to regenerate bone even when administered to lesion sites without hMSCs, its purification and fabrication into a 3D scaffold is an expensive, time-consuming process. Stimulating hMSCs to deposit the anabolic bone ECM on established scaffolds after implantation would circumvent some of these challenges and facilitate translation to the clinic. However, GW9662 necessitates constant replenishing to achieve its desired effects due to a short half-life[93]. We hypothesized that incorporating a drug delivery system capable of controlled release of GW9662 into porous mineralized scaffold would yield comparable deposition of ECM compared to traditional fabrication methods (10 μM every 2-3 days). Although direct implantation of hMSCs cultured on scaffolds embedded with GW9662-eluting microspheres is a possible clinical application route, we also explored the use of a perfusion bioreactor to improve deposition of the anabolic bone ECM throughout the scaffold. Together, the drug eluting microspheres and the perfusion bioreactor could be utilized to fabricate clinically relevant scaffolds for bone repair.

In order to fully understand Coll VI and Coll XII deposition trends, gene expression was correlated with immunostaining. While mRNA expression of Coll VI and Coll XII increased to varying degrees due to GW9662 and the drug eluting microspheres, only Coll VI expression increased in response to perfusion. In fact, a decrease in Coll XII expression was observed after 8 days of culture in the bioreactor. Immunostaining, however, showed a striking difference between static and perfused samples, revealing a remarkable increase in deposition of both Coll VI and Coll XII in terms of uniformity and density throughout GW-pSi and GW-media scaffolds. The differences between mRNA

and protein expression of Coll VI and Coll XII could be partially attributed to a possible negative feedback mechanism in which the anabolic bone ECM negatively regulates the further expression of ECM components. This result is at least partially attributable to the relatively high amount of hMSCs and their distribution deeper into the scaffold. Increased ECM deposition by hMSCs due to fluid shear stress has been previously reported[75], suggesting another mechanism by which perfusion promotes ECM deposition in the scaffolds. To our knowledge, this is the first time that perfusion has been used to in conjunction with a drug eluting system to fabricate a unique blend of matrix proteins for the purpose of mimicking the complex microenvironment of anabolic bone. Furthermore, the GW9662 eluting microspheres were capable of stimulating the deposition of the anabolic bone ECM using significantly less GW9662 compared to exogenously supplemented culture media; 0.52 μg of GW9662 in GW-pSi for 8 days of culture vs. 5.5 μg GW9662 added every 2 days in GW-media scaffolds.

As trabecular bone is major reservoir of progenitor cells[94], we initially quantified hMSC infiltration into the scaffolds under both static and perfused conditions without the influence of GW9662. In agreement with previous studies, cells cultured under static conditions form a dense layer constrained to the scaffold surface[76,95]. Perfusion of cells cultured in CCM drove the cells to distribute more uniformly into the scaffold, but did not significantly increase total cell number, suggesting that the enhanced distribution of the cells was primarily due to enhanced cell migration into the scaffold. With the exception of scaffolds cultured in CCM, the calculated cell population in scaffolds cultured under static conditions were lower than the initial seeding number. However, cultivation in the

perfusion bioreactors was able to rescue cell number in DMSO, GW-pSi, GW-media scaffolds. A greater commitment towards the osteogenic lineage has been associated with a reduction in hMSCs proliferation rates, which could explain the reason DMSO, GW-pSi, and GW-media scaffolds had lower cell populations than the scaffolds cultured in CCM[63,64,96]. Furthermore, insufficient gas and nutrient transport during the initial overnight static culture of the perfused samples is likely responsible for cell number being lower than the initial seeding number in DMSO, GW-pSi, and GW-media scaffolds.

The anabolic bone ECM derived from GW9662 treated hMSCs has been shown to upregulate the expression of osteogenic markers and improve bone repair in murine critical size-defect models[46,47]. The use of GW9662-eluting microspheres and perfusion bioreactors to prepare scaffolds with the anabolic bone ECM provides important information to inform translation of this technology to the clinic. We hypothesized that the controlled release of GW9662 and the subsequent deposition of ECM would result in improved osteogenic differentiation of seeded hMSCs. Consistent with previous in-vivo work[46], we observed BMP2 gene expression increase in response to GW9662 (exogenous and from microspheres) in static conditions. Although BMP2 gene expression was lower in GW9662-treated samples under perfused conditions, immunoblotting revealed a synergistic relationship between perfusion and GW9662 treatment. ALP expression in response to GW9662 treatment has been previously shown to be biphasic, becoming inhibitory at higher GW9662 concentrations[44]. Thus, it was unsurprising to see GW-pSi samples having a higher ALP expression than both GW-media and DMSO scaffolds under static conditions. Although the static DMSO and GW-media scaffolds had comparable

levels of ALP expression, both were still positively expressed. Furthermore, application of fluid shear stress significantly increased ALP expression in all three scaffolds.

Similarly, gene expression levels for OPN and OCN increased in response to perfused culture in GW-pSi and DMSO scaffolds. Expression of these two late osteogenic markers in perfused GW-media scaffolds was more complex. While OPN expression benefited from perfusion, OCN expression decreased. However, it should be noted that OCN expression in perfused GW-media scaffolds were still highly expressed. For Coll VI, Coll XII, BMP2, and OCN, the interaction was found to be significant, thus the effects of either variable depended on the other. Specifically, the upregulation of Coll VI, Coll XII, and BMP2 expression by GW9662 under static conditions were diminished under perfusion (*cf* **Figure 2.5, Figure 2.6A-B**). When investigated further at the protein level, however, Coll VI, Coll XII, and BMP2 expression was augmented by the dual treatment of GW9662 and perfusion. The mismatch in expression between the transcription and protein level highlights the limitations of utilizing gene expression data in understanding the interaction between perfusion and scaffold/culture media formulations.

The mechanism by which the GW9662-induced anabolic bone ECM mediates the upregulation of BMP2 and other osteogenic markers is not entirely understood, nor is the influence of perfusion. Previous work, however, has shown that signal transduction in hMSCs treated with GW9662 is dominated by integrins and, presumably, their interaction with the newly deposited ECM[46]. In rodents, Coll VI has been shown to mediate osteoblast differentiation via the cell-surface receptor neural/glial antigen 2 (NG2) and several types of integrins[18,24]. Coll XII is crucial in regulating osteoblast polarization and cell-cell

interaction[43]. As others have shown, integrin activated MAPK/ERK plays a crucial role in BMP2 induction[97], and it is feasible to assume a similar mechanism is responsible for the osteoinductive properties of the anabolic bone ECM. Integrins (β1) and other adaptor proteins have also been implicated in mediating hMSCs response to mechanical stimulation[98]. For example, application of fluid shear stress has been shown to increase ALP activity and expression of osteogenic markers, along with activation of Focal Adhesion Kinase (FAK)[98]. In addition, Coll XII gene expression can be directly stimulated by mechanical strain[99]. As a PPARγ inhibitor, GW9662 has been shown to upregulate various early stage markers of osteogenesis by attenuating the negative crosstalk on cWnt signaling, allowing for the translocation of β-catenin to the nucleus[98]. Although there are multiple mechanotransduction pathways that mediate osteogenic differentiation, exposure to fluid shear stress can also result in the translocation of β-catenin[100] to the nucleus in hMSCs mediated by N-cadherin signaling rather than cWnt[101]. However, these studies are typically performed in a 2D system, highlighting the need to investigate and decouple stimuli stemming from osteogenic niche environments such as from the anabolic bone ECM presented here from mechanical stimuli. At this current time, it is unknown whether cell-to-cell (N-cadherin) or cell-to-ECM (integrin) signaling pathways dominate in our system, which combines fluid shear stress from the perfusion bioreactor through a 3D environment mimicking the ECM of anabolic bone, or how the indirect upregulation of cWnt via PPARγ inhibition fits into the complex adhesive signaling networks.

Given the critical function of ALP and OPN in mineralization and the potent ability of BMP2 to induce ectopic bone formation, we evaluated whether their favorable response

to GW9662-treatment and perfusion were associated with a similar increase in mineralization. While the microstructure of as-prepared scaffolds could be discerned, their bone mineral density could not be evaluated as they were below the contrast limits of the calibration phantoms. After three weeks of culture, however, the bone mineral densities of all scaffolds were within the detection limit. In agreement with the gene expression results, we found significantly elevated BMD levels in the GW-pSi and GW-media scaffolds relative to the DMSO scaffolds. Perfusion augmented BMD levels in DMSO, GW-pSi, and GW-media scaffolds. In addition, the exogenous GW9662 treated scaffolds were mineralized to a significantly higher degree than even the GW-pSi scaffolds under perfusion, further corroborating the existence of synergistic relationship between GW9662-treatment and perfusion. Exemplifying a structure-function relationship, the compressive mechanical properties of bone are highly correlated with mineral density[92,102]. Given that restoring weight-bearing functionality to damaged or diseased bone is a goal of bone tissue engineering, it was crucial to evaluate whether the augmented bone mineral density observed in the cultured scaffolds translated to improved mechanical properties. While perfusion and GW9662 treatment individually improved the compressive properties of the scaffolds, together they resulted in a significantly stiffer scaffold. The compressive moduli were still substantial lower than those reported for native bone, but that is to be expected for experiments representing early mineralization of the scaffolds.

2.5. Conclusion

Despite their limited availability and association with donor site morbidity, autologous bone grafts remain the gold standard treatment for bone repair. Engineering bone constructs large enough for clinical utility is a challenging goal, due in part to our incomplete understanding of the combined effects of soluble factors and fluid shear stress on bone development. In this study, we examined the influence of controlled release of GW9662, a PPARγ inhibitor, and perfusion on the deposition of an ECM rich in collagens characteristic of newly formed bone by human mesenchymal stem cells cultured on osteoinductive scaffold. A striking improvement in deposition of the anabolic bone ECM relative to static and vehicle controls showed a synergistic relationship between perfusion and GW9662 treatment, from either the drug-eluting microspheres or media supplementation, resulting in a scaffold that recapitulated both the inorganic and organic fraction of nascent bone. Future *in vivo* work is needed to determine whether Coll/MgHA scaffolds embedded with GW9662-eluting microspheres can incite native osteoprogenitors cells to deposit the anabolic bone ECM at levels that result in improved bone healing. In addition, the data presented here suggests that GW9662 treatment and a perfusion culture system can be utilized to deposit the anabolic bone ECM to augment the osteoregenerative properties of existing scaffolds.

3. CLAY NANOPARTICLES IN COLLAGEN NANOCOMPOSITE HYDROGEL SEQUESTER HMSC SECRETED FACTORS IN 3D MICROENVIRONMENT

3.1. Introduction

The limited availability and donor-site morbidity associated with bone autografts underscore the need to engineer alternative scaffolds for bone repair. With their hydrophilic polymeric networks, hydrogels are capable of mimicking the highly hydrated 3D microenvironment of native tissues, making them a promising biomaterial for regenerative medicine. Designing hydrogels with appropriate physical and bioactive properties for bone repair is an ongoing endeavor. Inspired by the inorganic composition of native bone tissue, incorporating inorganic nanoparticles meant to mimic or substitute for bone mineral such as calcium phosphate[103] (e.g. hydroxyapatite[29,30], tricalcium phosphates[31]), calcium sulfates[5], and bioactive glass[104] present a facile means in augmenting the physical properties of hydrogels. Although these nanomaterials also enhance the osteoconductive properties of their nanocomposite hydrogels, whether they are capable of inducing osteogenic differentiation has been debated[5,7,105–107].

Laponite, a synthetic 2D nanosilicate (nSi), are a particularly exciting class of nanomaterial as they have been shown to induce osteogenic differentiation in bone marrow derived human mesenchymal stems cells (hMSCs)[57,58] and adipose-derived MSCs[59] in 2D culture. However, the mechanism by which nSi impart their osteoinductive influence in 2D culture has not been entirely characterized. It has been hypothesized that nSi internalization and their subsequent dissolution into mineral constituents

$(Na^{+}_{0.7}[\,(Si_8Mg_{5.5}Li_{0.3}))_{20}(OH)_4]^{-0.7})$ affect downstream gene expression[58]. However, the transition to the 3D microenvironment of a hydrogel nanocomposite further complicates the nature of nSi-cell interaction due to competing nSi-matrix interactions and the possibility of nSi aggregation in physiological solutions [108–110].

When incorporated in hydrogels, nSi have been shown to enhance osteogenic differentiation of preosteoblasts[111] and of hMSCS[112], suggesting that nSi retain their osteoinductive capabilities in 3D culture. However, nSi possess a high surface-to-volume ratio and discotic charge distribution that allows them to readily tune the mechanical properties of both natural and synthetic hydrogels[113]. Stem cell commitment in 3D culture has been shown to be influenced by hydrogel stiffness[114,115] and stress relaxation rate[116]. Thus, it is attractive to speculate whether hMSCs differentiation in the 3D microenvironment of nSi nanocomposites is largely influenced by the perceived alterations in hydrogel bulk mechanical properties caused by nSi-matrix interaction instead of the direct nSi-cell interaction as proposed in 2D culture.

Here, we investigate the mechanism by which nSi induce osteogenic differentiation in a collagen-nSi (Coll-nSi) nanocomposite. Coll hydrogels were chosen as they are widely available, provide 3D microenvironments with excellent cellular viability, spreading, and can be remodeled by hMSCs. To mimic the network-fortifying properties of nSi in Coll hydrogels lacking nSi, the boundaries of hydrogels were mechanically anchored. In addition, nSi pretreatment of hMSCs was performed prior to encapsulation in Coll hydrogels to replicate nSi internalization and dissolution that would possibly occur in the Coll-nSi nanocomposites. Results showed that while matrix stiffening and nSi

internalization influence the osteogenic differentiation of hMSCs in 3D culture, a third interaction between nSi and hMSCs secretome in the extracellular space could play a major regulatory role.

3.2. Methods

3.2.1. Cell Culture

Bone marrow-derived hMSCs were acquired from the adult stem cell distribution center at the Texas A&M Health Science Center Institute for Regenerative Medicine in accordance with institutionally approved protocols. The hMSCs at passage 3 were cultured in complete culture media (CCM) consisting of alpha minimal essential medium (α-MEM, Invitrogen), 20% (v/v) FBS (Atlanta Biologicals), 2 mM L- glutamine (Invitrogen), and 100 U/ml penicillin plus 100 µg/ml streptomycin (HyClone) at a seeding density of 500 cells/cm^2. Culture media was changed every 2-3 days until cells reached 70-80% confluency, which were then recovered and used for 2D and 3D osteogenic cultures.

3.2.2. 2D Cultures Containing nSi and Osteoprotegerin (OPG) ELISA Assay

For 2D culture, hMSCs were seeded at a density of 1000 cells/cm^2 in 6-well plates (Corning), cultured in CCM until 70-80% confluency. hMSCs were then treated with 0, 50, or 100 µg/mL nSi suspended in osteogenic basal medium (OBM) consisting of CCM supplemented with 50 µg/mL of ascorbic acid and 5 mM β-glycerophosphate, for two days. Thereafter, OBM media was changed every two days. On days 2, 4, and 8, conditioned media was collected and stored at -80°C for downstream use in OPG ELISA (R&D Systems) following manufacturer instructions.

3.2.3. 3D Cultures in Coll-nSi Hydrogels

For 3D culture, a known number of hMSCs were resuspended in 5X DMEM (HyClone) solution and added to a hydrogel precursor solution at a concentration of 200,000 cells/hydrogel. Coll hydrogels and Coll-nSi nanocomposites containing 3.5 mg/mL of collagen type I were prepared using a previously described protocol with modifications[117]. For Coll hydrogels, a solution consisting of high concentration, acid-solubilized rat tail collagen type I (Corning), 25% (v/v) of 0.1 M acetic acid, 20% (v/v) of 5x DMEM, 10% (v/v) of reconstitution buffer (200 mM HEPES and 260 $NaHCO_3$), and 2% (v/v) of 1 M NaOH was homogenized by repeated pipetting. Nanocomposites with either 1% nSi (Coll-1% nSi) or 0.1% nSi (Coll-0.1% nSi) were prepared in a similar fashion. To fabricate Coll-1% nSil nanocomposite hydrogels, nSi were resuspended in the 5x DMEM and reconstitution buffer stocks at a concentration of 3.3% (w/v) prior to use.

To fabricate 0.1% (w/v) nSi nanocomposite hydrogels, a 0.5% nSi solution was prepared in the 5x DMEM. These solutions were sonicated and incubated overnight at 4 °C to avoid nSi aggregation prior to their use. Approximately 120 µL of the precursor hydrogel solution was pipetted into 1-cm silicone rubber molds laid in 6-well plates (Fig. 1) and placed in a humidified incubator at 37 °C for 90 minutes to promote gelation and fibril formation. Encapsulated hMSCs were cultured in CCM overnight before starting OBM treatment, with media changes occurring every two days thereafter in low-adhesion 6-well plates (Corning). Images of the hydrogels were taken over the course of 8 days during media changes to investigate cell-mediated hydrogel compaction. Changes in hydrogel diameter were analyzed using ImageJ (NIH Image).

3.2.4. Bioactivity of nSi in Coll and Coll-nSi Hydrogels

To decouple the effects of hydrogel compaction on osteogenic differentiation of encapsulated hMSCs, a portion of the hydrogels were allowed to remain in the silicone molds, which prevented gels from compacting. To gauge whether nSi treatment of hMSCs during 2D culture could improve their propensity to differentiate towards the osteogenic lineage in 3D culture, hydrogels were prepared using hMSCs that were pretreated with 100 μg/mL of nSi in CCM the day prior to encapsulation. A third group of hydrogels were prepared in which hMSCs were pretreated with nSi and were kept in the silicone molds. Including the control in which hMSCs were not pretreated with nSi and were cultured in hydrogels without the aid of the silicone molds, there were a total of four culture conditions. An illustration depicting the three types of hydrogels with varying nSi percentage and the four culture conditions are shown in **Figure 3.1**.

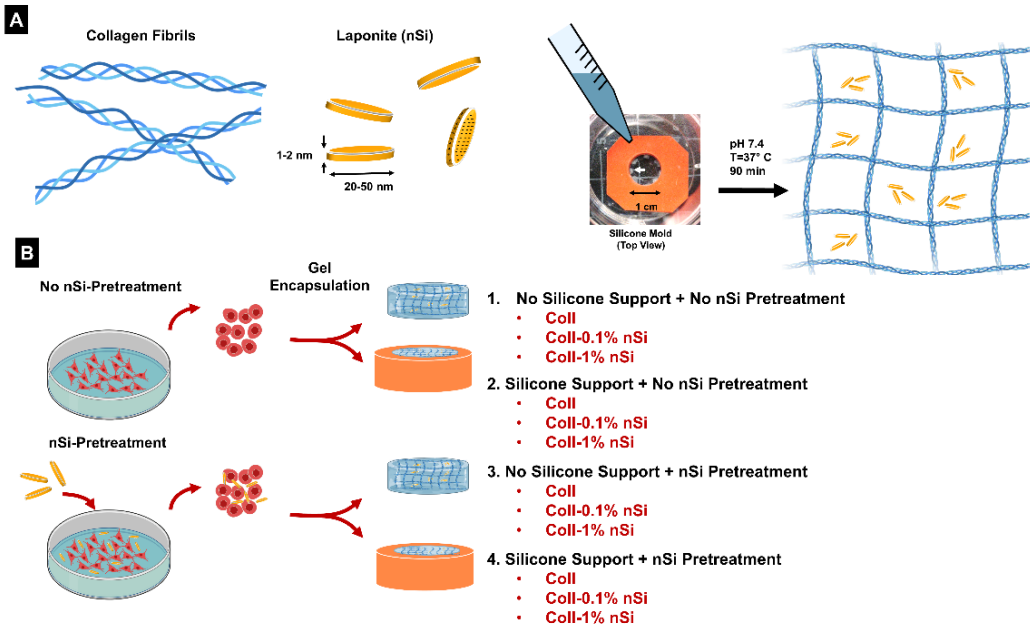

Figure 3.1: A) Fabrication of Collagen-nSi (Coll-nSi) nanocomposite hydrogels. Three different precursor hydrogel solutions with varying nSi percentage were pipetted into silicone mold seated on a silicone sheet (white arrow indicates dried collagen used for anchoring). B) Illustration of the four different culture condition; half of hMSCs cultures were pretreated with nSi, while half of the gels were kept in the silicone mold as a mechanical support.

3.2.5. Alkaline Phosphatase Kinetic Assay and Staining

Alkaline phosphatase (ALP) kinetic assay was measured using a colorimetric assay as previously described[118]. Briefly, after 8 days of OBM treatment, hMSCs cultured in 6-well plates were washed twice with PBS and once with ALP buffer consisting of 100 mM Trix-HCl, 100 mM KCl, 1 mM of $MgCl_2$. To start the reaction, 1 mL of ALP buffer warmed to 37°C and an equal volume of 1-Step p-itrophenyl phosphate (PNPP) substrate (Thermo Fisher Scientific) was added to each well and absorbance at 405 nm was measured every 30 seconds over the course of 15 minutes using an Infinite M200 Pro plate reader (Tecan). Wells were then washed with PBS and stored at -20°C to use downstream for cell number quantification. This protocol was modified for measuring ALP activity in

3D cultures. Cell-laden hydrogels were washed as described above, but kept at 37°C for 10 minutes between washes to maintain cell viability. Hydrogels were homogenized using 1 mL ALP buffer supplemented with 0.1% Triton-X 100 and a microcentrifuge pestle. Approximately 100 µL from each sample was reserved and stored at -20°C for cell number quantification. An equal volume of 1-Step PNPP substrate was added to the remaining sample, and was stored at 4°C on a tube revolver for 36 hours. For manual kinetic measurement, several 50 µL aliquots were taken from the samples after brief centrifugation and analyzed as previously described[118]. Results were normalized by cell number. ALP staining was also performed on monolayer samples after 8 days of culture with nitroblue tetrazolium/5-bromo-4-chloro-3-indolyl phosphate (NBT/BCIP 1-steps solution, Thermo Fisher) following the manufacturer instructions. ALP-stained monolayers were visualized with a Zeiss stereomicroscope.

3.2.6. Cell Number Quantification

Monolayer cultures stored at -20°C were removed and washed with warmed PBS. Samples were then lysed using a buffer consisting of PBS supplemented with 1 mM $MgCl_2$ and 0.1% Triton-X 100 (Sigma Aldrich). Samples were homogenized through vortexing for 15 seconds. Diluted aliquots of the lysed samples were pipetted to a Black Nunc 96-well fluorescent plat (Thermo Fisher Scientific). An equal volume of CyQUANT buffer consisting of 2X CyQUANT dye (CyQUANT Cell Proliferation, Invitrogen) was added to each sample. A standard from a known number of hMSCs was prepared in a similar fashion through serial dilutions. The fluorescence was read on an Infinite M200 Pro plate reader (Tecan) at 480/520 nm excitation/emission. Cell number from 3D cultures were

analyzed similarly. Hydrogels were homogenized using 1 mL of lysis buffer and a microcentrifuge pestle. Approximately 100 µL from each sample was reserved and analyzed as described above.

3.2.7. Immunoblotting

After 8 days of culture in OBM, hMSCs cultured in 6-well plates were washed with warm PBS followed by ice-cold PBS. Proteins were extracted using ice-cold RIPA buffer (50 mM Tris HCl, 150 mM NaCl, 1% Triton-X-100, 0.1% SDS, 0.5% Sodium Deoxylcholate, 1 mM EDTA, 1 mM Sodium Pyrophosphate) supplemented with SIGMAFAST^{TM} protease inhibitors (Sigma-Aldrich) through vortexing for 30 seconds. The homogenized cell lysates were stored at -80°C until total protein content was quantified through Pierce BCA Protein Assay kit (Thermo Fisher Scientific). Proteins were extracted from hMSCs-laden hydrogels in a similar fashion. Briefly, hydrogels were washed twice with warm PBS and incubated at 37 °C for 10 minutes before transferring to a 1.5 mL microcentrifuge tube. Hydrogels were then homogenized with ice-cold RIPA buffer and a microcentrifuge pestle. After protein quantification, 4X SDS sample buffer (150 mM Tris-HCl, 25% glycerol, 12% SDS, 0.05% bromophenol blue, and 6% β-mercaptoethanol) was added to extracted proteins at a 1:3 ratio. Approximately 20 µg of protein were resolved in hand-casted 12% SDS-PAGE gels, and transferred to a PVDF membrane (Millipore). The membrane was blocked in 5% milk in TBST buffer (20 mM Tris-base, 150 mM NaCl, 0.2% Tween 20) for one hour before being incubated overnight at 4 ºC with mouse anti human BMP2 antibody (R&D Systems) diluted (1:500) in blocking buffer. After 3 washes in TBST buffer, the membrane was incubated for 1 hour

with an HRP-conjugated goat anti mouse secondary antibody (Protein Tech). The membrane was developed for 5 minutes in WesternSure Chemiluminescent Substrate (LI-COR) and imaged on a C-Digit Blot Scanner (LI-COR). After imaging, the membrane was stripped using Restore Stripping Buffer (Thermo Fisher Scientific) following the manufacturer's instructions. The membrane was then blocked, incubated with mouse-anti-human GAPDH (Protein Tech, 1:4000), and imaged as previously described. Similar process was repeated with rabbit anti human osteopontin (Protein Tech) (1:1000) and mouse anti human VEGFA (Protein Tech) (1:1000) antibodies.

3.2.8. In vitro Mineralization

After 21 days culture in OBM, hMSCs grown in 6-well plates were washed twice with warmed PBS and were then fixed with 4% formaldehyde in PBS for 30 minutes at room temperature. The samples were then washed once with PBS, followed by two additional times with diH_2O. The samples were then incubated for 30 minutes at room temperature with gentle rocking with 1 mL per well of 40 mM of Alizarin Red S (Sigma Aldrich) in diH_2O, pH adjusted to approximately 4.2 using 0.5 M NH_4OH. Monolayers were then washed 4 times with diH_2O, 10 minutes with gentle rocking for each wash. The ARS-stained monolayers were visualized with a Zeiss stereomicroscope. ARS dye was then extracted using 10% acetic acid solution and quantified via colorimetric detection at 405 nm as previously described[119]. The calcium content of collagen-nSil hydrogels was measured using an o-Cresolphthalein-calcium reaction assay (Cayman Chemicals) after 21 days of culture in OBM. Briefly, samples were fixed at room temperature for 1 hour in 4% formaldehyde in PBS. Samples were then washed three times with diH2O before being

dried for 48 hours in a desiccator. Calcium was extracted from dried samples by undergoing an overnight acidic digestion at 4°C using 0.5 M HCl on a tube rotator. Samples were centrifuged prior to collecting the supernatant for downstream use.

3.2.9. Physical and Chemical Characterization

All rheological testing was performed on a Physica MCR 301 (Anton Paar) rheometer with a 1 cm parallel plate attachment. Hydrogels without cells were prepared the day before testing and were kept overnight in PBS in a humidified incubator. A strain sweep from 0.1 to 10% at 1 Hz and a frequency sweep from 0.1 to100 Hz at 1% strain were performed to characterize the linear viscoelastic behavior of the hydrogels. Fibrillar structure was imaged using confocal reflectance microscopy (Nikon D Eclipse C1 upright microscope). Fourier-transform infrared (FTIR) spectroscopy was utilized to further characterize interaction between nSi and collagen network. After crosslinking, hydrogels were washed three times with diH_2O, desiccated for 48 hours, and flattened into thin disks using a mortar and pestle for FTIR analysis (Alpha Bruker Spectrometer).

3.2.10. Metabolically Labeled Proteins and Actin Staining

Secreted proteins within collagen nanocomposite hydrogels were visualized using the fluorescent non-canonical amino acid tagging (FUNCAT) technique as previously described[120,121]. Briefly, hMSCs encapsulated in collagen-nSi hydrogels were cultured with OBM supplemented with 100 mM of azidohomoalaine (AHA), an azide-conjugated methionine analogue (Click Chemistry Tools). After 8 days of culture, hMSC-laden hydrogels were washed twice with 1% bovine serum albumin (BSA) in PBS with the samples kept at 37°C for 10 minutes for the duration of the washes. Samples were then

incubated with 30 μM DBCO-488 (Click Chemistry Tools), a fluorophore-conjugated dibenzocyclooctyne, in 1% BSA solution for 1 hour to undergo copper-free click-reaction with azide-labeled proteins. Samples were washed two additional times with warmed PBS before fixing with 4% formaldehyde in PBS for 1 hour at room temperature. Samples were washed three times in PBS before being permeabilized with 0.1% Triton-X 100 (Sigma Aldrich) for 1 hours at room temperature. Samples were then co-stained with Alexa-Fluor 543 Phalloidin (Life Technologies) according to the manufacturer's instructions to facilitate distinction between cellular and extracellular proteins in confocal images (Nikon D Eclipse C1 upright microscope). Confocal reflectance microscopy was used to visualize the established collagen matrix and distinguish from nascent ECM. The relative fluorescence intensity of nSi in Coll-1% nSi nanocomposites were measured using ImageJ (NIH Images) through manual segmentation (4-7 images per condition, a total of 60-70 nSi discrete regions analyzed per condition). Statistical analysis was performed via Kruskal-Wallis non-parametric test, followed by Dunn's multiple comparison test ($p<0.05$).

3.3. Results

3.3.1. Dose-dependent effects of nSi in hMSC Monolayers

After 2 days of culture, the number of hMSCs were similar between the control (no nSi) and the samples treated with 0.1 and 1% nSi (**Figure 3.2A**). Thereafter, nSi had a negative impact on cell number that was dose-dependent, likely due to a decrease in cell proliferation rate. Osteoprotegerin (OPG), an early osteogenic marker, detected in collected media was significantly lower in both nSi treatment groups in comparison to the

control OBM (**Figure 3.2B)** after 2 days of culture. However, by days 4 and 8 both nSi treatment groups secreted significantly higher levels of OPG than the OBM control (**Figure 3.2B**). Immunoblotting against BMP2 revealed two distinct molecular weights of approximately 46 and 33 kDa, corresponding to different stages of BMP2 post-translational modifications and maturity[122,123] (**Figure 3.2C**). The normalized BMP2 band signal of the 46 kDa variant was found to be comparable between the OBM control and the hMSCs treated with nSi. However, hMSCs treated with 100 μg/mL nSi had a significantly higher expression of the 33 kDa BMP2 isoform in comparison to the OBM control and the 50 μg/mL nSi treatment group.

ALP staining revealed that although the hMSCs in the OBM control expressed ALP homogeneously throughout the monolayer, hMSCs treated with nSi contained darker regions that increased in area with the higher dose of nSi (**Figure 3.2D**). ALP kinetic assay corroborated staining results. It was shown that nSil treatment upregulated the activity of ALP, with 100 μg/mL nSi having a significantly higher activity than the OBM control (**Figure 3.2E**). A similar trend was observed when investigating the ARS-stained, mineralized monolayers. After 21 days culture, the confluent monolayers of the OBM control contained several mineralized nodules (**Figure 3.2F**). Akin to the ALP staining results, these mineralized nodules increased in size and intensity in the nSi treated monolayers. Recovery and quantification of the ARS dye showed nSi treatment significantly increased mineralization in monolayer (**Figure 3.2G**).

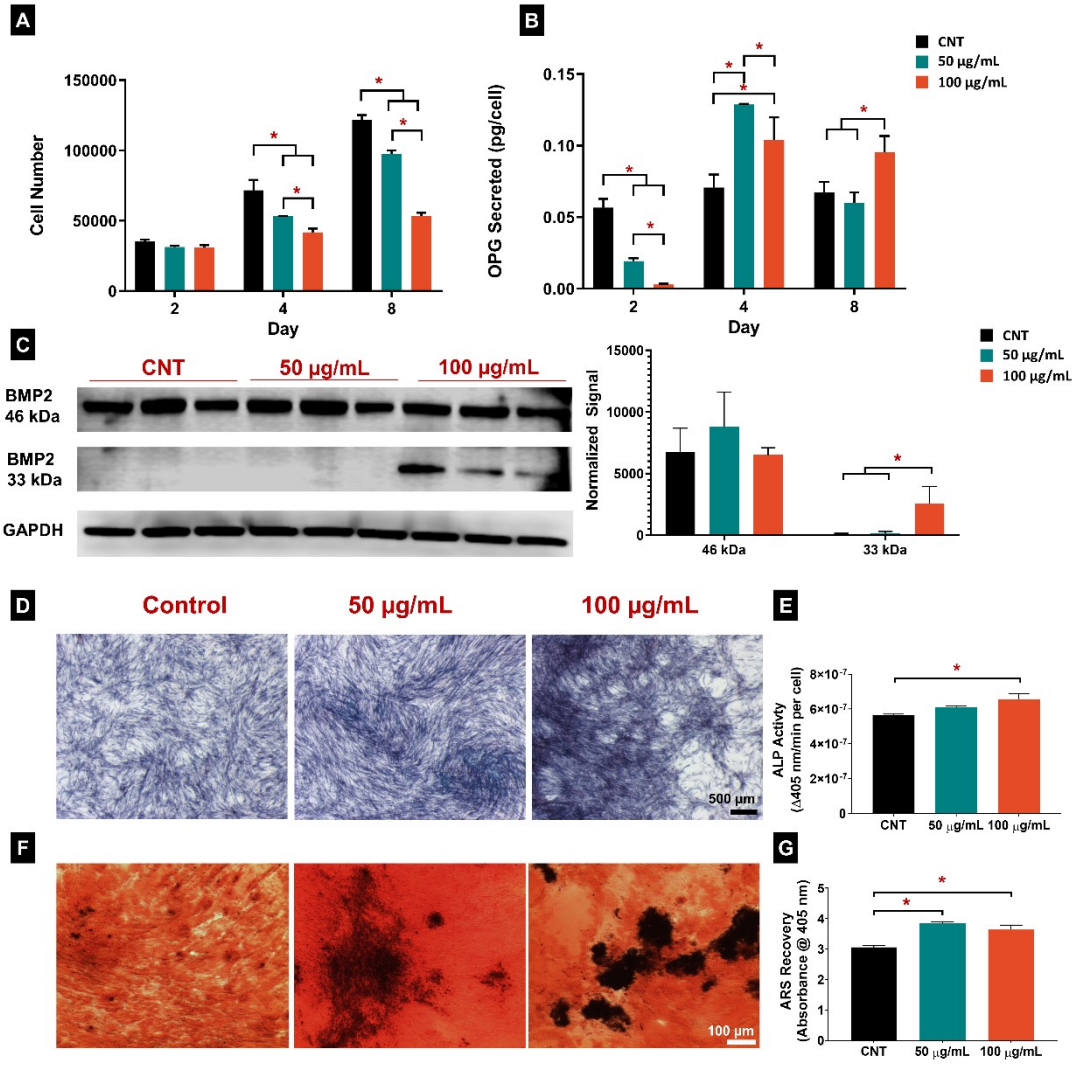

Figure 3.2: Effects of nSi treatment on hMSCs in monolayer culture. A) hMSCs population over 8 days of osteogenic culture. B) OPG secreted by hMSCs over 8 days of osteogenic culture. C) Immunoblotting against BMP2 of hMSCs lysates after 8 days of culture (left) and normalized band signals (right). D) Representative images of ALP-stained monolayers after 8 days of osteogenic culture. E) ALP activity after 8 days of osteogenic culture in monolayer. F) Representative ARS-stained hMSCs monolayers after 21 days of osteogenic culture. E) Spectrophotometric quantification of recovered ARS staining. Statistical testing was performed by one-way ANOVA, followed by a Tukey's multiple comparison. Asterisks depict statistically significant (n=3, error bars depict standard deviation).

3.3.2. Characterization of Collagen-nSil Network

The interaction between the nSi and collagen was investigated via FTIR (**Figure 3.3A**). Several prominent bands observed in the collagen samples were characteristic of amides[36], specifically at 3300 cm^{-1}, 1630 cm^{-1}, 1540 cm^{-1}, and 1250 cm^{-1}. With the exception of the vibrational band at 1250 cm^{-1}, the aforementioned bands were also present in the 0.1% and 1% nSi nanocomposite hydrogels. Upon incorporating nSi to the collagen hydrogels, a strong peak at approximately 1000 cm^{-1} was observed, corresponding to O-Si-O bending of the nSi[124]. Interestingly, the 1250 cm^{-1} vibrational band, corresponding to the amide III envelope, became more obscure with higher concentration of nSi (**Figure 3.3A)**. The amide III envelope is sensitive to the ratio between secondary protein structures, e.g. α-helix and β-sheet, and disordered structures, e.g random coil, with a larger band indicating a higher degree of disorder[125]. This would indicate the nSi reinforce collagen secondary protein structures in the Coll-nSi nanocomposites. of Confocal reflectance microscopy was used to visualize the crosslinked network of the collagen nanocomposites. As expected, the microstructure of the collagen hydrogel was made up of a densely woven network of isotropic-aligned collagen fibrils. The addition of the nSi did not affect the formation of alignment of the collagen network, However, incorporating nSi resulted in visible clusters that increase in frequency and size upon higher concentration of nSi (**Figure 3.3B)**.

3.3.3. Mechanical Characterization

Rheological testing was performed to characterize alterations in the viscoelastic properties of the collagen network upon the inclusion of nSi. A strain sweep revealed the collagen and collagen-0.1% nSi hydrogels had similar response to the oscillatory strain sweep (**Figure 3.3C**). Briefly, both had comparable average storage moduli (G') (**Figure 3.3F**) and average yield strain occurring after 1% (**Figure 3.3D**). In contrast, the 1% nSi nanocomposite hydrogels had a significant five-fold increase in the average G' (**Figure 3.3F**). However, the linear viscoelastic region (LVE) for the 1% nSi nanocomposite hydrogel was smaller, as its average yield strain occurred before 1% (**Figure 3.3D**). Further rheological characterization performed with a frequency sweep. (**Figure 3.3E**). Verifying the strain sweep results, the 1% nSi nanocomposite hydrogels had a higher G' than either of the collagen and collagen-0.1% nSi hydrogels. Furthermore, all three collagen hydrogel compositions were shown to be frequency-dependent.

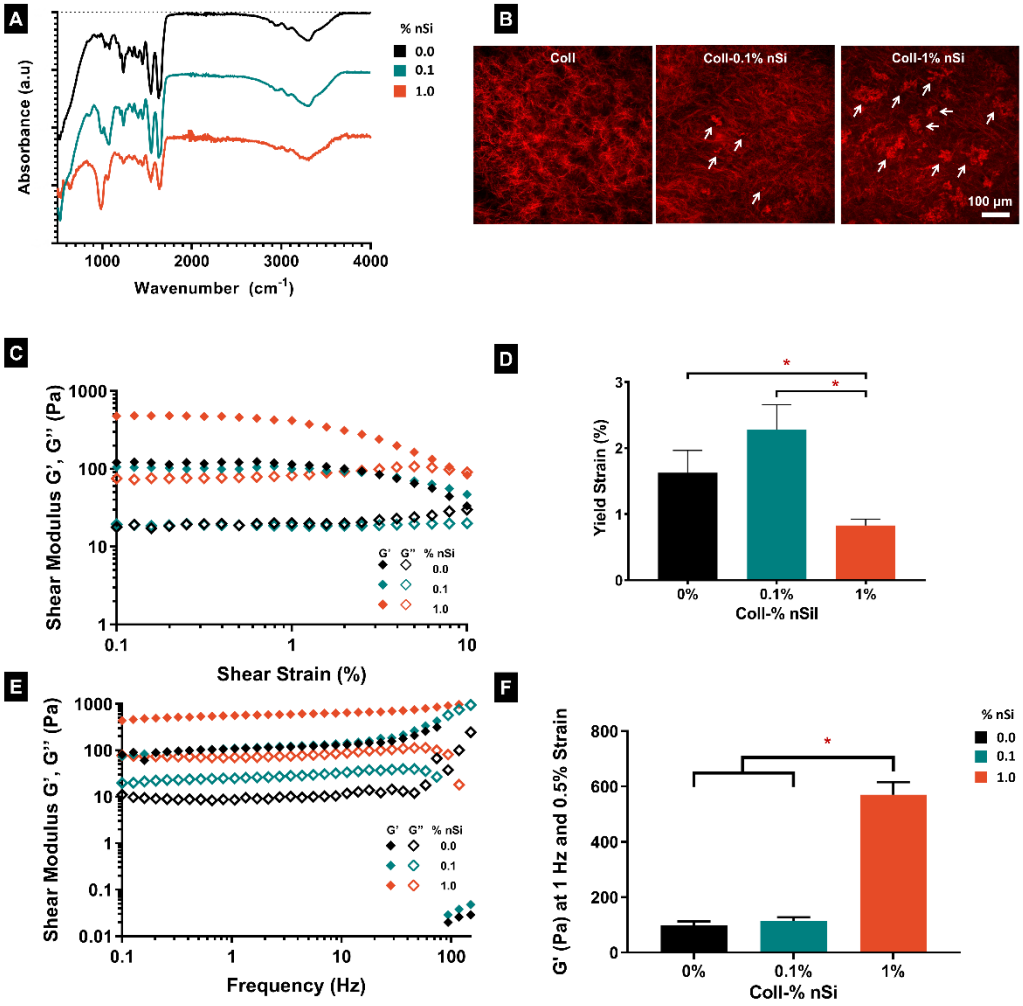

Figure 3.3: Chemical and rheological characterization of Coll-nSi nanocomposite hydrogels A) FTIR analysis of lyophilized nanocomposite hydrogels indicate presence of both protein (amides 3300 cm^{-1}, 1650 cm^{-1}, 1530 cm^{-1}, and 1250 cm^{-1}) and nSil (~1000 cm^{-1}). B) Confocal reflectance reveals nSil are heterogeneously distributed in collagen gels and disrupt fibril microstructure (scale bar 50 µm). Representative data shown for C) strain sweep and E) frequency sweeps. D) Average yield strain for the collagen and collagen-nSi hydrogels defined as a 10% deviation in G'. F) Average storage modulus Statistical testing was performed by one-way ANOVA, followed by a Tukey's multiple comparison. Asterisks depict statistically significant (n=3, error bars depict standard deviation).

3.3.4. Hydrogel Compaction and Actin Staining

We then investigated whether the observed increase in bulk G' would translate to different cellular behavior or phenotype between hydrogel composition. Representative images of cell-mediated hydrogel compaction are depicted in **Figure 3.4A**. Hydrogel compaction measured over the course of 8 days was significantly lower in the 1% nSil hydrogel compared to collagen control and the 0.1% nSi nanocomposite (**Figure 3.4B**). Confirming the rheological results, the collagen control and the 0.1% nSi nanocomposite experience similar levels of hMSC-mediated hydrogel compaction. Actin staining was performed to verify the differences in hydrogel compaction were not a result of compromised hMSC **Figure 3.4C-D**). After 8 days of culture within compacted collagen and collagen-0.1% nSi hydrogels, actin-stained hMSCs were densely packed. Furthermore, hMSCs exhibited arched stress fibers. In contrast, hMSCs cultured in the collagen-1% nSil hydrogels were not as densely packed and did not display the curved stress fibers (**Figure 3.4C**). Preventing cell-mediated hydrogel compaction with the use of the silicone molds did not result in crimped stress fibers in hMSCs in either of the three hydrogel formulations (**Figure 3.4B**). However, a lower cell density was observed in the 1% nSil hydrogels.

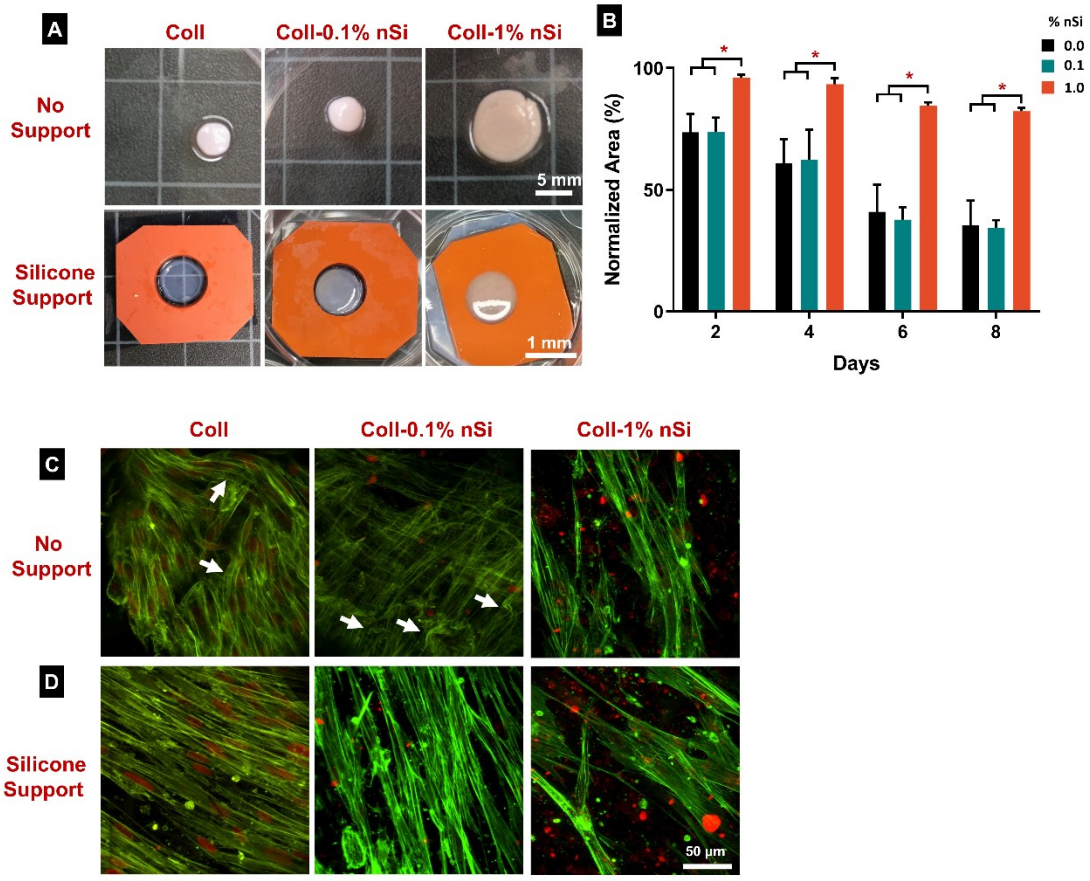

Figure 3.4: A) Representative images of hydrogels with and without silicone support after 4 days of culture. B) Quantified hMSCs-mediated compaction of hydrogels cultured without silicone support determined by changes in area. Statistical testing was performed by one-way ANOVA within individual days, followed by a Tukey's multiple comparison (n=3, error bars depict standard deviation, $p<0.05$). C) Hydrogel compaction results in arched stress fibers in collagen and 0.1% nSi hydrogels. hMSCs cultured in the 1% nSi hydrogels without the use of the silicone support did not have the arched stress fibers. D) hMSCs alignment is observed in silicone-supported gels; crimped stress fibers no present.

3.3.5. ALP Activity and Mineralization of hMSCs in 3D Coll-nSi Hydrogels

To evaluate the differentiation of hMSCs towards the osteogenic lineage in the nanocomposites, early and late hallmarks of osteogenesis were investigated. Briefly, an ALP kinetic assay was performed on encapsulated hMSCs after 8 days of culture (**Figure 3.5A**). A three-way ANOVA indicated that the three variables—nSi concentration in the

gels, the use of the silicone support, and pretreating hMSCs with nSi—each had a significant impact on ALP activity (**Table Appendix 24**). A more detailed analysis was performed with a Tukey's multiple comparison, although four types comparison are highlighted in **Figure 3.5** to better evaluate the effects of the individual variables. These include:

1. Comparison between gels with varying nSi percentage within the same culture condition. Significant difference indicated by * ($p<0.05$).
2. Comparison to the culture condition without silicone support and no pretreatment. Significant difference indicated by # ($p<0.05$).
3. Comparison to the culture condition with the silicone support and no pretreatment, Significant difference indicated by ¶ ($p<0.05$).
4. Comparison to the culture condition pretreated with nSi but lacking silicone support. Significant difference indicated by ‡ ($p<0.05$).

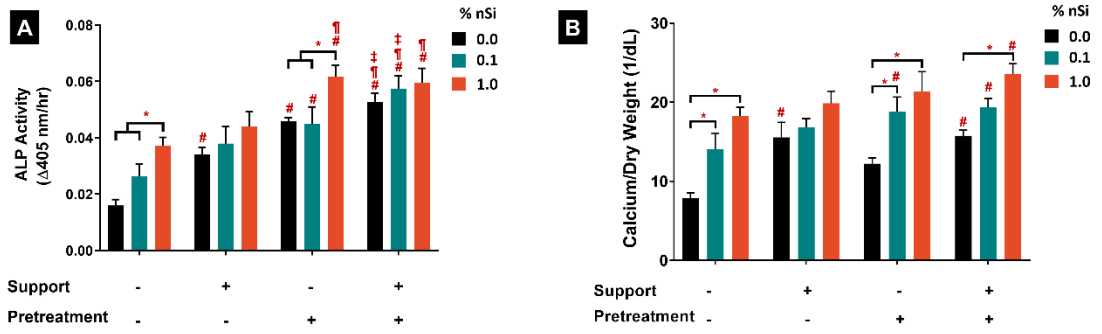

Figure 3.5: A) ALP activity of hMSCs after 8 days of 3D culture. B) Calcium content after 21 days of 3D culture. For ALP activity and calcium content, statistical analysis was performed by three-way ANOVA, followed by a Tukey's multiple comparison test (n=3). Error bars depict standard deviation. Four types of comparisons are emphasized in the figure and were assigned unique symbols when a significant difference ($p<0.05$) was discovered. These include: * when comparing gels with varying nSi percentage within the same culture condition, # when comparing to the culture condition without silicone support and no pretreatment, ¶ when comparing to the culture condition with the silicone support and no pretreatment, and ‡ when comparing to the culture condition pretreated with nSi but lacking silicone support. The comparisons between culture conditions (#, ¶, ‡) was performed between gels of the same Coll-nSi formulation.

ALP activity increased in response to increasing nSi gel percentage, resulting in significantly higher activity in Coll-1% nSi gels compared to Coll and Coll-0.1% nSi gels in two of the four culture conditions—in gels with neither silicone support nor nSi pretreatment and in gels pretreated with nSi but not provided the silicone support (**Figure 3.5A**). Furthermore, it was discovered that while the use of just the silicone support generally increased ALP activity in comparison to gels cultured with neither the silicone support nor nSi pretreatment, the increase was significant in only the case of Coll gels (**Figure 3.5A**). In contrast, nSi pretreatment in the absence of a silicone support significantly elevated ALP activity in all three gel formulations in comparison to the gels cultured with neither the silicone support nor nSi pretreatment. Furthermore, ALP activity of Coll and Coll-0.1% nSi hydrogels cultured with just the silicone support was

comparable to when they were cultured with just nSi pretreatment. For Col-1% nSi hydrogels, however, the nSi pretreatment stimulated ALP activity to significantly higher levels compared to when a silicone support was provided, as indicated by ¶ (**Figure 3.5A**). Providing both silicone support and nSi pretreatment had a synergistic effect on ALP activity for Coll and Coll-0.1% nSi gels, resulting in significantly higher levels compared to the other three culture conditions, as indicated by #, ¶, and ‡ (**Figure 3.5A**). The ALP activity of Coll-1% nSi gels when provided both silicone support and nSi pretreatment was comparable to levels observed in the no silicone support/ nSi pretreatment condition.

After 21 days of culture, the calcium content of the mineralized scaffolds was quantified using o-cresolphthalein colorimetric assay (**Figure 3.5B**). A three-way ANOVA revealed that the three variables—silicone-support, nSi-pretreatment, and the percentage of nSi in the hydrogels—each had a significant effect on calcification (**Table Appendix 25**). Similar to ALP kinetic analysis, a Tukey's multiple comparison was performed. The same four types of comparisons and corresponding symbols indicating significance were used. Coll-1%nSi hydrogels were found to be mineralized to a significantly higher degree than the Coll hydrogels, regardless of whether hMSCs were pretreated with nSi prior to encapsulations. Mineralization increased in response to increasing nSi gel percentage, resulting in significantly higher activity in Coll-1% nSi gels compared to Coll and Coll-0.1% nSi gels in three of the four culture conditions: in gels with neither silicone support nor nSi pretreatment, in gels pretreated with nSi but not provided the silicone support, and in gels provided both the silicone support and nSi pretreatment (**Figure 3.5B**).

Calcification in Coll-0.1% nSi nanocomposites was also significantly higher than in Coll hydrogels in two of the four culture conditions—in gels with neither silicone support nor nSi pretreatment and in gels pretreated with nSi but not provided the silicone support (**Figure 3.5B**). The use of just the silicone support resulted in a dramatic increase in the calcium content of Coll-gels in comparison to the culture condition with neither the silicone support nor nSi pretreatment (**Figure 3.5B**). The use of just the silicone support did not have a significant impact on the mineralization of the Coll-0.1% nSi and Coll-1% nSi nanocomposites. Pretreatment with nSi in the absence of a silicone support significantly elevated calcium content of Coll-0.1% nSi nanocomposite in comparison to its counterparts cultured with neither the silicone support nor nSi pretreatment (**Figure 3.5B**).

Calcification in Coll and Coll-1% nSi hydrogels pretreated with nSi in the absence of the silicone support was similar to levels observed in the culture condition with neither the silicone support nor nSi pretreatment. Furthermore, there was no statistical difference in the calcification of gels cultured with just the silicone support with that of gels just pretreated with nSi (**Figure 3.5B**). Pretreatment with nSi used in conjunction with silicone support caused significantly higher mineralization in all three gel formulations in comparison to their counterparts cultured with no silicone support and no nSi pretreatment (**Figure 3.5B**). However, calcium content for gels provided silicone support and nSi pretreatment was comparable to their counterpart gels provided either the silicone support or nSi pretreatment (**Figure 3.5B**).

3.3.6. Immunoblotting of BMP2 and Osteopontin

Immunoblotting against BMP2 was performed after 8 days of 3D culture. Similar to the results observed in monolayer (*cf*. Figure 1C), two distinct molecular weights of BMP2 were observed (**Figure 3.6A-D**). The bands located at 46 kDa were inconsistently expressed in Coll and Coll-0.1% nSi hydrogels cultured without the silicone support and without nSi pretreatment (**Figure 3.6A**). However, expression of the 46 kDa BMP2 isoform could be improved with aid of the silicone support (**Figure 3.6B&D**). Pretreatment of hMSCs with nSi had an inconsistent effect, upregulating BMP2 expression in Coll-0.1% nSi hydrogels while having no effect on Coll hydrogels (**Figure 3.6C**). In contrast, Coll-1% nSi hydrogels consistently expressed the 46 kDa BMP2 isoform in all four culture conditions. Furthermore, a 13 kDa BMP2 variant, corresponding to secreted BMP2, was detected only in the Coll-1% nSi hydrogels. Densiometric analysis confirmed expression of both BMP2 isoforms was significantly upregulated in the Coll-1% nSi hydrogels in comparison to the Coll control and the Coll-0.1% nSi.

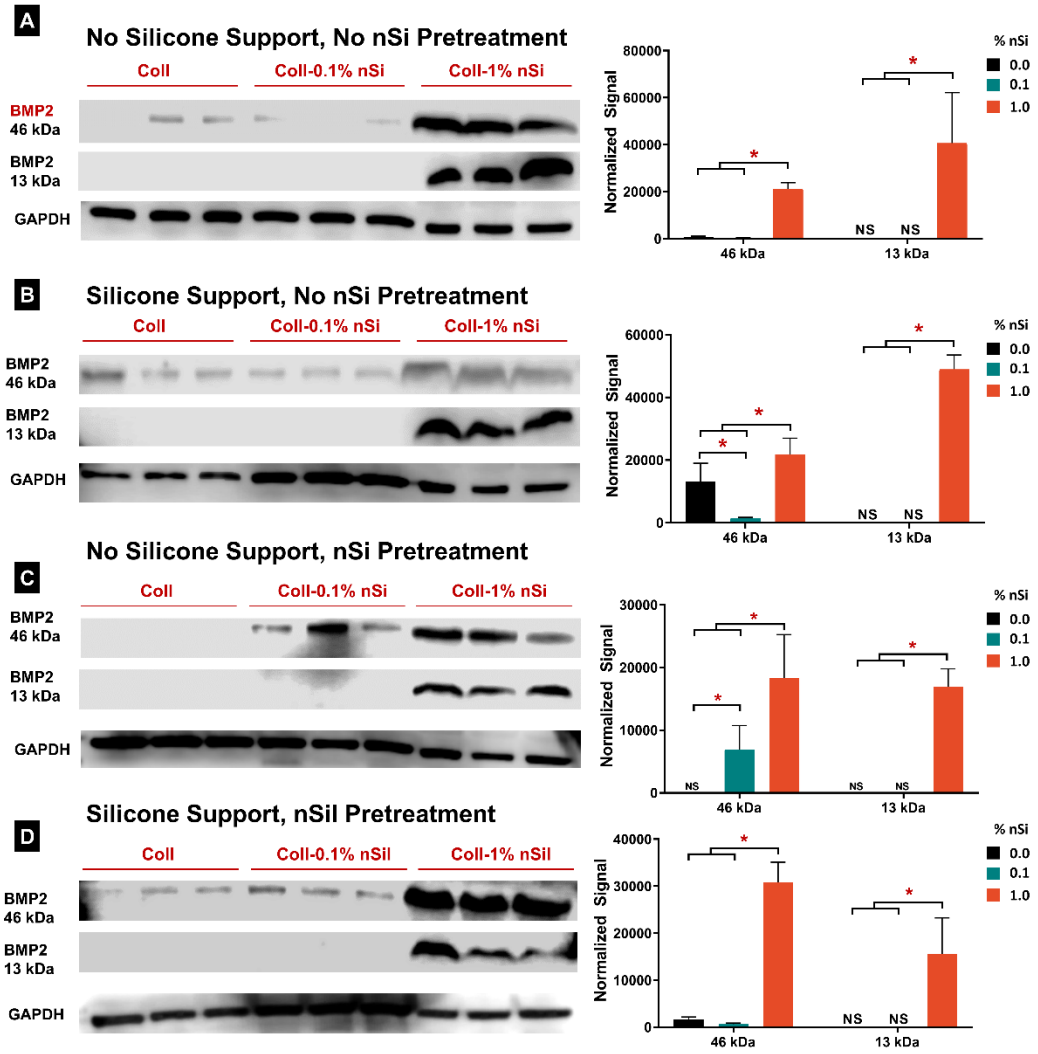

Figure 3.6: Immunoblotting against BMP2 after 8 days of 3D culture in Coll and Coll-nSIl hydrogels A) without the silicone support or nSi pretreatment, B) with silicone support and no nSi pretreatment, C) without silicone support and nSi pretreatment, and D) with both silicone support and nSi pretreatment; corresponding densiometric analysis are shown on the right. Two distinct isoforms of BMP2 were detected (46 kDa, 13 kDa), which were consistently upregulated in the Coll-1% nSi hydrogels. Statistical analysis was performed by one-way ANOVA within each BMP2 isoform, followed by a Tukey's multiple comparison. Error bars depict standard deviation (n=3), and asterisks signify a significant difference ($p<0.05$).

Osteopontin (OPN) expression was also investigated after 8 days of 3D culture (**Figure 3.7**). Three distinct isoforms of OPN were detected (72 kDa, 40 kDa, and 32 kDa),

which are consistent with the proteolytic cleaving of osteopontin.[126] However, OPN was reliably expressed to only in the Coll-1% nSil hydrogels (**Figure 3.7A-D**). In contrast, OPN expression was not detected in Coll and Coll-0.1% nSi hydrogels in three of the four culture conditions (**Figure 3.7A-C**). The exception occurred when Coll and Coll-0.1% nSi hydrogels were cultured with hMSCs pretreated with nSi and were anchored to the silicone support (**Figure 3.7D**). The corresponding densiometric analysis of the normalized bands indicated that hMSCs cultured on Coll-1% nSi hydrogels expressed OPN to a significantly higher degree than in Coll and Coll-0.1% nSi hydrogels in all culture conditions (**Figure 3.7E-H)**.

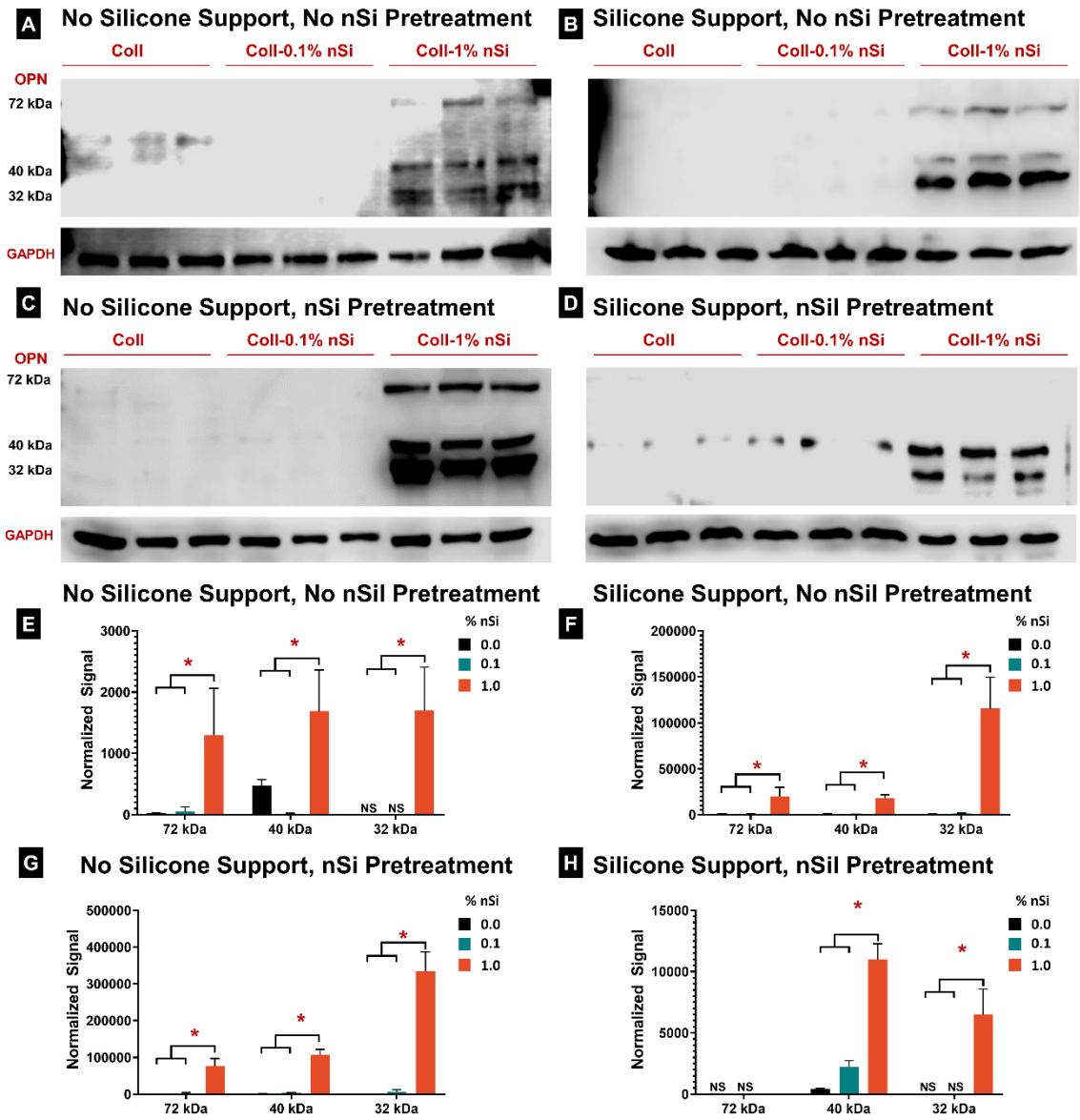

Figure 3.7: Immunoblotting against osteopontin (OPN) after 8 days of 3D culture in Coll and Coll-nSi hydrogels A) without the silicone support or nSi pretreatment, B) with silicone support and no nSi pretreatment, C) without silicone support and nSi pretreatment, and D) with both silicone support and nSi pretreatment. Three distinct isoforms of OPN were detected (72 kDa, 40 kDa, and 32 kDa), which were consistently upregulated in the Coll-1% nSi hydrogels. E-H) Corresponding densiometric analysis of the bands. Statistical analysis was performed by one-way ANOVA within each Osp isoform, followed by a Tukey's multiple comparison. Error bars depict standard deviation (n=3), and asterisks signify a significant difference ($p<0.05$).

3.3.7. Metabolically-Labelled ECM and Secreted Factors

To characterize nSi interaction with hMSC-secreted proteins in 3D culture, we utilized fluorescent non-canonical amino acid tagging (FUNCAT) technique previously described[127,128]. Briefly, azidohomoalanine (AHA), an azide-containing non-canonical amino acid analogue of methionine, can be incorporated into translated proteins. In turn, these can then be visualized using a fluorophore-conjugated dibenzocyclooctyne (DBCO) through strain-promoted, copper-free click-reaction. To avoid confounding effects of cell-mediated gel compactions, all hydrogels were cultured with a silicone support. After 8 days of culture in AHA-supplemented OBM, distinct spatiotemporal trends between Coll, Coll-0.1% nSi, and Coll-1% nSi hydrogels were observed (**Figure 3.8**). While hMSCs and their nuclei were clearly visible in Coll hydrogels after 4 of culture, numerous extracellular vesicles surrounding cell bodies were detected after an additional 4 days of culture (**Figure 3.8A**). In Coll-0.1% nSi gels, the addition of nSi resulted in reduced nuclear staining due to propidium iodide being sequestered by the nSi. In addition, extracellular vesicles were detected in Coll-0.1% nSi nanocomposites after 8 days of culture, albeit not as numerous as in the case of the Coll hydrogels (**Figure 3.8B**). Further increase in nSi percentage resulted in a total loss of visible extracellular vesicles in the Coll-1% nSi nanocomposites. Instead, matrix-like structures surrounding cell bodies were detected as early as 4 days of culture (**Figure 3.8C**). Furthermore, unlike in the case of Coll-0.1% nSi gels, the nSi in the Coll-1% nSi nanocomposites showed a preference for the DBCO-fluorophore instead of the propidium iodide. These results suggest that nSi in Coll-1% nSi nanocomposite are

interacting with secreted vesicles and sequestering their protein cargo, as well altering ECM deposition trends.

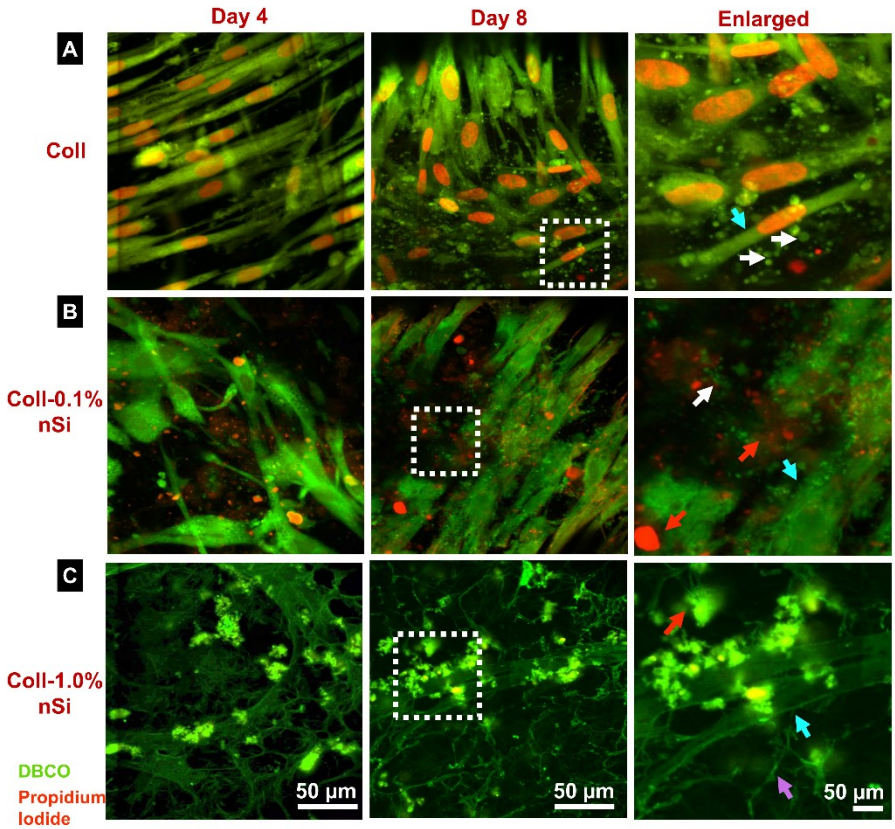

Figure 3.8: Visualization of metabolically-labeled intra- and extracellular proteins after 4 (left column) and 8 (middle and right column) days of 3D culture using fluorophore-conjugated DBCO (DBBCO-488) propidium iodide. Representative images of proteins and hMSCs encapsulated in A) Coll hydrogels, B) Coll-0.1% nSi, and C) Coll-1%nSi nanocomposites. White arrows indicate visible extracellular vesicles, red arrows indicate location of nSi, teal arrows indicate cell body, and purple arrow points to secreted ECM.

To assess whether DBCO-fluorophore propensity to nSi was indirect by means of AHA-containing proteins present on the surface of nSi, we cultured and stained acellular Coll-1% nSi nanocomposite hydrogels for 8 days in AHA-supplemented OBM (**Figure**

3.9A). Staining for metabolically labeled proteins showed an increase in the intensity of nSi-bound stain with increasing culture time (**Figure 3.9A**). Evaluating the fluorescent intensities (raw integrated density) of the acellular and hMSCs-laden Coll-1% nSi gels confirmed that although there was an inherent degree in which nSi can bind to either AHA or DBCO, the significant increase in intensity surrounding nSi after 8 days of culture is likely due to AHA-containing proteins bound to the surface of nSi (**Figure 3.9B**). We then assessed the spatial relation of newly deposited ECM with the established collagen network in Coll-1% nSi nanocomposites (**Figure 3.9C**). A high degree of colocalization and similar morphological features—thin and sparse—between metabolically-labeled proteins and the established collagen network were observed after 4 days of culture (**Figure 3.9C**). After 8 days of culture, metabolically-labeled ECM contained dense, woven structures linked by a sparsely, thin network similar to that of day 4. Furthermore, the metabolically-labeled dense woven structures were localized to regions with visibly tighter fibrillar mesh in the collagen network (**Figure 3.9C**).

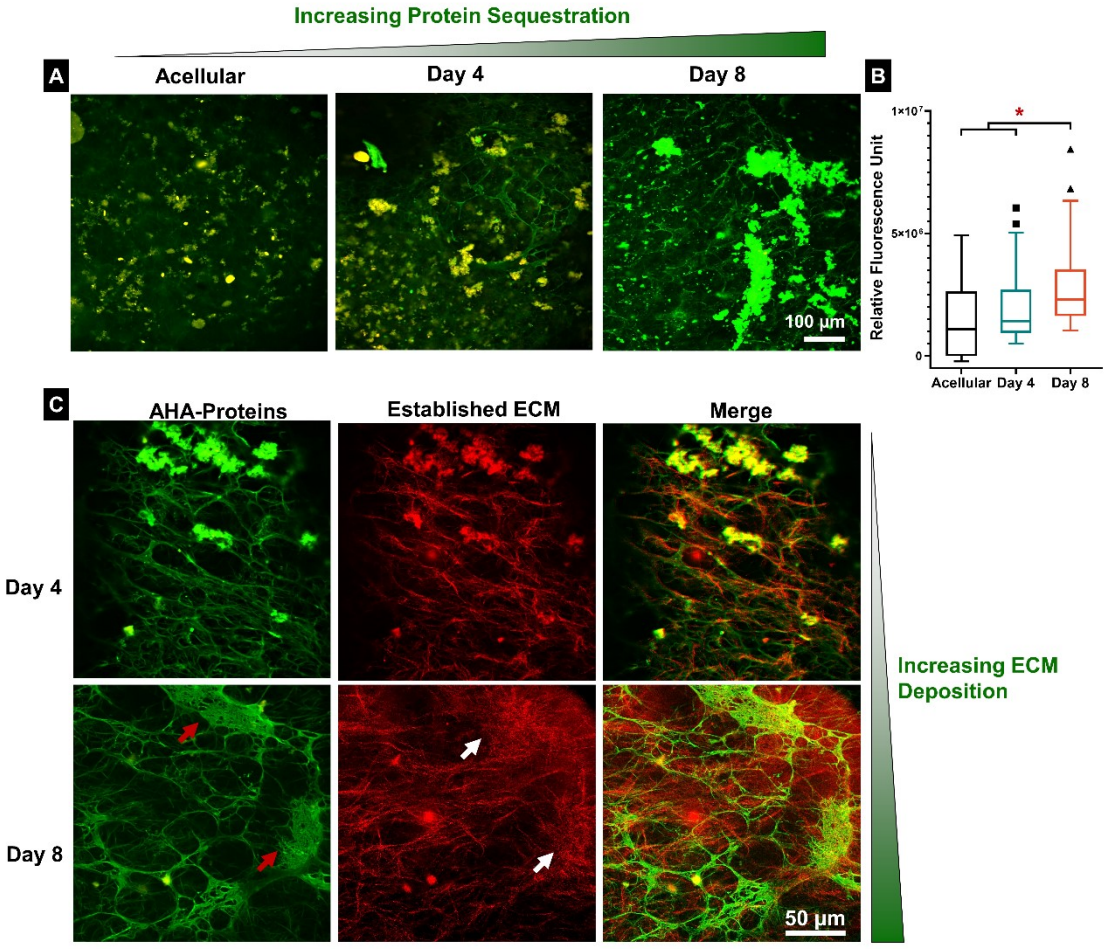

Figure 3.9: A) Representative images of acellular and hMSCs-laden Coll-1% nSi nanocomposites indicate an increase in metabolically-labelled proteins sequestered by nSi with increasing culture time. B) Quantification of fluorescence intensities of metabolically-labeled proteins on nSi confirmed significant increase in protein-nSi tethering with culture time (Kruskal-Wallis non parametric test, followed by Dunn's multiple comparison test, * $p<0.05$). C) Metabolic labelling of secreted proteins after 4 (top row) and 8 (bottom) days of 3D culture in Coll-1% nSi nanocomposites. Red arrows indicate woven structure of metabolically-labeled ECM, while white arrows indicate regions with dense fibrillar mesh in collagen network.

3.4. Discussion

Inorganic nanoparticles have been used to augment the physical and bioactive properties of polymeric hydrogels for bone repair. nSi have been particularly attractive as they readily reinforce hydrogels and possess inherent osteoinductive properties[57,58,111]. However, the mechanism by which nSi impart their osteoinductive influence in 2D culture has been elusive, and is less understood in the 3D environment of hydrogels. The data presented here showed that while matrix stiffening and nSi internalization influence the osteogenic differentiation of hMSCs in 3D culture, a strong interaction between nSi and secreted factors could play a major regulatory role by altering the biochemical landscape.

OPG, known for its role in inhibiting osteoclastic differentiation and activity by acting as a decoy receptor for receptor activator nuclear factor κ-B (RANK) ligand,[129–131] is an early indicator of osteogenic differentiation. Here, nSi treatment resulted in a significant increase in secreted OPG levels by hMSCs on days 4 and 8 (*cf.* **Figure 3.2B**). Further support of nSi osteoinductive properties in monolayers were observed in ALP expression and mineralization. The ALP enzyme plays a crucial role in generating the phosphates that are to be incorporated into the inorganic phase of bone, and is thus probed in early to mid-stages of osteogenic differentiation. ALP was observed to be significantly upregulated with a single 100 μg/mL treatment of nSi **(***cf.* **Figure 3.2E).** Microscopy imaging of ALP-stained monolayers confirmed these results, as dark and dense nodules were detected in the nSi-treated samples (*cf.* **Figure 3.2D**). Similar features were detected in the ARS-staining of mineralized monolayers, where large mineralized nodules were more frequent and darker than that of the control (*cf.* **Figure 3.2F**). In addition, recovery

of the ARS stain was significantly higher in both the 50 and 100 μg/mL nSi-treated samples when compared to the control (*cf.* **Figure 3.2G**). The similarity of the nodules in both ALP and ARS-stained monolayers is consistent with the role ALP plays in mineralization. These results are consistent with previously reported osteoinductive capabilities of nSi. Given that a single 100 μg/mL nSi treatment enhanced osteogenic differentiation, hMSCs were treated with an identical dose of nSi prior to encapsulation (nSi pretreatment).

While the mechanism by which nSi impart their influence in 2D culture is not entirely understood, internalization into cellular bodies has been proposed[57,58]. Investigation into the pathways by which nanoparticles are internalized by cells has shown that nanoparticles size, geometry, surface charge, and the presence of a protein corona regulate the rate and mode of uptake into cells[132–135]. Generally, particles under 200 nm in diameter are endocytosed by the clathrin-mediated pathway[134,135]. Indeed, it has been previously shown that nSi can be internalized by hMSCs through clathrin-mediated endocytosis, which results in nSi translocation to lysosomes (pH~5.5) where it subsequently degrades[58]. Studies into the stability of nSi over a range of pH values has shown that nSi degrade into its constituents at a pH below 9[136], and has been hypothesized that the dissolution of nSi into its mineral constituents within cellular bodies imparts the osteoinductive effects. Silicon, the most prevalent inorganic ion in nSi (~21%), has been shown to upregulate gene expression of bone markers and enhance biomineralization mediated through cWnt-signaling[137,138]. Acting through the same pathway, lithium treatment elevates cytosolic-levels of β-catenin by preventing its phosphorylation and

subsequent degradation through inhibition of glycogen synthesase kinase-3 (GSK3)[139–141]. Magnesium, the second most prolific ion in nSi (~15%), has been shown to regulate cellular proliferation and protein synthesis[142]. Specifically in hMSCs, magnesium upregulates the expression of both ECM and angiogenic proteins[143]. Whereas silicon and lithium exert their influence through the canonical Wnt/β-catenin pathway, magnesium promotes osteogenesis through Notch signaling pathway[144]. However, inclusion of the nSi into the Coll hydrogels resulted in the formations of clusters too large for clathrin-mediated endocytosis, suggesting nSi facilitate osteogenesis in 3D microenvironments by other means.

Evaluation of the microstructure of the collagen nanocomposite showed nSi clustered together to form aggregates interspersed through the network (*cf.* **Figure 3.3B**). The ways in which nSi arrange and distribute themselves in aqueous biological environments has been found to be heavily dictated by pH, presence of ions/proteins, and nSi concentration[108–110]. The discotic surface charge distribution that has made nSi a popular additive to modify the rheological properties of hydrogels also results in flocculation, or aggregation of the nanoparticles, in the presence of ions. While steps were taken (e.g. ultrasonication) to encourage a homogenous distribution of nSi in the collagen hydrogels, the use of 5x DMEM and the reconstitution buffer as the carriers of nSi in the precursor solution promotes the formation of aggregates. The choice to resuspend nSi in these solutions rather than in acetic acid was driven by fact that nSi dissociates into ion products at an accelerated rate at lower pH values. Although there are endocytic pathways that can internalize particles above 200 nm, e.g. pinocytosis and phagocytosis[134,135] , the

presence of nSi aggregates 8 days into culture (*cf.* **Figure 3.4C-D**) suggests that nSi internalization is not the dominant means by which nSi impart their osteoinductive influence.

A hallmark of nanocomposites is the tunability and improvement of mechanical properties[29,112,145,146], which readily influence stem cell fate[114–116]. Indeed, a significant increase the storage modulus was observed in Coll-1% nSi nanocomposites, while no difference was detected in Coll-0.1% nSi nanocomposites relative to Coll hydrogels (*cf.* **Figure 3.3**). Interestingly**,** despite a five-fold increase in G', the Coll-1% nSi nanocomposites experienced a significant decrease in the yield strain, and was thus more brittle than Coll and Coll-0.1% nSi hydrogels (*cf.* **Figure 3.3D**). Similar findings have been found in both self-assembled nSi hydrogels and in nSi-gelatin hydrogels[108,109], and has been proposed that the bridging between ions/proteins with nSi accounts for the increase in network stiffness, while the decrease in degrees of freedom of large nSi aggregates results in a more brittle network. The improved bulk mechanical properties of Coll-1% nSil also manifest in their ability to resist hMSCs-mediated gel compaction (*cf.* **Figure 3.4B**). Although collagen hydrogels readily promote cellular adhesion and viability, its bulk compaction from encapsulated cells is well documented and is a definitive example of cellular forces acting on their environment[115,147,148]. Given that the addition of 0.1% nSi did not cause a quantifiable alteration in the bulk rheological properties of the Coll-0.1% nSi nanocomposites, it was not surprising for Coll and Coll-0.1% nSi hydrogels to experience similar rates of cell-mediated gel compaction (*cf.* **Figure 3.4A-B**). Visualized cellular stress-fibers confirmed cell-ECM contractility. Actin staining

of hMSCs cultured in compacted hydrogels showed irregular, crimped stress fibers. In contrast, the stress fibers of hMSCs in Coll-1% nSi nanocomposites—which experienced minimal gel compaction—were elongated and aligned. The use of the silicone mold allowed for similar morphology in Coll hydrogels and Coll-0.1% nSi nanocomposites (*cf.* **Figure 3.4**). The aligned stress fibers in Coll-1% nSi suggests that hMSCs experienced a stiffer network, which could be recapitulated in Coll and Coll 0.1% nSi hydrogels by mechanically anchoring the hydrogels to the silicone mold. Matrix stiffness of 3D environment has been show to affect hMSCs commitment (osteogenesis peaking around 11–30 kPa) by influencing the ability of hMSCs to recruit and cluster adhesion ligands[114] via actin-myosin contractile forces.

We investigated the influence of nSi on the osteogenic differentiation of hMSCs in 3D culture. While the silicone support generally resulted in an increase in both ALP activity and mineralization (*cf.* **Figure 3.5**), only Coll hydrogels experienced a significant increase in ALP activity and mineralization. This would suggest that the bulk gel compaction permitted by a weaker collagen network impeded osteogenic differentiation, in agreement with previous findings[114] where it was found that rigidity of three-dimensional microenvironments influences the commitment of mesenchymal stem-cell populations changes, with osteogenesis preferentially occurring at 11–30 kPa. Thus, it was not surprising that the silicone support had little effect on ALP activity and mineralization on Coll-1% nSil, which experienced the least amount of bulk gel compaction. Pretreatment with nSi prior to hMSCs encapsulation proved to have a considerable impact on ALP activity (*cf.* **Figure 3.5B**), significantly upregulating ALP activity in all three

formulations. However, nSi pretreatment did not greatly impact calcium content, suggesting the osteoinductive influence of nSi pretreatment is limited to early window of time. In contrast, the percentage of nSi within the gels seem to have a more crucial influence. For example, Coll-1% nSi nanocomposites expressed significantly higher levels of mineralization compared to Coll hydrogels even when the Coll hydrogels was pretreated with nSi and supported by the silicone mold. This suggests that a unique microenvironment exists within the Coll-1% nSi nanocomposites that could not be entirely replicated by stiffening the collagen network with the silicone support or by the direct effects of nSi on the cells. In both endochondral and intramembranous ossification, secreted ECM and matrix vesicles act as nucleation sites for calcium phosphates[119,149]. Matrix vesicles are extracellular vesicles containing proteins that facilitate the growth of HA crystals as well as the attachment of HA to ECM. It is possible that nSi present in the extracellular space could function as nucleation sites, explaining the higher mineralization levels observed in the Coll-1% nSi nanocomposites. It should also be noted that nSi pretreatment consisted of a one-day long treatment prior to encapsulation, and does not fully replicate the continual presence of nSi in the nanocomposites. However, hMSCs in monolayer were provided an identical, single dose of nSi that yielded a significant upregulation of early to late osteogenic markers.

Given the potent capability of BMP2 in inducing endochondral bone formation, it is not surprising that BMP2 has seen clinical use for bone repair[150], despite its well-documented complications in off-label use[151–158], or that it spurred the development of novel techniques to address these limitations[159,160]. Thus, we investigated BMP2

expression at the translational level in Coll hydrogels and in Coll-nSi nanocomposites. BMP2 is initially synthesized as an inactive, 44 kDa long pre-proprotein[122,123]. Upon the removal of the signal peptide and cleaving of the prodomain by proprotein convertase, a functional and mature BMP2 (13 kDa monomer, homodimer 26 kDa) is secreted[122,161,162]. Two distinct sizes of BMP2 were observed in the resolved hMSCs lysates after 8 days of monolayer culture (*cf.* **Figure 3.2C**). Although all three conditions expressed the pre-proprotein (44 kDa), only hMSCs treated with 100 µg/mL expressed the 33kDa variant. Noticeably absent is the 13 kDa, secreted isoform of BMP2, which was likely present in the culture media of the hMSCs treated with 100 µg/mL of nSi. Nevertheless, the presence of the 33 kDa variant, which likely belongs to the cleaved region of the BMP2 proprotein, suggests that mature BMP2 had been secreted by hMSCs treated with 100 µg/mL of nSi. In 3D culture, there was a drastic difference in the expression of BMP2 between Coll-1% nSi nanocomposites and the other two hydrogel formulations. While the 44 kDa pre-proprotein was intermittently expressed in Coll hydrogels and Coll-0.1% nSi nanocomposites in the three of the four culture conditions, Coll-1% nSi nanocomposites consistently expressed significantly higher levels of the 44 kDa BMP2 isoform (*cf.* **Figure 3.6A-D**). Of particular importance, however, is the expression of the secreted 13 kDa BMP2 isoform, which was expressed in significantly higher quantities in Coll-1% nSil compared to Coll hydrogels and Coll-0.1% nSi nanocomposites. This trend was consistent for all culture conditions (*cf.* **Figure 3.6 A-D**). Interestingly, despite the synergistic effect of nSi pretreatment and silicone support had on the ALP activity and mineralization of Coll hydrogels and Coll-0.1% nSi nanocomposites, the same culture condition was not

able to stimulate the Coll hydrogels and Coll-0.1% nSi nanocomposites to express BMP2 near the levels observed in the Coll-1% nSi nanocomposites. BMP2 expression results further suggest that the microenvironment of Coll-1% nSi nanocomposites is not entirely explained by the stiffening matrix or nSi internalization.

The mode of BMP2-signaling has been hypothesized to be dominated by autocrine signaling in 3D culture due to an increase in BMP2 concentration in the pericellular space resulting from a decrease in the diffusion of BMP2. This constrainment of BMP2 is due in part to ECM sequestering BMP2[163]. For example, heavily sulfated glycosaminoglycan (GAG) can bind to BMP2 through electrostatic interactions[163,164]. In a similar principle, recent work has leveraged the negatively charged surface of nSi as a vehicle for prolonged delivery of rhBMP2[160]. It is therefore possible that incorporated nSi in Coll-1% nSi are sequestering and accumulating secreted BMP2 in the pericellular space, resulting in the drastic difference observed in the expression of the 13 kDa BMP2 isoforms. This would suggest nSi could function as a protein reservoir in 3D culture, further encouraging autocrine signaling over paracrine signaling. However, it should be mentioned that BMP2 and its receptor are internalized via clathrin or caveolin-mediated endocytosis in the initial stages of BMP signaling[155], and there has been an ongoing debate on whether internalization of BMP2 is required to achieve the full effect[155,157]. Recent in-vitro work on matrix-bound BMP2 suggests BMP signaling and the osteoinductive effects can occur even in the absence of BMP2 internalization[155,165]. In the case of nSi-bound BMP2 in collagen hydrogels, we hypothesize that both passive nSi degradation (pH of 7.4<9.0) and ECM remodeling would regulate BMP2 availability. Further investigation into nSi

binding to proteins secreted by hMSCs in 3D culture was accomplished through FUNCAT. By monitoring metabolically-labeled protein, we discovered a decrease in secreted vesicles in nSi-containing hydrogels (*cf.* **Figure 3.8A-C**), and that metabolically-labeled proteins were accumulating on nSi, which increased with the duration of culture (*cf.* **Figure 3.9A-B**). These results suggest that nSi in the extracellular environment are capable of hijacking hMSCs secretome and altering trophic activity.

As BMP2 signaling has been shown to regulate OPN transcription by activating a promoter of OPN[166], OPN protein expression in the nanocomposites was monitored to investigate whether commandeering of secreted proteins by nSi negatively impacted BMP2 activity. Three distinct isoforms of OPN were detected in the nanocomposites, 72 kDa, 40 kDa, and 32 kDa. Mimicking the trend observed for BMP2 expression, Coll-1% nSil were the only hydrogel formulation that reliably expressed OPN in the four culture conditions, suggesting that BMP2 signaling could have been occurring despite being matrix/nSi bound (*cf.* **Figure 3.7A-D**). More important, however, was the fact that the three OPN isoforms matched that of full-length OPN and its fragments after being proteolytically cleaved by matrix metalloproteinase (MMP)-3 and MMP-7[126]. The biological significance of discovering evidence of MMP3 and MMP7 activity lies in their high expression in both immature and hypertrophic chondrocytes and their role in matrix remodeling during endochondral bone formation[126,167–169]. While attempts have been made to replicate endochondral ossification *in vitro* through co-cultures of MSCs, chondrocytes, and or osteoblasts[170–172], our results suggest this can be achieved with hMSCs cultured in a Coll-nSi nanocomposite with standard osteogenic supplements.

Furthermore, MMPs are known to be trafficked by extracellular vesicles[173], and would suggest that the presence of the nSi did not negatively impact their proteolytic activity. Visualization of secreted ECM by FUNCAT collaborated these findings (*cf.* **Figure 3.9C**). Newly synthesized ECM with varying structural features were detected and were localized in regions of collagen hydrogels with similar microarchitecture. Thus, indicating encapsulated cells were actively remodeling their environment.

3.5. Conclusion

The high surface-to-volume ratio and discotic charge distribution of synthetic silicate nanoplatelets (nSi) has motivated a prolific body of work in designing nanocomposites for regenerative applications. In addition to their ability to modify the rheological properties of polymer-based hydrogels, nSi are viewed as an attractive choice for bone repair as they are an additional osteoinductive source. Conventional knowledge on nSi-based nanocomposites touts their improved mechanical properties and their internalization into cell bodies and subsequent ionic dissolution as the driving force behind the enhanced osteo-regenerative capabilities observed in nSi nanocomposites. In our work, we decouple the network-fortifying properties of nSi and the effects of nSi internalization/ionic dissolution. By allowing nSi to aggregate in a collagen-network, we fabricated a mechanically-stiffer network and a microenvironment in which nSi were too large to be internalized. Anchoring standard collagen gels to silicone support replicated a stiffer matrix without nSi, while nSi pretreatment was used to replicate nSi internalization without altering hydrogel properties. We showed that neither of those efforts truly replicated the improved osteogenic response of Coll-nSi nanocomposites. Further

examination showed that nSi aggregates sequester and accumulate the cargo of extracellular vesicles. Thus, the improved osteogenic response in Coll-nSi nanocomposite could be due in part to nSi hijacking trophic activity.

4. METABOLICALLY LABELED IP-HMSC-DERIVED ANABOLIC BONE ECM FOR BIO-ORTHOGONAL CLICK REACTIONS

4.1. Introduction

ECM proteins and their binding domains have been used to enhance the bone repair capabilities of scaffolds[46,48,49,70,174]. Methods to functionalize scaffold surface with ECM proteins include physisorption from simple protein stock solutions[174], direct cell-culture deposition[48–51,70], and covalent tethering[116,175]. Functionalizing synthetic scaffolds/hydrogels with singular peptide sequences, that exert similar effects to their full-length protein counterpart have also been explored[176,177]. Peptide instability remains an issue[177], however, and the use of single peptide sequences fails to mimic the complex array of signals stemming from an osteogenic extracellular niche. While direct deposition of ECM onto established scaffolds allows for the fabrication of scaffolds with desired microstructures and composition coated with a complex array of ECM[48,50,51], the decellularization process can have a deleterious effect on scaffold mechanical properties[60]. Covalent tethering of ECM to established scaffolds can provide greater stability than adsorption, but the tethering chemistry can potentially alter the bioactivity of the proteins of interest. A technique capable of covalently tethering a complex array of proteins to established scaffolds without compromising their bioactivity would be a powerful tool in designing engineered scaffolds for bone repair.

We have utilized an hMSC-derived ECM that has been shown to enhance hMSC retention and accelerate bone repair in rodent calvarial, femoral, and spinal defect models[45–47]. Briefly, hMSCs treated with GW9662, a PPAR-γ inhibitor, secrete a

collagenous ECM cocktail that resembles the composition of anabolic bone, including high levels of Collagen VI (Coll VI) and Collagen XII (Coll XII)[45]. A significant drawback to using hMSCs to produce ECM and other complex biological products is their limited proliferation potential and variability in cell behavior between donors. To address these limitations, hMSCs have been generated from human induced pluripotent stem cells (iP-hMSCs)[69]. Unlike donor-derived hMSCs, undifferentiated iPSCs divide without senescence until they are differentiated into iP-hMSCs, providing a theoretically limitless supply of reproducible biomaterial for the production of the anabolic bone matrix described in this work. This provides a potential strategy to produce large quantities of ECM generated from a genetically identical source of iP-hMSCs in a reproducible manner. While this ECM can mimic the osteoregenerative microenvironment, a lack of structural form limits its practicality for bone repair. Direct cellular deposition of the anabolic bone ECM has been previously performed onto gelatin foam[46,60] as well as 3D-printed scaffolds[60], but these suffer from the aforementioned limitations.

Protein functionalization strategies have historically targeted lysine and cysteine residues due to their relative abundance and highly nucleophilic side chains[178]. Although these techniques are facile to implement, the random functionalization can yield a heterogeneous mixture of proteins, with potentially reduced bioactivity[159]. Recently, strategies that hijack native protein synthesis processes have been used to functionalize proteins in a relatively non-invasive manner. Specifically, non-canonical amino acids recognized by endogenous tRNA/synthetase pairs can be incorporated into translated proteins in the place of their canonical counterparts. Although many non-canonical amino

acids have been developed to be metabolically incorporated, azide-containing methionine analog L-azidohomoalanine (AHA) has been widely utilized[120,121,179–182]. Once present, azide moieties have been typically leveraged to participate in a either copper-catalyzed azide-alkyne cycloaddition or strain promoted azide-alkyne cycloaddition (SPAAC) for protein visualization, i.e. fluorescent non-canonical amino-acid tagging (FUNCAT)[120,121,182]. Here, we report an approach for covalently tethering iP-hMSC-derived ECM onto established scaffolds via biorthogonal SPAAC chemistry. Azide functionality was metabolically incorporated into iP-MSCs-derived ECM, while gelatin-methacryloyl (GelMA) was functionalized with dibenzocyclooctyne (DBCO), which can participate in SPAAC chemistry.

4.2. Methods

4.2.1. Synthesis of DBCO-Modified GelMA

Gelatin methacryloyl (GelMA) with 80% methacrylation was synthesized using a previously reported method[183]. The addition of the DBCO moiety was performed either on GelMA polymer chains in solution before UV-crosslinking (DBCO-GelMA^{BC}) or after UV-crosslinking (DBCO-GelMA^{AC}). Both methods made use of EDC (1-ethyl-3-[3-dimethylaminopropyl] carbodiimide hydrochloride) and NHS (N- hydroxysuccinimide) chemistry. For functionalizing uncrosslinked polymeric chains, 60 mg of GelMA were dissolved in 6 mL of reaction buffer consisting of 0.1M MES and 0.5M NaCl (pH 6.0) for 30 minutes at 37°C. Once dissolved, approximately 23 mg of EDC (20 mM) and 34.5 mg NHS (50 mM) were added to the GelMA solution. The solution was incubated at 37°C for 20 minutes with gentle rocking. To quench the reaction, 20 µL of β-mercaptoethanol was

added to the mixture. A Zeba™ Spin Desalting Column (Thermo Fisher Scientific) equilibrated to PBS was used to remove non-protein reagents following the manufacturer instructions. A 100 mM stock solution of DBCO-Sulfo-PEG-Amine (Click Chemistry Tools) in sterile-filtered DI water was prepared prior to use. Approximately 30 µL of 100 mM DBCO-Sulfo-PEG-Amine solution was added to the activated GelMA solution, resulting in a 5-molar excess ratio between DBCO to GelMA. The reaction was allowed to proceed for 2 hours at 37°C. After the reaction, the solution was dialyzed for 24 hours against DI water at 37°C using dialysis cassettes (Thermo Fisher Scientific). The solution was stored overnight at -20°C, then lyophilized for 48 hours. The resulting DBCO functionalized GelMA (DBCO-GelMA^{BC}) was stored at -20°C until needed. Hydrogels were prepared with the lyophilized DBCO-GelMA^{BC} by dissolving 7.5% (w/v) DBCO-GelMA^{BC} and 2 mM lithium acylphosphinate photoinitiator (LAP) in PBS and dispensing into silicone molds (diameter 1 cm; 1.5 mm thick). The precursor solution was crosslinked for 2 minutes seconds under UV light using a High-Performance UV Transilluminator Plate (UVP).

For surface functionalization, standard GelMA hydrogels were prepared prior to EDC/NHS rection. GelMA precursor solution—7.5% (w/v) GelMA and 2 mM LAP dissolved in PBS—was dispensed in the silicone molds and UV crosslinked as described above. The hydrogels were collected and washed three times with the reaction buffer, incubating for 20 minutes at 37°C between washes. The hydrogels were then incubated in 2 mL of reaction buffer with 20 mM of EDC and 50 mM of NHS for 20 minutes at 37°C with gentle rocking. The hydrogels were then washed three times with excess PBS,

incubating for 10 minutes at 37°C with agitation in the final wash. The hydrogels were incubated in 1 mL of PBS and 5 µL of 100 mM DBCO-Sulfo-PEG-Amine (5:1 molar ratio) for overnight at 37°C with gentle rocking. The resulting DBCO-GelMA^{AC} hydrogels were then washed three times in PBS and were immediately used for downstream applications.

4.2.2. Fluorescent Labeling of DBCO-GelMA Hydrogels and Swelling Test

To evaluate the optimal procedure in functionalizing DBCO moiety onto GelMA hydrogels, the degree of DBCO functionality on the DBCO-GelMA^{BC} or DBCO-GelMA^{AC} was evaluated using an azide-conjugated fluorescent dye. Briefly, hydrogels were incubated in 1 mL of 30 µM of AFDye 488 Azide, (Click Chemistry Tools) in PBS for 45 minutes at 37°C. The hydrogels were washed three times with PBS and imaged on the Bio-Rad EZ Gel Reader. The hydrogels were stored overnight at 4°C in PBS and imaged again the following day. The process was repeated up to 8 days. The fluorescent intensity of the hydrogels was quantified on ImageJ (NIH Image). The equilibrium swelling ratio of DBCO-GelMA^{BC}, DBCO-GelMA^{AC}, GelMA, and GelMA hydrogels that underwent the EDC/NHS chemistry but were no provided the DBCO moiety were evaluated using the following equation:

$$\text{Swelling Ratio} = \frac{\mathrm{W_{wet}} - \mathrm{W_{dry}}}{W_{dry}}$$

Here, W_{wet} and W_{dry} represent the weight of the hydrogels equilibrated in DI water and the weight of the hydrogels after drying. The hydrogels were incubated with DI water for 1 hours at 37ºC. After recording the wet weights, scaffolds were dried in a desiccator for 48 hours, and weighed again.

4.2.3. iP-hMSC Culture and Production of Anabolic Bone ECM

Human induced pluripotent stem cells (iP-hMSCs) were generated as previously described[69], and were expanded in complete culture media (CCM) consisting of alpha minimal essential medium (α-MEM; Invitrogen), 10% (v/v) FBS (Atlanta Biologicals), 2 mM L- glutamine (Invitrogen;), and 100 U/ml penicillin plus 100 µg/ml streptomycin (HyClone™) at a seeding density of 500 cells/cm^2. To generate anabolic bone ECM for SPAAC applications (**Figure 4.1**A), iP-hMSCs were cultured in 150 mm petri dishes. Culture media was changed every 2-3 days until a confluency of 70-80% was achieved. Thereafter, iP-hMSCs were cultured in osteogenic basal media (OBM)—CCM with 20% (v/v) FBS instead of 10% (v/v), 5 mM β-glycerophosphate, and 50 µg/mL ascorbic acid—supplemented with either 10 µM of GW9662 or an equal volume of its vehicle, DMSO. In addition, L-azidohomoalanine (AHA) (Click Chemistry Tools), a non-canonical analogue of methionine, was metabolically incorporated in the ECM by adding 300 µM of AHA, or an equal volume of deionized water vehicle. The iP-hMSCs were cultured for a total of 10 days, with media changes occurring every 2 days. On day 10, the ECM was harvested as previously described[184]. Briefly, the 150 mm dishes were washed twice with warmed PBS before being stored overnight at -20°C. The following day, frozen monolayers were washed with warmed PBS before being transferred to 15 mL conical tubes (two 150 mm^2 dishes per conical tube) using sterile cell-scrapers.

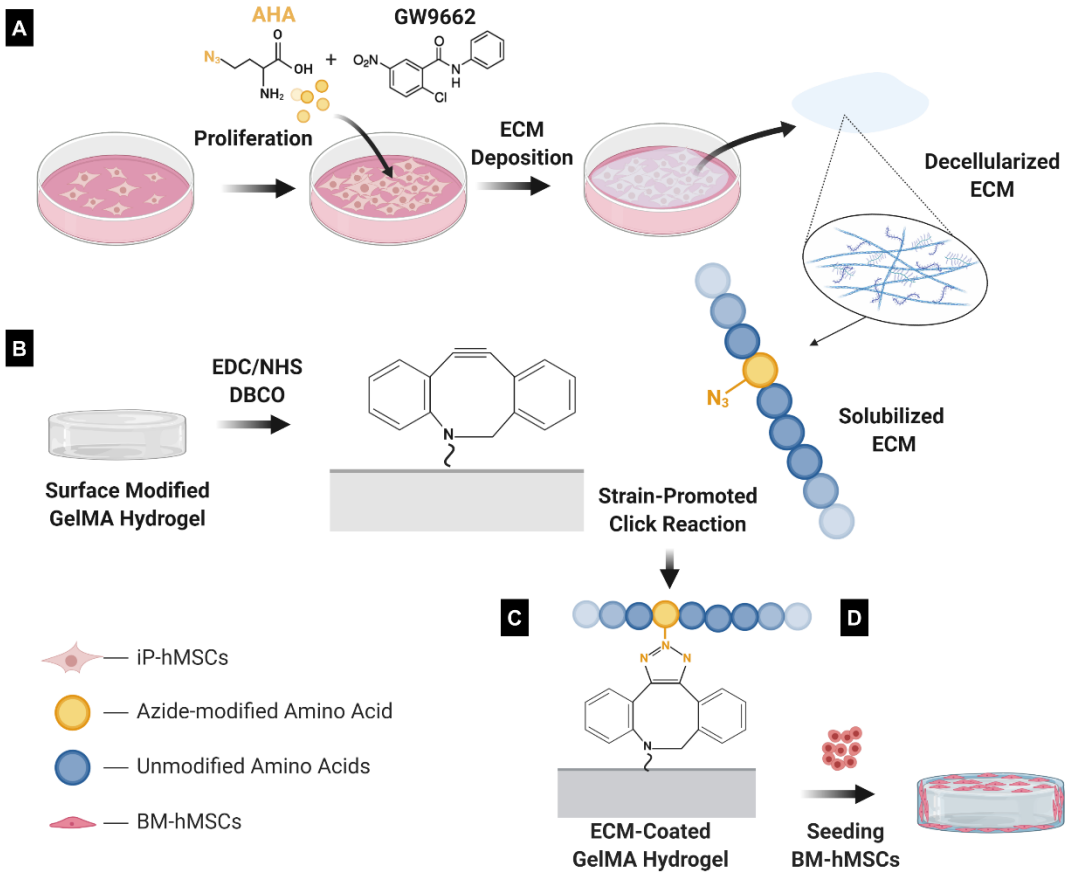

Figure 4.1: A) Schematic illustrating the development iP-hMSC derived AHA-ECM. The methionine analogue added to culture media is metabolically incorporated into the anabolic bone ECM over the course of 10 days, after which it is decellularized. B) GelMA hydrogels functionalized with the DBCO moiety (DBCO-PEG-Sulfo-Amine) through EDC/NHS chemistry. C) Anabolic bone ECM covalently tethered to DBCO-GelMA hydrogels through strain-promoted azide-alkyne cycloaddition. D) BM-hMSCs will be seeded on ECM-coated GelMA hydrogels and evaluated for in vitro osteogenic differentiation after 21 days of culture.

The collected ECMs were then pelleted by centrifugation (10 minutes at 1000g) and resuspended in 10 mL of lysis buffer consisting of 0.1% (v/v) Triton-X 100, 1 mM $MgCl_2$, 1 U/mL DNAse I (Thermo Fisher), and 10 µg/mL of RNAse (Sigma-Aldrich). The conical tubes were placed in a rocker at 37°C for 4 hours before adding 10 µg/mL

trypsin (Gibco). The lysis was allowed to proceed overnight at 37 °C with gentle rocking. The ECMs were then pelleted and washed twice with DI water, once with chloroform, and twice with DI water. The collected ECMs were washed once with acetone then resuspended in 1 mL of DI water before freezing at -20°C. The frozen ECMs were lyophilized for two days and then stored at -20°C until needed for solubilization. Briefly, dried ECMs were resuspended in sterile-filtered 0.1 M acetic Acid (5-10 mg/mL) and were kept at 4°C on a tube revolver for 48 hours. Collagen concentration in the supernatant was measured by A280 method using known collagen standards on a nanodrop 3000 (Thermo Fisher). In the end, four distinct ECMs were generated, referred to by the media in which iP-hMSCs were cultured in: DMSO, DMSO+AHA, GW, and GW+AHA.

4.2.4. Immunoblotting AHA-Modified ECM

After 10 days of culture on 6-well plates, proteins from iP-hMSCs monolayers were fractioned into intracellular and extracellular portions using a previously described protocol with modifications[141]. Briefly, monolayers were washed with warm followed by ice-cold PBS. Sequential lysing was performed with two distinct lysis buffers. Intracellular proteins were first extracted by dispensing 450 µL of ice-cold lysis buffer consisting of 50 mM Tris HCl, 150 mM NaCl, 1% Triton-X-100, 1 mM EDTA, 1 mM Sodium Pyrophosphate, and SIGMAFAST™ protease inhibitor cocktail (Sigma-Aldrich) into each well. Well plates were then incubated for 10 minutes with gentle rocking. The lysis buffer and the extracted proteins was carefully collected, making sure to avoid collecting the visible monolayer of extracellular proteins. After three washes with PBS,

the extracellular proteins left behind were then extracted using 450 µL ice-cold RIPA buffer (50 mM Tris HCl, 150 mM NaCl, 1% Triton-X-100, 1% SDS, 0.5% Sodium Deoxylcholate, 1 mM EDTA, 1 mM Sodium Pyrophosphate) supplemented with SIGMAFAST^{TM} protease inhibitors (Sigma-Aldrich) through vortexing for 30 seconds. Both protein fractions were stored in -80°C until total protein content was quantified through Pierce BCA Protein Assay kit (Thermo Fisher Scientific).

After protein quantification, 4X SDS sample buffer (150 mM Tris-HCl, 25% glycerol, 12% SDS, 0.05% bromophenol blue, and 6% β-mercaptoethanol) was added to extracted proteins at a 1:3 ratio. Approximately 20 µg of protein were resolved in hand-casted 8% SDS-PAGE gels, and transferred to a PVDF membrane (Millipore). The membrane was blocked in 5% milk in TBST buffer (20 mM Tris-base, 150 mM NaCl, 0.2% Tween 20) for one hour before being incubated overnight at 4 ºC with rabbit-anti-human Coll VI alpha-1 antibody (Novus Bio NB120-6588) diluted (1:1000) in blocking buffer. After 3 washes in TBST buffer, the membrane was incubated for 1 hour with an HRP-conjugated goat-anti-rabbit secondary antibody (Protein Tech). The membrane was developed for 5 minutes in WesternSure Chemiluminescent Substrate (LI-COR) and imaged on a C-Digit Blot Scanner (LI-COR). After imaging, the membrane was stripped using Restore Stripping Buffer (Thermo Fisher Scientific) following the manufacturer instructions. The membrane was then blocked, incubated with rabbit-anti-human Coll XII alpha-1 antibody (Novus Bio NP88062; 1:500 dilution), and imaged as previously described. Similar process was repeated with mouse-anti-human GAPDH (Protein Tech;

1:4000) antibody and its corresponding HRP-conjugated goat-anti-mouse secondary antibody (Protein Tech).

4.2.5. Immunostaining of AHA-Modified ECM

To verify AHA was metabolically incorporated in the deposited ECM, immunofluorescence against ECM proteins counterstained with DBCO-fluorescent dye was performed on iP-hMSCs monolayers. Briefly, after 10 days of cultured in OBM with 10 μM of GW9662 and either 0, 100, or 300 μM of AHA, iP-hMSC monolayers were washed once with PBS then twice with 1% bovine serum albumin (BSA) in PBS. Monolayers were then incubated with 30 μM DBCO-543 fluorescent dye (Click Chemistry Tools) in 1% BSA solution for 45 minutes at 37°C, and were then washed three times with warmed PBS. The cycloaddition between the DBCO fluorescent tag and the AHA-containing proteins was performed prior to cell fixation as it reduced intracellular staining[120]. Monolayers were fixed for 1 hour at room temperature in 4% formaldehyde in PBS, followed by three washes with PBS. Samples were then blocked with 5% goat serum (MP Biomedical) and 0.3% Triton-X (Sigma Aldrich, St. Louis, MO, USA) in PBS for 1 hour at room temperature before being incubated overnight at 4°C in the blocking buffer supplemented with either rabbit anti-human Coll VI or Coll XII (1:200, Novus Biological, Littleton, CO, USA). Monolayers were then washed with PBS and were incubated at room temperature for 2 hours in blocking buffer with fluorescein-conjugated goat anti-rabbit (1:500, Millipore, Burlington, MA, USA). Standard nuclear staining with Hoechst was then performed. Monolayers were imaged on an Axio Vert.A1 fluorescent microscope (Zeiss). The mean fluorescence intensity of DBCO-staining was quantified on ImageJ

(NIH Images) (n=4 images per condition). Statistical analysis was performed by one-way ANOVA, followed by a Tukey's multiple comparison ($p<0.05$).

4.2.6. In Gel Detection of AHA-Modified Proteins

To further confirm whether the added AHA was directly incorporated into newly made proteins and whether this non-canonical amino acid alters iP-hMSC translational activity, in-gel fluorescence was performed. Briefly, 50 µg of extracted proteins were conjugated to 10 µM of DBCO-488 fluorescent dye (Click Chemistry Tools) in 100 µL of RIPA buffer for 45 minutes at 37°C in a 1.5 mL microcentrifuge tube. Proteins were then extracted and separated from unreacted DBCO dye using a modified methanol-chloroform precipitation protocol. Briefly, 400 µL of methanol was added to each sample, followed by 100 of µL of chloroform, and then 300 µL of water. Samples were briefly vortexed between each addition. Samples were centrifuged at 4°C for 5 minutes at 12,000g. After removing the top aqueous layer without disturbing the protein interphase, 400 µL of methanol was added and vortexed. Proteins were precipitated by centrifuging at 4°C for 5 minutes at 20,000g. The supernatant was removed and an additional 400 µL of methanol was added. Samples were kept overnight at 4°C on a tube rotator, protected from light, to elute unreacted DBCO dye. The following day, the supernatant was removed and the protein pellets were washed one additional time with 400 µL of methanol. The supernatant was removed and the protein pellets were dried at room temperature. Immediately after, protein pellets were resuspended in 50 µL of warmed RIPA buffer/4X SDS sample buffer. Proteins were resolved in a hand-casted 10% SDS-PAGE gel, and imaged on a Bio-Rad EZ Gel Reader. Total protein in the gel was visualized using the Imperial™ Protein Stain

(Thermo Fisher Scientific) following the manufacturer instructions, and were imaged on the gel reader.

4.2.7. Bone Marrow Derived hMSCs Cultured on ECM-coated Tissue Culture Plates

We anticipated that bone marrow aspirate is currently the most clinically relevant source of osteoprogenitor cell source, hence we used bone marrow derived hMSCs to assess cell behavior on standard and AHA-modified iP-hMSC-derived ECM. The bone marrow derived hMSCs were acquired from the Texas A&M Health Science Center adult stem cell distribution facility in accordance with their institutionally approved protocols. The hMSCs were expanded in a similar fashion as the iP-hMSCs with slight modifications; CCM contained 20% (v/v) FBS rather than 10% (v/v). Several ECM-coated 6-well plates were prepared using a previously described protocol with slight modifications[184]. Dilutions of acid-solubilized ECM in PBS were dispensed in the wells of 6-well plates at a final concentration of 25 μg/cm^2. The well plates were then incubated overnight at 4°C. The following day, the plates were washed with PBS prior to seeding hMSCs at density of 10,000 cells/cm^2 in CCM. The hMSCs were incubated overnight before switching to OBM. The cultures were continued up to 4 days, with media changes occurring every two days.

4.2.8. Alkaline Phosphatase Kinetic and Osteoprotegerin (OPG) ELISA Assays

On days 2, 4, and 8, conditioned media was collected and stored at -80°C for downstream use in OPG ELISA (R&D Systems) following manufacturer instructions. Concurrently, the monolayers were washed twice with warmed PBS followed by ALP

buffer consisting of 100 mM Trix-HCl, 100 mM KCl, 1 mM of $MgCl_2$. Each well was then given 1 mL of ALP buffer warmed to 37°C. An equal volume of 1-Step p-nitrophenyl phosphate (PNPP) substrate (Thermo Fisher Scientific) was added to each well. Immediately, the absorbance at 405 nm was read every 30 seconds over the course of 15 minutes using an Infinite M200 Pro plate reader (Tecan). Monolayers were then washed with PBS and stored at -20°C to use downstream for cell number quantification.

4.2.9. Cell Number Quantification

The 6-well plates cultures stored at -20°C were removed and washed with warmed PBS. Samples were then lysed using a buffer consisting of PBS supplemented with 1 mM $MgCl_2$ and 0.1% Triton-X 100 (Sigma Aldrich). Samples were homogenized through vortexing for 15 seconds. Diluted aliquots of the lysed samples were pipetted to a Black Nunc 96-well fluorescent plat (Thermo Fisher Scientific). An equal volume of CyQUANT buffer consisting of 2X CyQUANT dye (CyQUANT Cell Proliferation, Invitrogen) was added to each sample. A standard from a known number of hMSCs was prepared in a similar fashion through serial dilutions. The fluorescence was read on an Infinite M200 Pro plate reader (Tecan) at 480/520 nm excitation/emission.

4.3. Results

4.3.1. Characterization of DBCO-GelMA Hydrogels

Our goal to covalently tether the iP-hMSCs derived anabolic bone ECM to an established scaffold via SPAAC chemistry necessitates the presence of azides or alkyne moieties on the anabolic bone ECM and on the established scaffold (**Figure 4.1**). Here, we investigated two approaches to functionalize the GelMA, a well-established hydrogel

platform, with DBCO, a cyclooctyne: 1) functionalization of pre-polymer monomers in solution and 2) functionalization of the polymerized GelMA. DBCO functionality on GelMA hydrogels was assessed with an azide-fluorescent tag. Photopatterned DBCO-GelMA^{BC} were easily distinguished from unaltered GelMA hydrogels, although an overnight wash in PBS is required to eliminate untethered azide-fluorophores (**Figure 4.2A**). Furthermore, the azide-fluorophore was consistently region-bound to the DBCO-GelMA^{BC} up to 8 days, hinting a stable covalent cycloaddition bone has occurred. Comparison between surface (DBCO-GelMA^{AC}) and bulk (DBCO-GelMA^{BC}) functionalization revealed both methods yield hydrogels that retain the azide-fluorescent tag to a significantly higher degree than GelMA hydrogels modified by the EDC/NHS chemistry, indicating both are chemically functionalized with the DBCO moiety (**Figure 4.2B-C**). In addition, a significantly higher fluorescence was observed in the DBCO-GelMA^{AC} hydrogels compared to DBCO-GelMA^{BC} hydrogels.

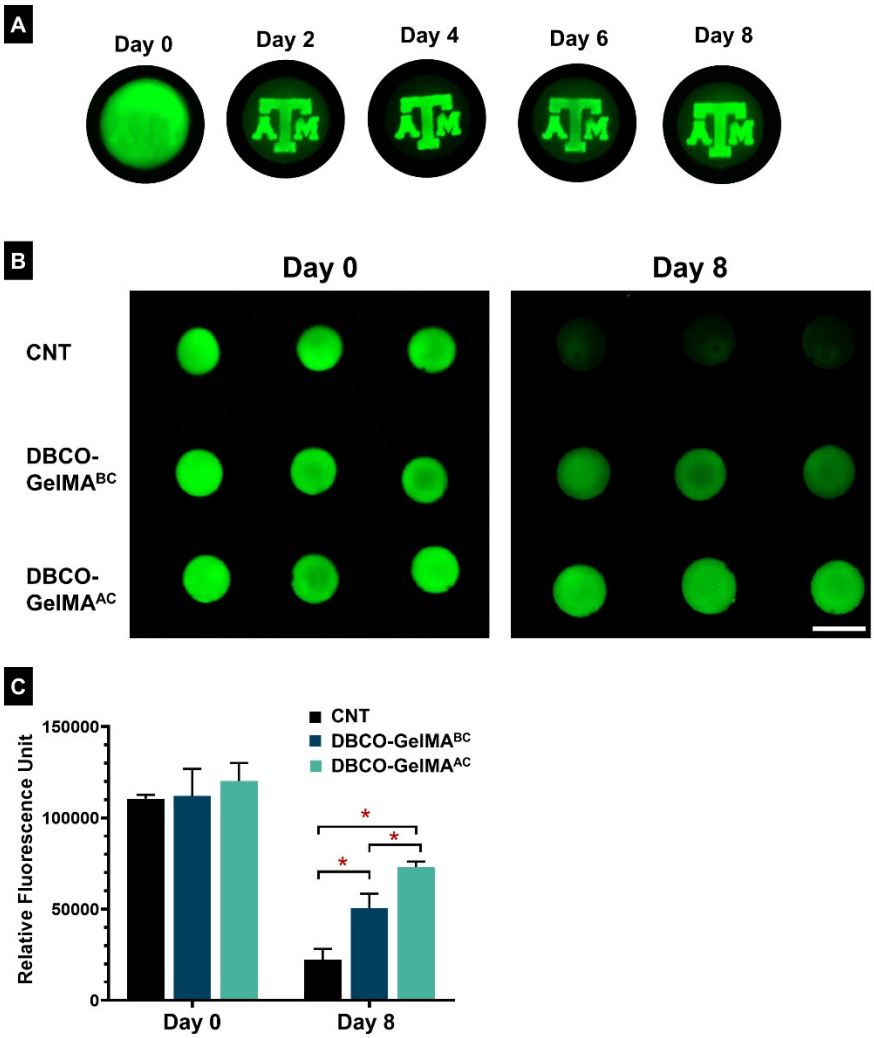

Figure 4.2: Fluorescent labeling of DBCO-GelMA hydrogels. A) Photopatterned DBCO-GelMA^{BC} hydrogel in GelMA. B) Fluorescently labeled DBCO-GelMA^{BC} and DBCO-GelMA^{AC} with an azide-488 tag. GelMA hydrogels modified by EDC/NHS chemistry used as a control (Scale bar 1 cm). C) Degree of DBCO functionality on DBCO-GelMA^{BC} and DBCO-GelMA^{AC} hydrogels approximated by their relative fluorescent intensity. GelMA hydrogels modified by EDC/NHS chemistry used as a control. Statistical analysis was performed by one-way ANOVA, followed by a Tukey's multiple comparison. Error bars depict standard deviation (n=3), and asterisks signify a significant difference ($p<0.05$).

4.3.2. Expression of Anabolic Bone ECM

Metabolic incorporation of azide-containing non-canonical amino acids into translated proteins provides a facile mean to functionalize a complex cocktail of proteins

with the azide functionality. It has been previously shown that the ECM deposited by hMSCs treated with GW9662 contains elevated levels of Coll VI and XII[46], with similar trends observed in iP-hMSCs[60]. Immunoblotting against these matrix proteins was performed on intracellular and extracellular fractions of lysed iP-hMSCs monolayers after 10 days of culture in OBM supplemented with GW9662 in the presence and absence of AHA. Although Coll VI and Coll XII expression was analyzed in both fractions, results for the extracellular fraction are more representative of the composition of purified decellularized anabolic bone ECM. Two distinct molecular weights for Coll VI were observed in both the intracellular and extracellular fractions, at approximately 150 and 100 kDa (**Figure 4.3A&C**). While similar expression levels of the 100 kDa Coll VI was observed between GW9662 treated and the DMSO controls, GW9662 treatment increased the expression of the 150 kDa Coll VI in the intracellular fraction (**Figure 4.3B**). Furthermore, AHA treatment did not affect expression of either variant of Coll VI in either GW9662-treated samples and DMSO samples (**Figure 4.3B**). Results for the expression of Coll XII (250 kDa) were more complex. GW9662 treatment increased Coll XII expression in the absence of AHA relative to the DMSO control. Upon the addition of AHA, however, Coll XII expression appeared to decrease (**Figure 4.3A**). In contrast, AHA treatment in the absence of GW9662 increased Coll XII expression in the intracellular fraction (**Figure 4.3B**).

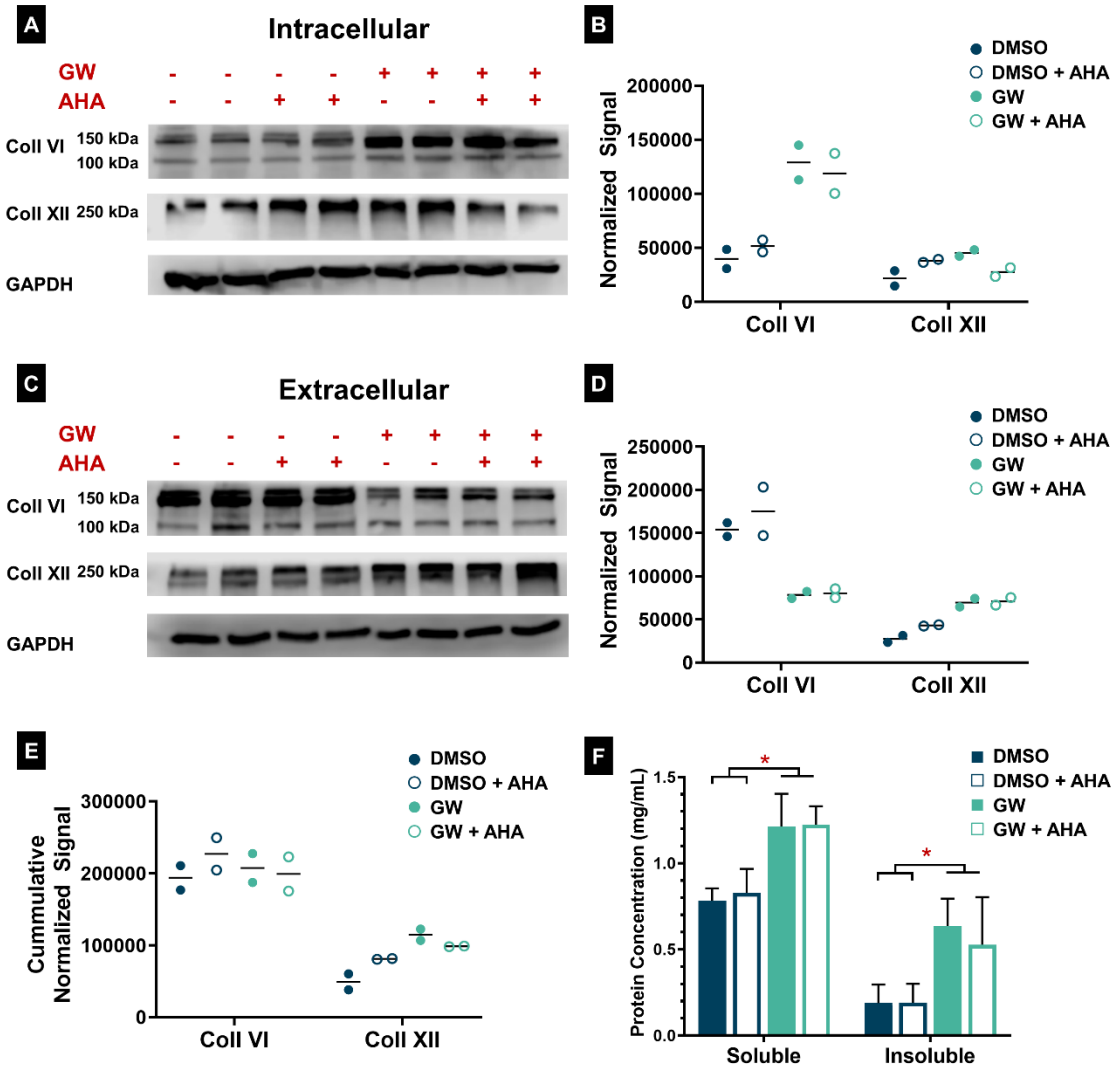

Figure 4.3: Immunoblotting against Coll VI and XII after 10 days of culture for A) intracellular and C) extracellular protein fractions. B) and D) Corresponding densiometric analysis are shown on the right. E) Cumulative band intensity for intracellular and extracellular protein fractions. F) Protein content of iP-hMSCs monolayers after 10 days of culture. Statistical analysis was performed by one-way ANOVA within insoluble and soluble fractions, followed by a Tukey's multiple comparison. Error bars depict standard deviation (n=3), and asterisks signify a significant difference ($p<0.05$).

In contrast to the Coll VI expression trends observed in the intracellular fraction, DMSO treated cultures expressed higher levels of the 150 kDa Coll VI variant relative to the GW9662 treated counterparts in the extracellular fractions (**Figure 4.3C**). In

agreement with results observed in the intracellular fraction, AHA treatment did not impact Coll VI expression in either the GW9662 treated samples and the DMSO controls in the extracellular fraction (**Figure 4.3C&D**). GW9662 treatment increased Coll XII expression relative to the DMSO controls in the extracellular fraction (**Figure 4.3C&D**). Once again, providing iP-hMSCs cultures with AHA did not impact Coll XII expression (**Figure 4.3D**). To approximate total cell and ECM expression, the normalized signal for the extracellular and intracellular fractions was consolidated (**Figure 4.3E**). Analysis of the consolidated signals indicated GW9662 increased Coll XII expression relative to the DMSO controls, while Coll VI expression was unaffected by GW9662 treatment (**Figure 4.3E**). Furthermore, AHA treatment had no impact on either Coll VI and Coll XII expression (**Figure 4.3E**). To evaluate which culture condition would provide larger volumes of decellularized ECM for downstream tethering applications, total protein content of the extracellular fractions were analyzed. Interestingly, GW9662 treatment stimulated significantly higher levels of protein in both the intracellular and extracellular fractions relative to the DMSO controls (**Figure 4.3F**).

4.3.3. Deposition of AHA Incorporated Anabolic Bone ECM

To determine whether the non-canonical amino acid was successfully incorporated into secreted proteins, cyclo-addition between the AHA-containing proteins and the fluorophore-conjugated cyclooctyne was performed on iP-hMSCs monolayers prior to cell fixation. By performing the click reaction prior to fixation, we expect that reactions with azide-labeled intracellular proteins will be avoided[120,182]. Monolayers were also immunostained against either Coll VI or Coll XII for comparison. Phase microscopy

showed highly confluent iP-hMSC monolayers contained protein aggregates that are likely nascent bone nodules (**Figure 4.4A&C**). Fluorescence microscopy of the metabolically-labeled proteins in the extracellular space showed a high degree of spatial and morphological similarities to these nodules. Furthermore, increasing the AHA concentration provided to iP-hMSC cultures resulted in significantly higher mean fluorescence (**Figure 4.4B&D**). Coll VI was highly expressed and was uniformly distributed in the monolayers. Consistent with immunoblotting results (*cf* **Figure 4.3E**), AHA treatment did not impact deposition of Coll VI. While Coll XII was also highly expressed, strong fluorescent regions matched the aggregates observed under phase microscopy and in metabolically labeled proteins. Furthermore, deposition of Coll XII was not affected by AHA treatment.

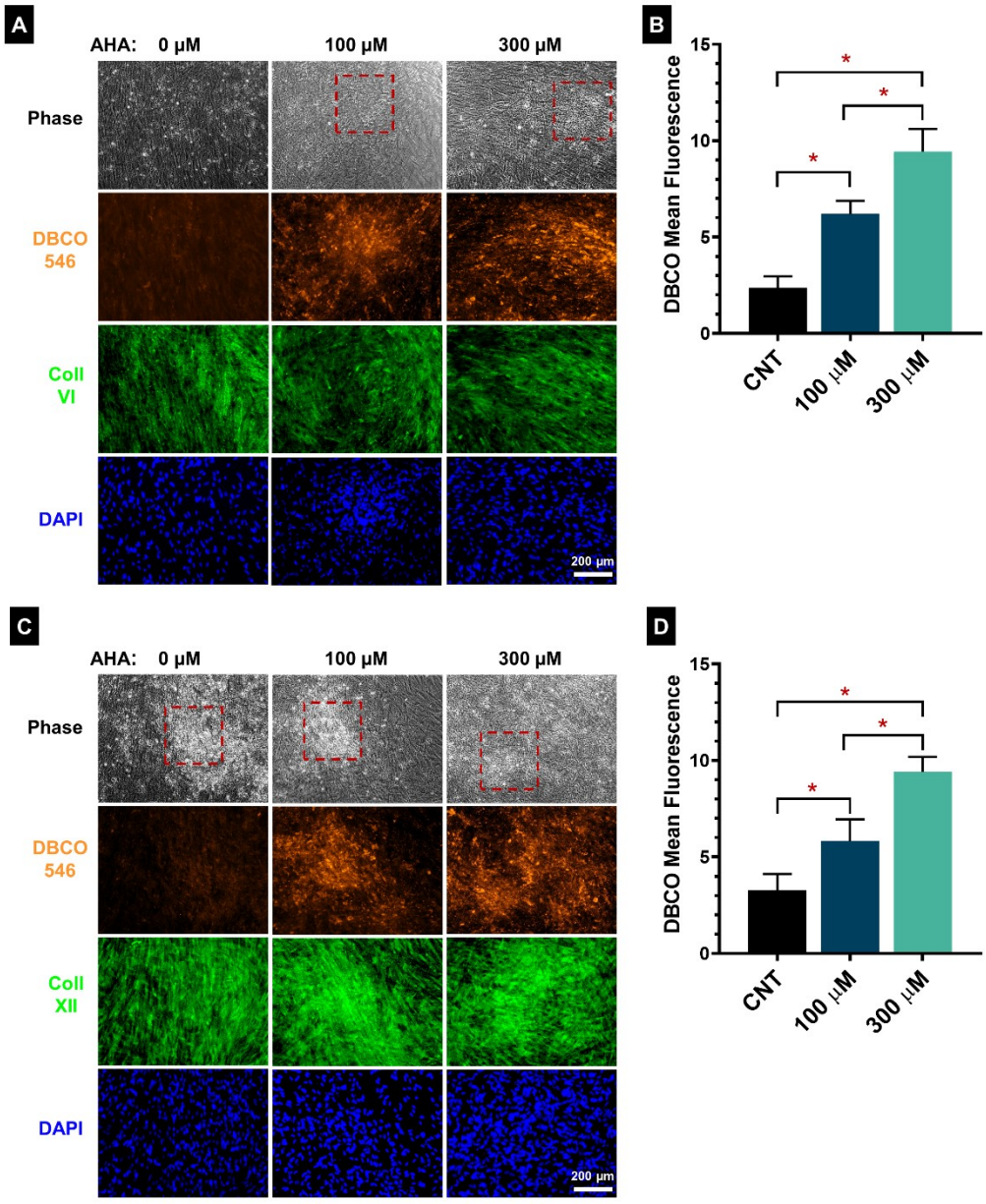

Figure 4.4: iP-hMSCs uptake and incorporate AHA into deposited ECM. Representative images of iP-hMSCs monolayers after 10 days of culture in the presence of 0, 100, and 300 µM of AHA and 10 µM of GW9662. Monolayers were labeled with DBCO-488 fluorescent tag, counterstained with DAPI, and either A) Coll VI or C) Coll XII. Cyclo-addition reaction between DBCO and AHA-containing proteins was performed. Red squares indicate bone-line nodules. The corresponding B) and D) mean fluorescence intensity for the DBCO-stained monolayers are shown on the right. Statistical analysis was performed by one-way ANOVA on the mean fluorescence of the DBCO-stained monolayers, followed by a Tukey's multiple comparison. Error bars depict standard deviation (n=4), and asterisks signify a significant difference ($p<0.05$).

4.3.4. AHA Modified Anabolic Bone ECM Retains Osteoinductive Properties

To evaluate whether AHA substitutions impacted the osteoinductive properties of the anabolic bone ECM, bone marrow derived hMSCs were cultured on ECM coated well plates up to 4 days. ALP activity of hMSCs cultured on ECM derived from GW9662 treated iP-hMSCs was comparable to that of hMSCs cultured on ECM derived from DMSO treated iP-hMSCs after 2 days of culture **(Figure 4.5A**). Metabolically incorporating the non-canonical amino acid did not affect ALP activity after 2 days of culture. After 4 days of culture, GW9662 derived ECM significantly upregulated ALP activity as compared to the DMSO derived ECM. Consistent with day 2 results, AHA substitutions into the ECM did not affect ALP activity. OPG, an early osteogenic biomarker, was also analyzed. Similar levels of OPG secretion were observed from hMSCs cultured on all four types of ECM after two days of culture (**Figure 4.5B**). After 4 days of culture, OPG secretion rose significantly relative to levels observed on day 2 in all cases (**Figure 4.5B**). Further, ECM derived from GW9662-treated iPhMSCs enhanced OPG secretion, resulting in significantly higher levels than those observed from hMSCs cultured on DMSO ECM for 4 days. In agreement with ALP activity results, AHA-substituted ECMs had comparable secretion levels relative to their standard ECM counterparts. Specifically, GW-ECM and GW-AHA ECM stimulated similar levels of OPG secretion (**Figure 4.5B**).

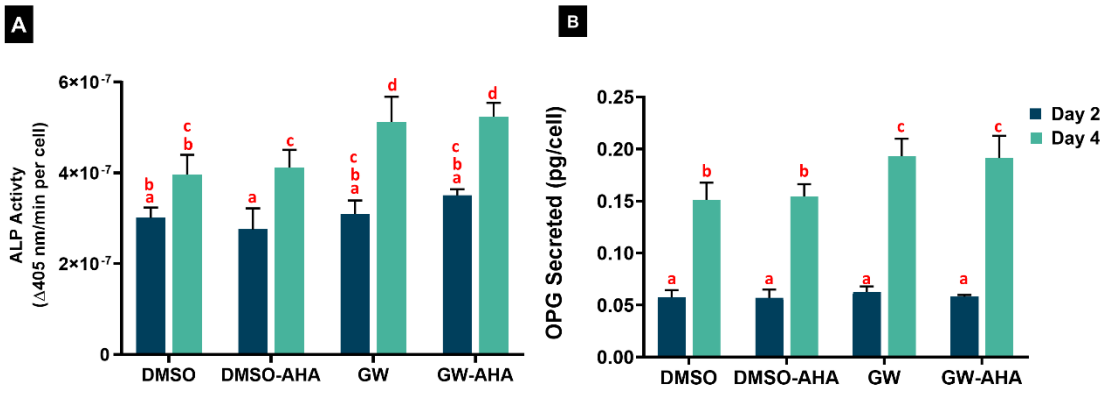

Figure 4.5: Inclusion of AHA into the anabolic bone ECM does not interfere with osteoinductive properties of the ECM. Bone marrow derived hMSCs cultured on tissue culture plates coated with standard and AHA-modified ECM show comparable A) ALP activity and B) OPG secretion. ECM derived from GW9662 treated cells accelerates expression of early osteogenic markers. Columns with matching letters indicate all possible comparisons were not significant. (n=3, error bars depict standard deviation, $p<0.05$, two-way ANOVA, Tukey's multiple comparison test).

4.4. Discussion

We investigated the strategy of incorporating azide-containing non-canonical amino acids into the anabolic bone ECM so as to exploit the azide-functionality and covalently attach the ECM onto scaffolds through strain-promoted azide-alkyne cycloaddition. We demonstrated metabolic incorporation of the non-canonical amino acid did not alter the composition or the osteoinductive properties of an iP-hMSCs derived ECM that resembles the anabolic bone microenvironment. Further, we demonstrated a possible strategy to functionalize established GelMA hydrogels surfaces with a cyclooctyne capable of participating in SPAAC chemistry. Although not accomplished in this work, these preliminary results strongly suggest covalent tethering of the anabolic bone ECM, a complex mixture of proteins, onto established scaffolds is possible without compromising the bioactivity of the ECM.

The regulatory role of the ECM has long been appreciated, motivating a multitude of approaches in designing scaffolds that mimic the composition and microstructure of healthy bone tissue. However, recapitulating the ECM of the osteogenic niche rather than homeostatic bone is a logically sound strategy to augmenting the osteoregenerative capabilities of engineered bone scaffolds. The collagenous ECM secreted by hMSCs treated with the PPAR-γ inhibitor GW9662 resembles the composition of anabolic bone, e.g. high levels of Coll VI and XII, and has been successfully employed in improving bone healing outcome in critical-sized defects in small-animal models[45,46]. A significant drawback to using hMSCs to produce ECM and other complex biological products is their limited proliferation potential and variability in cell behavior between donors. While iP-hMSCs provide a potential strategy in producing large quantities of the anabolic bone ECM from a genetically identical source in a reproducible manner, a lack of structural form limits the practicality of the ECM for bone repair. A strategy that covalently tethers ECM to established scaffolds without compromising the bioactivity of the ECM would facilitate its translation to clinical use.

GelMA hydrogels were chosen as a hydrogel model for DBCO functionalization as their ability to support cell adhesion[183], cell-induced matrix remodeling[112] and the ease in which they can be microfabricated into complex structures is well documented[56,185,186]. The conjugation of the DBCO functional handle on GelMA hydrogels was accomplished through the EDC/NHS chemistry, a commonly employed strategy in protein conjugation[187,188]. Due to a reduction in primary amines stemming from the initial fabrication of GelMA (methacrylation of gelatin)[183], the carboxylic side chains of GelMA

were leveraged during the EDC/NHS coupling. The activated NHS-ester would in turn react with the amine handle of the DBCO-Sulfo-PEG-Amine. The DBCO coupling was initially performed on GelMA while in solution (DBCO-GelMA^{BC}), allowing access to the entirety of the polymeric chains to be functionalized. DBCO-GelMA^{BC} could be photopatterned and retained azide-conjugated fluorescent tags for long periods of time compared to standard GelMA (*cf* **Figure 4.2A**). This would suggest DBCO was successfully conjugated and were capable of participating in the strain promoted cycloaddition. However, this bulk functionalization required downstream purification via desalting columns, dialysis, and lyophilization, resulting in some loss of GelMA material (approximately 77-89% recovery).

Given the goal to tether AHA-modified ECM is constrained to the surface of prepared scaffolds, conjugation of DBCO to the surface of GelMA hydrogels presented a more efficient approach that would circumvent issues with material loss. Conjugating DBCO on GelMA hydrogel surface revealed DBCO-GelMA^{AC} was also capable of retaining the azide-fluorescent tag (*cf* **Figure 4.2B**). Although the degree of DBCO functionalization between the two approaches was not measured and compared by previously described methods, e.g. H-NMR[189] or 1-pyrenyldiazomethane (PDAM)[190], the higher fluorescence intensity observed in the DBCO-GelMA^{AC} hydrogels suggest a higher capacity to click to the azide fluorescent tag (*cf* **Figure 4.2C**). To verify that the ability to retain the azide-fluorescent tag was due to DBCO conjugation and subsequent cycloaddition and not due to the increase in crosslinking density/decrease in swelling ratio caused by the EDC/NHS chemistry (**Figure Appendix 3**), a GelMA hydrogel that

underwent the EDC/NHS chemistry without being given the DBCO moiety was used a control. Both DBCO functionalization approaches had higher fluorescence than the control after 8 days in PBS (*cf.* **Figure 4.2C**), suggesting the decrease in swelling ratio played a negligible role in retaining the azide-fluorescent tag. Given the improved DBCO functionality, DBCO-GelMA^{AC} hydrogels were chosen for downstream use.

Metabolic incorporation of non-canonical amino acids have proven useful for visualizing translated intra[179,180] and extracellular proteins[181] in standard 2D culture, within cell-laden biomaterials[120,121,182], and in whole organisms (e.g. zebra fish, drosophila, murine embryos[128,191,192]). Here, iP-hMSCs cultures were simultaneously stimulated with GW9662 and provided AHA to be metabolically incorporated into the anabolic bone ECM. The composition of the ECM generated by hMSCs treated with GW9662 is characterized by high levels of Coll VI and Coll XII[45,46], and similar trends needed to be verified in iP-hMSC cultures. Although the expression of these two matrix proteins were evaluated in both the intracellular and extracellular fractions, the extracellular fraction is a closer approximation to the composition of the decellularized ECM that would be utilized during the cycloaddition with DBCO-GelMA^{AC}. In the extracellular fraction, Coll VI and Coll XII were highly expressed in iP-hMSCs even in the absence of GW9662 (*cf* **Figure 4.3 A&C**). Surprisingly, a higher Coll VI expression was observed in the vehicle controls compared to the GW9662 treated iP-hMSCs. However, GW9662 enhanced Coll XII expression in iP-hMSCs in the extracellular fraction (*cf* **Figure 4.3C**), consistent with previous results in hMSCs. Furthermore, GW9662 treatment also stimulated significantly higher protein deposition (*cf* **Figure**

4.3F), approximately 2.5-3 times higher than the vehicle control. A higher ECM yield would be beneficial during large-scale production and would facilitate the translation from benchtop to clinical use.

After confirming that AHA was globally incorporated into synthesized proteins and did not alter iP-hMSCs translational activity (**Figure Appendix 4**), we evaluated the degree in which AHA could be incorporated into Coll VI and Coll XII present in secreted ECM. Methionine constitutes approximately 1.5-2.1% of the amino acid content of the anabolic bone ECM secreted by GW9662-treated hMSCs[45], with similar levels calculated for Coll VI and Coll XII subunits (**Table Appendix 26**). Immunostaining against Coll VI and Coll XII in iP-hMSCs monolayers confirmed the expression trends observed during immunoblotting. Fluorescent tagging against AHA showed colocalization with the dense, highly fluorescent regions of Coll XII immunostaining (*cf* **Figure 4.4C**). These refringent bone-like nodules have been claimed to mimic endochondral ossification[193]. Given the importance of Coll XII in regulating terminal differentiation of osteoblasts[43], its high expression in these nodules is unsurprising and lends credence to *in-vitro* bone nodules recapitulating endochondral ossification. In contrast, secreted Coll VI and fluorescently tagged AHA-proteins had dissimilar distributions, with Coll VI uniformly expressed in the iP-hMSC monolayers (*cf* **Figure 4.4A**). It is possible the DBCO-fluorescent tag congregated to nodule formations simply due to a high concentration of ECM in these locations instead of an inherent difference in AHA-substitutions in Coll VI.

Although AHA can be recognized by endogenous methionyl-tRNA synthetase and tRNA pairs during translation, the kinetics are lower than that of its canonical

counterpart[181], and could also be partly responsible for the lack of spatial similarity between Coll VI and fluorescently tagged AHA-proteins. Genetic engineering and mutant aminoacyl-tRNA synthetase and tRNA pairs has been explored to improve the rate[191], the specificity[194], and versatility[195] of incorporating non-canonical amino acids into translated proteins. However, these approaches suffer from poor yields, can be labor intensive, and are limited to modifying singular proteins[196]. Thus, using non-canonical amino acids recognized by endogenous translational machinery is a more accessible approach that is particularly suitable for functionalizing a cocktail of proteins, as in the case of the anabolic bone ECM.Methionine-free media has been used to achieve a high percentage of AHA substitution[120,182], and should be explored as means of improving percentage of AHA substitution. However, to avoid altering established protocols with known growth trends in iP-hMSCs, we elected to continue with the established α-MEM based culture media. Instead, AHA concentration in supplemented media was increased, which did ultimately increase fluorescence tagging of AHA-proteins (*cf* **Figure 4.4D**). Improving AHA incorporation efficiency into the anabolic bone ECM could culminate into a denser anabolic bone ECM coating on the DBCO-GelMA^{AC} hydrogels.

Although it has been reported that incorporating AHA causes insignificant alterations in protein folding[128], we verified that the AHA-substitutions were not detrimental to the previously reported osteoinductive properties of the anabolic bone ECM (***cf* Figure 4.5**). The native and AHA-containing anabolic bone ECM enhanced the osteogenic characteristic of seeded hMSCs relative to their DMSO ECM counterparts to comparable degrees. These results suggest that the AHA-modified anabolic bone ECM

have the potential to be tethered to DBCO-GelMA^{AC} hydrogels and retain their osteoinductive properties. However, because methionine typically contributes to the hydrophobic cores of proteins[197], it is possible that tethering the anabolic bone ECM to DBCO-GelMA^{AC} could be hindered by limited accessibility between azides and the cycloalkyne. Continuation of this work entails performing the cycloaddition between AHA-containing ECM and DBCO-GelMA^{AC} hydrogels. Broad verification of ECM on hydrogel surface could be determined via SEM, while specific matrix proteins (Coll VI and Coll XII) could be evaluated via immunoblotting. Future *in vitro* work is needed to confirm the osteogenic potential of the ECM-tethered GelMA hydrogels. Lastly, while the intent of this work has been primarily to covalently tether an anabolic bone ECM onto hydrogel network for bone repair, the approach to metabolically incorporate azide functionality followed by immobilization via SPAAC could be applied to secreted factors found in conditioned media, which have also been explored for their therapeutic value[198–201].

4.5. Conclusion

We have demonstrated the feasibility of utilizing SPAAC technique in fabricating ECM-coated hydrogels. While metabolic-labelling of proteins with non-canonical amino acids has been traditionally implemented in identifying and visualizing newly synthesized proteins, here we implement it to imbue azide functionality into a complex anabolic bone ECM mixture. We verified that the AHA-modified ECM retains its osteoinductive properties. In addition, we developed a method to functionalize the DBCO moiety onto GelMA hydrogels. These hydrogels retained azide-conjugated fluorescent tags for long

periods of time, indicating covalent tethering to the hydrogel. Although future *in vitro* work is needed to confirm the osteogenic potential of the ECM-tethered GelMA hydrogels, this approach hold promise in augmenting the osteoregenerative properties of existing scaffolds.

5. CONCLUSION

5.1. Summary of Dissertation and Future Work

Despite their limited availability and association with donor site morbidity, autologous bone grafts remain the gold standard treatment for bone repair. Efforts to engineer bone graft substitutes have relied heavily on mimicking key compositional and physical properties of adult homeostatic bone, which has yielded mixed results. Interestingly, the morphological processes that allow bone to regenerate under ideal conditions bears a strong resemblance to developing bone in utero and to growing bone in children/adolescents. Mimicking the key features of developing/growing bone rather than homeostatic bone holds great promises in designing engineered bone tissues for bone repair.

The work presented in Section 2 show a possible translational route for an anabolic bone ECM secreted by hMSCs and iP-hMSCs first reported by our collaborator. In Section 2, I examined the influence of controlled release of GW9662 and perfusion on the deposition of the anabolic bone ECM by human mesenchymal stem cells cultured on osteoinductive scaffold (Coll/MgHA) in a perfusion bioreactor. An improvement in deposition of the anabolic bone ECM relative to both static and vehicle controls showed a synergistic relationship between perfusion and GW9662 treatment, from either the drug-eluting microspheres or media supplementation, resulting in a scaffold that recapitulated both the inorganic and organic fraction of nascent bone. Future *in vivo* work is needed to determine whether Coll/MgHA scaffolds embedded with GW9662-eluting microspheres

can incite native osteoprogenitors cells to deposit the anabolic bone ECM at levels that result in improved bone healing. In addition, the data presented in this section suggests that GW9662 treatment and a perfusion culture system can be utilized to deposit the anabolic bone ECM to augment the osteoregenerative properties of existing scaffolds.

Laponite, a synthetic silicate nanoplatelets (nSi) commonly employed to modulate the rheological properties of polymer-based hydrogels, are an attractive nanoparticle for bone repair due to previously reported osteoinductive properties. Despite their popularity, the mechanism by which nSi impart their osteoinductive effects in not entirely understood in 2D, less so in the 3D microenvironment of hydrogels. Conventional knowledge on nSi-based nanocomposites touts their improved mechanical properties and their internalization into cell bodies and subsequent ionic dissolution as the driving force behind the enhanced osteo-regenerative capabilities. In Section 3, I work to decouple the network-fortifying properties of nSi and the effects of nSi internalization/ionic dissolution on hMSC differentiation in a collagen hydrogel platform (Coll-nSi). I demonstrated that neither matrix stiffening and nSi internalization truly captures the microenvironment experienced by hMSCs in Coll-nSi nanocomposites or explain the improved osteogenic response. Instead, I showed that nSi aggregates sequester and accumulate the cargo of secreted extracellular vesicle, and that the improved osteogenic response in Coll-nSi nanocomposite could be due in part to nSi hijacking trophic activity.

A significant drawback to using hMSCs to produce the anabolic bone ECM is their limited proliferation potential and variability in cell behavior between donors. In addition, the process of bioconditioning established scaffolds requires decellularization, which has

been proven to be detrimental to mechanical properties of hydrogel-based scaffolds. To address these limitations, hMSCs generated from human induced pluripotent stem cells (iP-hMSCs) were instead utilized to produce the anabolic bone ECM for the work presented in Section 4. In addition, I explore the feasibility of covalently tethering the iP-hMSCs derived anabolic bone ECM onto established scaffolds through strain-promoted azide-alkyne cyclo addition (SPAAC). I demonstrated that azide functionality can be metabolically incorporated into iP-MSCs-derived anabolic bone ECM without negatively impacting the composition or the osteoinductive properties of the ECM. In addition, the azide moieties in the ECM were still able to partake in SPAAC click reaction. I fabricated gelatin-methacryloyl (GelMA) hydrogels functionalized with dibenzocyclooctyne (DBCO) that can also participate in SPAAC click reaction.

Future work will focus on verifying covalent tethering of the ECM to GelMA can occurred. In addition, in-vitro work is required to assess the osteogenic potential of ECM-tethered GelMA hydrogels. Successful execution of this work holds great promise for other GelMA-based scaffolds. We have previously augmented the osteoinductive properties of 3D-printed Nanoengineered Ionic-Covalent Entanglement (NICE) scaffolds through the bioconditioning process. The NICE ink platform consists of two interpenetrating polymer networks, one of which is GelMA. Despite a robust increase in the expression of osteogenic markers (**Figure 1.3C-E**) and mineralization (**Figure 1.3F**), bioconditioning of NICE necessitates it to undergo the decellularization process and weaken its mechanical properties (**Figure 1.3A-B).** DBCO functionalization of NICE would allow its surface to be covalently tethered to azide-functionalized anabolic bone

ECM without undergoing the decellularization process. Coupled with the tunability in microarchitecture provided by 3D printing, the resulting biodegradable scaffold holds great potential as an engineered bone graft.

REFERENCES

1. Nauth, A., Miclau, T., Li, R. & Schemitsch, E. H. Gene therapy for fracture healing. *J. Orthop. Trauma* **24**, 17–24 (2010).
2. Zura, R. *et al.* Bone fracture nonunion rate decreases with increasing age: A prospective inception cohort study. *Bone* **95**, 26–32 (2017).
3. Ensrud, K. E. Epidemiology of Fracture Risk With Advancing Age. *Journals Gerontol. Ser. A Biol. Sci. Med. Sci.* **68**, 1236–1242 (2013).
4. Amini, A. R., Laurencin, C. T. & Nukavarapu, S. P. Bone Tissue Engineering: Recent Advances and Challenges. *Crit. Rev. Biomed. Eng.* **40**, 363–408 (2012).
5. Wang, W. & Yeung, K. W. K. Bone grafts and biomaterials substitutes for bone defect repair: A review. *Bioact. Mater.* **2**, 224–247 (2017).
6. Flierl, M. A. *et al.* Outcomes and complication rates of different bone grafting modalities in long bone fracture nonunions: a retrospective cohort study in 182 patients. *J. Orthop. Surg. Res.* **8**, 33 (2013).
7. Brydone, A. S., Meek, D. & MacLaine, S. Bone grafting, orthopaedic biomaterials, and the clinical need for bone engineering. *Proc. Inst. Mech. Eng. Part H J. Eng. Med.* **224**, 1329–1343 (2010).
8. Greenwald, A. S. *et al.* Bone-Graft Substitutes: Facts, Fictions, and Applications. *J. Bone Jt. Surgery-American Vol.* **83**, 98–103 (2001).
9. Gelinsky, M., Welzel, P. B., Simon, P., Bernhardt, A. & König, U. Porous three-dimensional scaffolds made of mineralised collagen: Preparation and properties of a biomimetic nanocomposite material for tissue engineering of bone. *Chem. Eng.*

J. **137**, 84–96 (2008).

10. Roseti, L. *et al.* Scaffolds for Bone Tissue Engineering: State of the art and new perspectives. *Mater. Sci. Eng. C* **78**, 1246–1262 (2017).
11. Lenas, P., Moos, M. & Luyten, F. P. Developmental engineering: A new paradigm for the design and manufacturing of cell-based products. Part I: From three-dimensional cell growth to biomimetics of in Vivo development. *Tissue Eng. - Part B Rev.* **15**, 381–394 (2009).
12. Einhorn, T. A. & Gerstenfeld, L. C. Fracture healing: mechanisms and interventions. *Nat. Rev. Rheumatol.* **11**, 45–54 (2015).
13. Dirckx, N., Van Hul, M. & Maes, C. Osteoblast recruitment to sites of bone formation in skeletal development, homeostasis, and regeneration. *Birth Defects Res. Part C - Embryo Today Rev.* **99**, 170–191 (2013).
14. Little, D. G., Ramachandran, M. & Schindeler, A. The anabolic and catabolic response in bone repair. *J. Bone Joint Surg. Br.* **89-B**, 425–433 (2007).
15. Gerstenfeld, L. C., Cullinane, D. M., Barnes, G. L., Graves, D. T. & Einhorn, T. A. Fracture healing as a post-natal developmental process: Molecular, spatial, and temporal aspects of its regulation. *J. Cell. Biochem.* **88**, 873–884 (2003).
16. Carrington, J. L. & Reddi, A. H. Parallels between development of embryonic and matrix-induced endochondral bone. *BioEssays* **13**, 403–408 (1991).
17. Kakei, M., Nakahara, H., Tamura, N., Itoh, H. & Kumegawa, M. Behavior of carbonate and magnesium ions in the initial crystallites at the early developmental stages of the rat calvaria. *Ann. Anat.* **179**, 311–316 (1997).

18. Kohara, Y., Soeta, S., Izu, Y. & Amasaki, H. Accumulation of type VI collagen in the primary osteon of the rat femur during postnatal development. *J. Anat.* **226**, 478–488 (2015).

19. Christensen, S. E. *et al.* Altered Trabecular Bone Structure and Delayed Cartilage Degeneration in the Knees of Collagen VI Null Mice. *PLoS One* **7**, e33397 (2012).

20. Shim, K. S. Pubertal growth and epiphyseal fusion. *Ann. Pediatr. Endocrinol. Metab.* **20**, 8 (2015).

21. Biga, L. M. *et al.* Bone Formation and Development. in *Anatomy & Physiology* (OpenStax/Oregon State University, 2016). http://cnx.org/contents/14fb4ad7-39a1-4eee-ab6e-3ef2482e3e22@8.24.

22. Shapiro, F., Holtrop, M. & Glimcher, M. Organization and cellular biology of the perichondrial ossification groove of ranvier. *J. Bone Jt. Surg.* **59**, 703–723 (1977).

23. Schollmeier, G., Uhthoff, H. K., Lewandrowski, K.-U. & Fukuhara, K. Role of Bone Bark During Growth in Width of Tubular Bones A Study in Human Fetuses. *Clin. Orthop. Relat. Res.* **367**, 291–299 (1999).

24. Kohara, Y., Soeta, S., Izu, Y., Arai, K. & Amasaki, H. Distribution of type VI collagen in association with osteoblast lineages in the groove of Ranvier during rat postnatal development. *Ann. Anat.* **208**, 58–68 (2016).

25. Shapiro, F. Bone development and its relation to fracture repair. The role of mesenchymal osteoblasts and surface osteoblasts. *Eur. Cells Mater.* **15**, 53–76 (2008).

26. Abe, Y., Kokubo, T. & Yamamuro, T. Apatite coating on ceramics, metals and polymers utilizing a biological process. *J. Mater. Sci. Mater. Med.* **1**, 233–238 (1990).

27. Uddin, M. S. *et al.* Surface treatments for controlling corrosion rate of biodegradable Mg and Mg-based alloy implants Surface treatments for controlling corrosion rate of biodegradable Mg and Mg-based alloy implants. *Sci. Technol. Adv. Mater.* **16**, 53501 (2015).

28. Bohner, M. Calcium orthophosphates in medicine: From ceramics to calcium phosphate cements. *Injury* **31**, (2000).

29. Thakur, T. *et al.* Photocrosslinkable and Elastomeric Hydrogels for Bone Regeneration. *J. Biomed. Mater. Res. A* **104**, 879–888 (2015).

30. Gaharwar, A. K., Dammu, S. A., Canter, J. M., Wu, C. J. & Schmidt, G. Highly extensible, tough, and elastomeric nanocomposite hydrogels from poly(ethylene glycol) and hydroxyapatite nanoparticles. *Biomacromolecules* **12**, 1641–1650 (2011).

31. Shim, J. H. *et al.* Fabrication of blended polycaprolactone/poly (Lactic-Co-Glycolic Acid)/β-tricalcium phosphate thin membrane using solid freeform fabrication technology for guided bone regeneration. *Tissue Eng. - Part A* **19**, 317–328 (2013).

32. Eggli, P. S., Müller, W. & Schenk, R. K. Porous hydroxyapatite and tricalcium phosphate cylinders with two different pore size ranges implanted in the cancellous bone of rabbits. A comparative histomorphometric and histologic

study of bony ingrowth and implant substitution. *Clin. Orthop. Relat. Res.* 127–38 (1988).

33. Barber, F. A. & Dockery, W. D. Long-term Absorption of β-Tricalcium Phosphate Poly-L-Lactic Acid Interference Screws. *Arthrosc. - J. Arthrosc. Relat. Surg.* **24**, 441–447 (2008).

34. Landi, E. *et al.* Biomimetic Mg-substituted hydroxyapatite: From synthesis to in vivo behaviour. *J. Mater. Sci. Mater. Med.* **19**, 239–247 (2008).

35. Rey, C., Combes, C., Drouet, C. & Glimcher, M. J. Bone mineral: update on chemical composition and structure. *Osteoporos. Int.* **20**, 1013–1021 (2009).

36. Figueiredo, M. M., Gamelas, J. A. F. & Martins, A. G. Characterization of Bone and Bone-Based Graft Materials Using FTIR Spectroscopy. in *Infrared Spectroscopy - Life and Biomedical Sciences* 315–338 (2012). doi:10.5772/36379.

37. Quint, P., Althoff, J., Höhling, H. J., Boyde, A. & Laabs, W. A. Characteristic molar ratios of magnesium, carbon dioxide, calcium and phosphorus in the mineralizing fracture callus and predentine. *Calcif. Tissue Int.* **32**, 257–261 (1980).

38. De Lima, I. R. *et al.* Understanding the impact of divalent cation substitution on hydroxyapatite: An in vitro multiparametric study on biocompatibility. *J. Biomed. Mater. Res. - Part A* **98 A**, 351–358 (2011).

39. Dvir, T., Timko, B. P., Kohane, D. S. & Langer, R. Nanotechnological strategies for engineering complex tissues. *Nat. Nanotechnol.* **6**, 13–22 (2011).

40. Marvulli, D. & Bressan, G. M. Spatial and Temporal Changes of Type VI

Collagen During Mouse Development. *Dev. Dyn.* **206**, 447–454 (1996).

41. Yamazaki, M., Majeska, R. J., Yoshioka, T., Moriya, H. & Einhorn, A. Spatial and Temporal Expression of Fibril-Forming Minor Collagen Genes (Types V and XI) during Fracture Healing. *J. Bone Jt. Surg.* **15**, 757–764 (1997).

42. Wälchli, C., Koch, M., Chiquet, M., Odermatt, B. F. & Trueb, B. Tissue-specific expression of the fibril-associated collagens XII and XIV. *J. Cell Sci.* **107**, 669–81 (1994).

43. Izu, Y. *et al.* Type XII collagen regulates osteoblast polarity and communication during bone formation. *J. Cell Biol.* **193**, 1115–1130 (2011).

44. Krause, U. *et al.* Pharmaceutical modulation of canonical Wnt signaling in multipotent stromal cells for improved osteoinductive therapy. *Proc. Natl. Acad. Sci.* **107**, 4147–4152 (2010).

45. Zeitouni, S. *et al.* Human mesenchymal stem cell-derived matrices for enhanced osteoregeneration. *Sci. Transl. Med.* **4**, 132ra55 (2012).

46. Clough, B. H. *et al.* Bone regeneration with osteogenically enhanced mesenchymal stem cells and their extracellular matrix proteins. *J. Bone Miner. Res.* **30**, 83–94 (2015).

47. Clough, B. H. *et al.* An allograft generated from adult stem cells and their secreted products efficiently fuses vertebrae in immunocompromised athymic rats and inhibits local immune responses. *Spine J.* **17**, 418–430 (2017).

48. Pati, F. *et al.* Ornamenting 3D printed scaffolds with cell-laid extracellular matrix for bone tissue regeneration. *Biomaterials* **37**, 230–241 (2015).

49. Decaris, M. L., Binder, B. Y., Soicher, M. A., Bhat, A. & Leach, J. K. Cell-derived matrix coatings for polymeric scaffolds. *Tissue Eng. - Part A* **18**, 2148–2157 (2012).

50. Pham, Q. P. *et al.* Analysis of the osteoinductive capacity and angiogenicity of an in vitro generated extracellular matrix. *J. Biomed. Mater. Res. Part A* **88**, 295–303 (2009).

51. Pham, Q. P. *et al.* The influence of an in vitro generated bone-like extracellular matrix on osteoblastic gene expression of marrow stromal cells. *Biomaterials* **29**, 2729–2739 (2008).

52. Bai, F. *et al.* The effect of pore size on tissue ingrowth and neovascularization in porous bioceramics of controlled architecture in vivo. *Biomed. Mater.* **6**, (2011).

53. Scheinpflug, J. *et al.* Journey into bone models: A review. *Genes (Basel).* **9**, (2018).

54. Hogrebe, N. J., Reinhardt, J. W. & Gooch, K. J. Review Article Biomaterial microarchitecture : a potent regulator of individual cell behavior and multicellular organization. *J. Biomed. Mater. Res. Part A* **105**, 640–661 (2017).

55. Seol, Y. J., Kang, T. Y. & Cho, D. W. Solid freeform fabrication technology applied to tissue engineering with various biomaterials. *Soft Matter* vol. 8 1730–1735 (2012).

56. Chimene, D. *et al.* Nanoengineered Ionic-Covalent Entanglement (NICE) Bioinks for 3D Bioprinting. *ACS Appl. Mater. Interfaces* **10**, 9957–9968 (2018).

57. Gaharwar, A. K. *et al.* Bioactive silicate nanoplatelets for osteogenic

differentiation of human mesenchymal stem cells. *Adv. Mater.* **25**, 3329–3336 (2013).

58. Carrow, J. K. *et al.* Widespread changes in transcriptome profile of human mesenchymal stem cells induced by two-dimensional nanosilicates. *Proc. Natl. Acad. Sci.* **115**, E3905–E3913 (2018).

59. Mihaila, S. M. *et al.* The osteogenic differentiation of SSEA-4 sub-population of human adipose derived stem cells using silicate nanoplatelets. *Biomaterials* **35**, 9087–9099 (2014).

60. Sears, C. *et al.* Conditioning of 3D Printed Nanoengineered Ionic–Covalent Entanglement Scaffolds with iP-hMSCs Derived Matrix. *Adv. Healthc. Mater.* 1901580 (2020).

61. Frohlich, M. *et al.* Tissue Engineered Bone Grafts: Biological Requirements, Tissue Culture and Clinical Relevance. *Curr. Stem Cell Res. Ther.* **3**, 254–264 (2008).

62. Bianco, P., Riminucci, M., Gronthos, S. & Robey, P. G. Bone Marrow Stromal Stem Cells: Nature, Biology, and Potential Applications. *Stem Cells* **19**, 180–192 (2001).

63. Wagner, W., Horn, P., Castoldi, M., Diehlmann, A. & Bork, S. Replicative Senescence of Mesenchymal Stem Cells: A Continuous and Organized Process. *PLoS One* **3**, 2213 (2008).

64. Banfi, A. *et al.* Replicative Aging and Gene Expression in Long-Term Cultures of Human Bone Marrow Stromal Cells. *Tissue Eng.* **8**, 901–910 (2002).

65. Ho, A. D., Wagner, W. & Franke, W. Heterogeneity of mesenchymal stromal cell preparations. *Cytotherapy* **10**, 320–330 (2008).

66. Wagner, W. & Ho, A. D. Mesenchymal stem cell preparations-comparing apples and oranges. *Stem Cell Rev.* **3**, 239–248 (2007).

67. Mauney, J. R. *et al.* Matrix-mediated retention ofin vitro osteogenic differentiation potential andin vivo bone-forming capacity by human adult bone marrow-derived mesenchymal stem cells duringex vivo expansion. *J. Biomed. Mater. Res. Part A* **79A**, 464–475 (2006).

68. Mareschi, K. *et al.* Expansion of mesenchymal stem cells isolated from pediatric and adult donor bone marrow. *J. Cell. Biochem.* **97**, 744–754 (2006).

69. Zhao, Q. *et al.* MSCs derived from iPSCs with a modified protocol are tumor-tropic but have much less potential to promote tumors than bone marrow MSCs. *Proc. Natl. Acad. Sci. U. S. A.* **112**, 530–535 (2015).

70. Liao, J. *et al.* Modulation of osteogenic properties of biodegradable polymer/extracellular matrix scaffolds generated with a flow perfusion bioreactor. *Acta Biomater.* **6**, 2386–2393 (2010).

71. Stiehler, M. *et al.* Effect of dynamic 3-D culture on proliferation, distribution, and osteogenic differentiation of human mesenchymal stem cells. *J. Biomed. Mater. Res. Part A* **89**, 96–107 (2008).

72. Rauh, J., Milan, F., Günther, K. P. & Stiehler, M. Bioreactor systems for bone tissue engineering. *Tissue Eng. - Part B Rev.* **17**, 263–280 (2011).

73. Vunjak-Novakovic, G. *et al.* Bioreactor cultivation conditions modulate the

composition and mechanical properties of tissue-engineered cartilage. *J. Orthop. Res.* **17**, 130–138 (1999).

74. Marijanovic, I., Antunovic, M., Matic, I., Panek, M. & Ivkovic, A. Bioreactor-Based Bone Tissue Engineering. in *Advanced Techniques in Bone Regeneration* (ed. Miranda, A. R. Z. and J. B. de) (IntechOpen, 2016). doi:10.5772/62546.

75. Grayson, W. L. *et al.* Optimizing the medium perfusion rate in bone tissue engineering bioreactors. *Biotechnol. Bioeng.* **108**, 1159–1170 (2011).

76. Grayson, W. L. *et al.* Effects of Initial Seeding Density and Fluid Perfusion Rate on Formation of Tissue-Engineered Bone. *Tissue Eng. Part A* **14**, 1809–1820 (2008).

77. Wendt, D. *et al.* Bioreactors for tissue engineering. in *Tissue Engineering* (eds. Blitterswijk, C. van et al.) 483–506 (Elsevier, 2008). doi:10.1016/B978-0-12-370869-4.00016-1.

78. Minardi, S. *et al.* Evaluation of the osteoinductive potential of a bio-inspired scaffold mimicking the osteogenic niche for bone augmentation. *Biomaterials* **62**, 128–37 (2015).

79. Ratnayake, J. T. B., Mucalo, M. & Dias, G. J. Substituted hydroxyapatites for bone regeneration : A review of current trends. *J. Biomed. Mater. Res. Part B Appl. Biomater.* **105**, 1285–1299 (2017).

80. Su, J. Enhanced biocompatibility and osteogenic potential of mesoporous magnesium silicate / polycaprolactone / wheat protein composite scaffolds. *Int. J. Nanomedicine* **13**, 1107–1117 (2018).

81. He, D., Dong, W. & Tang, S. Tissue engineering scaffolds of mesoporous magnesium silicate and poly (e -caprolactone)– poly (ethylene glycol)– poly (e -caprolactone) composite. *J. Mater. Sci. Mater. Med.* **25**, 1415–1424 (2014).

82. Chaya, A. *et al.* In vivo study of magnesium plate and screw degradation and bone fracture healing. *Acta Biomater.* **18**, 262–269 (2015).

83. Datta, N., Holtorf, H. L., Sikavitsas, V. I., Jansen, J. A. & Mikos, A. G. Effect of bone extracellular matrix synthesized in vitro on the osteoblastic differentiation of marrow stromal cells. *Biomaterials* **26**, 971–977 (2005).

84. Fan, D. *et al.* Mesoporous silicon-PLGA composite microspheres for the double controlled release of biomolecules for orthopedic tissue engineering. *Adv. Funct. Mater.* **22**, 282–293 (2012).

85. Minardi, S. *et al.* Multiscale patterning of a biomimetic scaffold integrated with composite microspheres. *Small* **10**, 3943–3953 (2014).

86. Pandolfi, L. *et al.* Composite microsphere-functionalized scaffold for the controlled release of small molecules in tissue engineering. *J. Tissue Eng.* **7**, (2016).

87. Tsao, C. J. *et al.* Controlled Release of Small Molecules for Cardiac Differentiation of Pluripotent Stem Cells. *Tissue Eng. - Part A* **24**, 1798–1807 (2018).

88. Livak, K. J. & Schmittgen, T. D. Analysis of relative gene expression data using real-time quantitative PCR and the 2-ΔΔCT method. *Methods* **25**, 402–408 (2001).

89. Bouxsein, M. L. *et al.* Guidelines for assessment of bone microstructure in rodents using micro-computed tomography. *J. Bone Miner. Res.* **25**, 1468–1486 (2010).

90. Kourkoumelis, N. & Tzaphlidou, M. Spectroscopic Assessment of Normal Cortical Bone: Differences in Relation to Bone Site and Sex. *Sci. World J.* **10**, 402–412 (2010).

91. Bais, M., Mclean, J., Sebastiani, P., Young, M. & Wigner, N. Transcriptional Analysis of Fracture Healing and the Induction of Embryonic Stem Cell-Related Genes. *PLoS One* **4**, (2009).

92. Teo, J. C. M., Si-Hoe, K. M., Keh, J. E. L. & Teoh, S. H. Relationship between CT intensity, micro-architecture and mechanical properties of porcine vertebral cancellous bone. *Clin. Biomech.* **21**, 235–244 (2006).

93. Li, X., Ycaza, J. & Blumberg, B. The environmental obesogen tributyltin chloride acts via peroxisome proliferator activated receptor gamma to induce adipogenesis in murine 3T3-L1 preadipocytes. *J. Steroid Biochem. Mol. Biol.* **127**, 9–15 (2011).

94. Sakaguchi, Y. *et al.* Suspended cells from trabecular bone by collagenase digestion become virtually identical to mesenchymal stem cells obtained from marrow aspirates. *Blood* **104**, 2728–35 (2004).

95. Correia, C., Bhumiratana, S., Sousa, R. A., Reis, R. L. & Vunjak-Novakovic, G. Sequential application of steady and pulsatile medium perfusion enhanced the formation of engineered bone. *Tissue Eng. Part A* **19**, 1244–1254 (2013).

96. Bara, J. J., Richards, R. G., Alini, M. & Stoddart, M. J. Concise review: Bone

marrow-derived mesenchymal stem cells change phenotype following in vitro culture: Implications for basic research and the clinic. *Stem Cells* **32**, 1713–1723 (2014).

97. Lu, Z. & Zreiqat, H. The Osteoconductivity of Biomaterials Is Regulated by Bone Morphogenetic Protein 2 Autocrine Loop Involving α2β1 Integrin and Mitogen-Activated Protein Kinase/Extracellular Related Kinase Signaling Pathways. *Tissue Eng. Part A* **16**, 3075–3084 (2010).

98. Chen, J. C. & Jacobs, C. R. Mechanically induced osteogenic lineage commitment of stem cells. *Stem Cell Res. Ther.* **4**, 107 (2013).

99. Arai, K., Nagashima, Y., Takemoto, T. & Nishiyama, T. Mechanical Strain Increases Expression of Type XII Collagen in Murine Osteoblastic MC3T3-E1 Cells. *Cell Struct. Funct.* **33**, 203–210 (2008).

100. Chen, W.-T. *et al.* Alteration of mesenchymal stem cells polarity by laminar shear stimulation promoting β-catenin nuclear localization. *Biomaterials* **190**–**191**, 1–10 (2019).

101. Arnsdorf, E. J., Tummala, P. & Jacobs, C. R. Non-Canonical Wnt Signaling and N-Cadherin Related β-Catenin Signaling Play a Role in Mechanically Induced Osteogenic Cell Fate. *PLoS One* **4**, e5388 (2009).

102. Follet, H., Boivin, G., Rumelhart, C. & Meunier, P. J. The degree of mineralization is a determinant of bone strength: A study on human calcanei. *Bone* **34**, 783–789 (2004).

103. Trombetta, R., Inzana, J. A., Schwarz, E. M., Kates, S. L. & Awad, H. A. 3D

Printing of Calcium Phosphate Ceramics for Bone Tissue Engineering and Drug Delivery. *Ann. Biomed. Eng.* **45**, 23–44 (2017).

104. Gao, G. *et al.* Bioactive nanoparticles stimulate bone tissue formation in bioprinted three-dimensional scaffold and human mesenchymal stem cells. *Biotechnol. J.* **9**, 1304–1311 (2014).

105. Ren, X. *et al.* Nanoparticulate mineralized collagen scaffolds induce in vivo bone regeneration independent of progenitor cell loading or exogenous growth factor stimulation. *Biomaterials* **89**, 67–78 (2016).

106. Taraballi, F., Bauza, G., McCulloch, P., Harris, J. & Tasciotti, E. Concise Review: Biomimetic Functionalization of Biomaterials to Stimulate the Endogenous Healing Process of Cartilage and Bone Tissue. *Stem Cells Transl. Med.* **6**, 2186–2196 (2017).

107. Blokhuis, T. J. & Arts, J. J. C. Bioactive and osteoinductive bone graft substitutes: Definitions, facts and myths. *Injury* **42**, S26–S29 (2011).

108. Shi, P. *et al.* Self-Assembling Nanoclay Diffusion Gels for Bioactive Osteogenic Microenvironments. *Adv. Healthc. Mater.* **7**, 1800331 (2018).

109. Sheikhi, A., Afewerki, S., Oklu, R., Gaharwar, A. K. & Khademhosseini, A. Effect of ionic strength on shear-thinning nanoclay-polymer composite hydrogels. *Biomater. Sci.* **6**, 2073–2083 (2018).

110. Zulian, L., Augusto De Melo Marques, F., Emilitri, E., Ruocco, G. & Ruzicka, B. Dual aging behaviour in a clay-polymer dispersion. *Soft Matter* **10**, 4513–4521 (2014).

111. Xavier, J. R. *et al.* Bioactive nanoengineered hydrogels for bone tissue engineering: A growth-factor-free approach. *ACS Nano* **9**, 3109–3118 (2015).

112. Paul, A. *et al.* Nanoengineered biomimetic hydrogels for guiding human stem cell osteogenesis in three dimensional microenvironments. *J. Mater. Chem. B* **4**, 3544–3554 (2016).

113. Gaharwar, A. K. *et al.* 2D Nanoclay for Biomedical Applications: Regenerative Medicine, Therapeutic Delivery, and Additive Manufacturing. *Adv. Mater.* **31**, 1900332 (2019).

114. Huebsch, N. *et al.* Harnessing traction-mediated manipulation of the cell/matrix interface to control stem-cell fate. *Nat. Mater.* **9**, 518–26 (2010).

115. Baker, B. M. *et al.* Cell-mediated fibre recruitment drives extracellular matrix mechanosensing in engineered fibrillar microenvironments. *Nat. Mater.* **14**, 1262–1268 (2015).

116. Chaudhuri, O. *et al.* Hydrogels with tunable stress relaxation regulate stem cell fate and activity. *Nat. Mater.* **15**, 326–333 (2015).

117. Zoumi, A., Yeh, A. & Tromberg, B. J. Imaging cells and extracellular matrix in vivo by using second-harmonic generation and two-photon excited fluorescence. *Proc. Natl. Acad. Sci. U. S. A.* **99**, 11014–9 (2002).

118. Krause, U., Seckinger, A. & Gregory, C. A. Assays of osteogenic differentiation by cultured human mesenchymal stem cells. in *Methods in molecular biology (Clifton, N.J.)* vol. 698 215–230 (2011).

119. Gregory, C. A., Grady Gunn, W., Peister, A. & Prockop, D. J. An Alizarin red-

based assay of mineralization by adherent cells in culture: comparison with cetylpyridinium chloride extraction. *Anal. Biochem.* **329**, 77–84 (2004).

120. Loebel, C., Mauck, R. L. & Burdick, J. A. Local nascent protein deposition and remodelling guide mesenchymal stromal cell mechanosensing and fate in three-dimensional hydrogels. *Nat. Mater.* **18**, 883–891 (2019).

121. McLeod, C. M. & Mauck, R. L. High fidelity visualization of cell-to-cell variation and temporal dynamics in nascent extracellular matrix formation. *Sci. Rep.* **6**, 38852 (2016).

122. Heng, S. *et al.* Posttranslational Activation of Bone Morphogenetic Protein 2 Is Mediated by Proprotein Convertase 6 during Decidualization for Pregnancy Establishment. *Endocrinology* **151**, 3909–3917 (2010).

123. Felin, J. E. *et al.* Nuclear variants of bone morphogenetic proteins. *BMC Cell Biol.* **11**, 20 (2010).

124. Shi, J., Wang, C., Ngai, T. & Lin, W. Diffusion and Binding of Laponite Clay Nanoparticles into Collagen Fibers for the Formation of Leather Matrix. *Langmuir* **34**, 7379–7385 (2018).

125. Dehring, K. A., Smukler, A. R., Roessler, B. J. & Morris, M. D. Correlating Changes in Collagen Secondary Structure with Aging and Defective Type II Collagen by Raman Spectroscopy. *Appl. Spectrosc.* **60**, 366–372 (2006).

126. Agnihotri, R. *et al.* Osteopontin, a Novel Substrate for Matrix Metalloproteinase-3 (Stromelysin-1) and Matrix Metalloproteinase-7 (Matrilysin). *J. Biol. Chem.* **276**, 28261–28267 (2001).

127. tom Dieck, S. *et al.* Metabolic Labeling with Noncanonical Amino Acids and Visualization by Chemoselective Fluorescent Tagging. in *Current Protocols in Cell Biology* vol. 1 (John Wiley & Sons, Inc., 2012).

128. Hinz, F. I., Dieterich, D. C., Tirrell, D. A. & Schuman, E. M. Noncanonical amino acid labeling in vivo to visualize and affinity purify newly synthesized proteins in larval zebrafish. *ACS Chem. Neurosci.* **3**, 40–49 (2012).

129. Khosla, S. Minireview: The OPG/RANKL/RANK System. *Endocrinology* **142**, 5050–5055 (2001).

130. James, A. W. & W., A. Review of Signaling Pathways Governing MSC Osteogenic and Adipogenic Differentiation. *Scientifica (Cairo).* **2013**, 684736 (2013).

131. Lacey, D. L., Timms, E. & a;, et. Osteoprotegrin ligand is cytokine that regulates osteoclast differentiation and activation. *Cell* **93**, 165–176 (1998).

132. Saikia, J., Yazdimamaghani, M., Pouya, S., Moghaddam, H. & Ghandehari, H. Differential Protein Adsorption and Cellular Uptake of Silica Nanoparticles Based on Size and Porosity. *ACS Appl. Mater. Interfaces* **8**, 34820–34832 (2016).

133. Monopoli, M. P., Åberg, C., Salvati, A. & Dawson, K. A. Biomolecular coronas provide the biological identity of nanosized materials. *Nat. Nanotechnol.* **7**, 779–786 (2012).

134. Herd, H. *et al.* Nanoparticle geometry and surface orientation influence mode of cellular uptake. *ACS Nano* **7**, 1961–1973 (2013).

135. Rejman, J., Oberle, V., Zuhorn, I. S. & Hoekstra, D. Size-dependent

internalization of particles via the pathways of clathrin-and caveolae-mediated endocytosis. *Biochem. J.* **377**, 159–169 (2004).

136. Thompson, D. W. & Butterworth, J. T. The nature of laponite and its aqueous dispersions. *J. Colloid Interface Sci.* **151**, 236–243 (1992).

137. Reffitt, D. M. *et al.* Orthosilicic acid stimulates collagen type 1 synthesis and osteoblastic differentiation in human osteoblast-like cells in vitro. *Bone* **32**, 127–135 (2003).

138. Han, P., Wu, C. & Xiao, Y. The effect of silicate ions on proliferation, osteogenic differentiation and cell signalling pathways (WNT and SHH) of bone marrow stromal cells. *Biomater. Sci.* **1**, 379–392 (2013).

139. Clément-Lacroix, P. *et al.* Lrp5-independent activation of Wnt signaling by lithium chloride increases bone formation and bone mass in mice. *Proc. Natl. Acad. Sci. U. S. A.* **102**, 17406–17411 (2005).

140. Zhan, F., Phiel, C. J., Spece, L., Gurvich, N. & Klein, P. S. Inhibitory phosphorylation of glycogen synthase kinase-3 (GSK-3) in response to lithium: Evidence for autoregulation of GSK-3. *J. Biol. Chem.* **278**, 33067–33077 (2003).

141. Gregory, C. A. *et al.* Dkk-1-derived synthetic peptides and lithium chloride for the control and recovery of adult stem cells from bone marrow. *J. Biol. Chem.* **280**, 2309–2323 (2005).

142. Wolf, F. I. & Cittadini, A. Magnesium in Cell Proliferation and Differentiation. *Front. Biosci.* **4**, 607–617 (1999).

143. Yoshizawa, S., Brown, A., Barchowsky, A. & Sfeir, C. Magnesium ion

stimulation of bone marrow stromal cells enhances osteogenic activity, simulating the effect of magnesium alloy degradation. *Acta Biomater.* **10**, 2834–2842 (2014).

144. Díaz-Tocados, J. M. *et al.* Magnesium Chloride promotes Osteogenesis through Notch signaling activation and expansion of Mesenchymal Stem Cells. *Sci. Rep.* **7**, 1–12 (2017).

145. Akhilesh K. Gaharwar, Peppas, N. A. & Khademhosseini, A. Nanocomposite hydrogels for biomedical applications. *Biotechnol Bioeng.* **111**, 441–453 (2015).

146. Peak, C. W., Stein, J., Gold, K. A. & Gaharwar, A. K. Nanoengineered Colloidal Inks for 3D Bioprinting. *Langmuir* **34**, 54 (2018).

147. Desimone, M. F. *et al.* Silica–collagen bionanocomposites as three-dimensional scaffolds for fibroblast immobilization. *Acta Biomater.* **6**, 3998–4004 (2010).

148. Pang, Y., Wang, X., Lee, D. & Greisler, H. P. Dynamic quantitative visualization of single cell alignment and migration and matrix remodeling in 3-D collagen hydrogels under mechanical force. *Biomaterials* **32**, 3776–3783 (2011).

149. Hasegawa, T. *et al.* Ultrastructural and biochemical aspects of matrix vesicle-mediated mineralization. *Jpn. Dent. Sci. Rev.* **53**, 34–45 (2017).

150. Ronga, M. *et al.* Clinical applications of growth factors in bone injuries: Experience with BMPs. *Injury* **44**, S34–S39 (2013).

151. Boraiah, S., Paul, O., Hawkes, D., Wickham, M. & Lorich, D. G. Complications of recombinant human BMP-2 for treating complex tibial plateau fractures: A preliminary report. *Clin. Orthop. Relat. Res.* **467**, 3257–3262 (2009).

152. Wong, D. A., Kumar, A., Jatana, S., Ghiselli, G. & Wong, K. Neurologic

impairment from ectopic bone in the lumbar canal: a potential complication of off-label PLIF/TLIF use of bone morphogenetic protein-2 (BMP-2). *Spine J.* **8**, 1011–1018 (2008).

153. Robin, B. N. *et al.* Cytokine-Mediated Inflammatory Reaction Following Posterior Cervical Decompression and Fusion Associated With Recombinant Human Bone Morphogenetic Protein-2. *Spine (Phila. Pa. 1976).* **35**, E1350–E1354 (2010).

154. Lin, D. *et al.* Rapid initiation of guided bone regeneration driven by spatiotemporal delivery of IL-8 and BMP-2 from hierarchical MBG-based scaffold. *Biomaterials* **196**, 122–137 (2019).

155. Gilde, F. *et al.* Stiffness-dependent cellular internalization of matrix-bound BMP-2 and its relation to Smad and non-Smad signaling. *Acta Biomater.* **46**, 55–67 (2016).

156. Park, S. H. *et al.* BMP2-modified injectable hydrogel for osteogenic differentiation of human periodontal ligament stem cells. *Sci. Rep.* **7**, 6603 (2017).

157. Tabisz, B. *et al.* Site-Directed Immobilization of BMP-2: Two Approaches for the Production of Innovative Osteoinductive Scaffolds. *Biomacromolecules* **18**, 695–708 (2017).

158. Zouani, O. F., Rami, L., Lei, Y. & Durrieu, M. C. Insights into the osteoblast precursor differentiation towards mature osteoblasts induced by continuous BMP-2 signaling. *Biol. Open* **2**, 872–881 (2013).

159. Jivan, F. & Alge, D. L. Bio-Orthogonal, Site-Selective Conjugation of

Recombinant Proteins to Microporous Annealed Particle Hydrogels for Tissue Engineering. *Adv. Ther.* **3**, 1900148 (2020).

160. Cross, L. M., Carrow, J. K., Ding, X., Singh, K. A. & Gaharwar, A. K. Sustained and Prolonged Delivery of Protein Therapeutics from Two-Dimensional Nanosilicates. *ACS Appl. Mater. Interfaces* **11**, 6741–6750 (2019).

161. Wozney, J. M. The Bone Morphogenetic Protein Family Osteogenesis. *Mol. Reprod. Dev.* **32**, 160–167 (1992).

162. Yang, J. *et al.* Bone morphogenetic proteins: Relationship between molecular structure and their osteogenic activity. *Food Sci. Hum. Wellness* **3**, 127–135 (2014).

163. Sedlmeier, G. & Sleeman, J. P. Extracellular regulation of BMP signaling: welcome to the matrix. *Biochem. Soc. Trans.* **45**, 173–181 (2017).

164. Kisiel, M. *et al.* Complexation and Sequestration of BMP-2 from an ECM Mimetic Hyaluronan Gel for Improved Bone Formation. *PLoS One* **8**, 1–13 (2013).

165. Pohl, T. L. M., Boergermann, J. H., Schwaerzer, G. K., Knaus, P. & Cavalcanti-Adam, E. A. Surface immobilization of bone morphogenetic protein 2 via a self-assembled monolayer formation induces cell differentiation. *Acta Biomater.* **8**, 772–780 (2012).

166. Hullinger, T. G., Pan, Q., Viswanathan, H. L. & Somerman, M. J. TGFβ and BMP-2 activation of the OPN promoter: Roles of Smad- and Hox-binding elements. *Exp. Cell Res.* **262**, 69–74 (2001).

167. Bord, S., Horner, A., Hembry, R. M. & Compston, J. E. Stromelysin-1 (MMP-3) and stromelysin-2 (MMP-10) expression in developing human bone: Potential roles in skeletal development. *Bone* **23**, 7–12 (1998).

168. Tamamura, Y. *et al.* Developmental regulation of Wnt/β-catenin signals is required for growth plate assembly, cartilage integrity, and endochondral ossification. *J. Biol. Chem.* **280**, 19185–19195.

169. Bord, S., Horner, A., Beeton, C. A., Hembry, R. M. & Compston, J. E. Tissue inhibitor of matrix metalloproteinase-1 (TIMP-1) distribution in normal and pathological human bone. *Bone* **24**, 229–235 (1999).

170. Jiang, J., Nicoll, S. B. & Lu, H. H. Co-culture of osteoblasts and chondrocytes modulates cellular differentiation in vitro. *Biochem. Biophys. Res. Commun.* **338**, 762–770 (2005).

171. Nakaoka, R., Hsiong, S. X. & Mooney, D. J. Regulation of Chondrocyte Differentiation Level via Co-culture with Osteoblasts. *Tissue Eng.* **12**, 2425–2433 (2006).

172. Giovannini, S. *et al.* Micromass co-culture of human articular chondrocytes and human bone marrow mesenchymal stem cells to investigate stable neocartilage tissue formation in vitro. *Eur. Cells Mater.* **20**, 245–259 (2010).

173. Golub, E. E. Role of matrix vesicles in biomineralization. *Biochim. Biophys. Acta* **1790**, 1592–1598 (2009).

174. Decaris, M. L., Mojadedi, A., Bhat, A. & Leach, J. K. Transferable cell-secreted extracellular matrices enhance osteogenic differentiation. *Acta Biomater.* **8**, 744–

752 (2012).

175. Liu, Q. *et al.* Covalent attachment of P15 peptide to titanium surfaces enhances cell attachment, spreading, and osteogenic gene expression. *J. Orthop. Res.* **30**, 1626–1633 (2012).

176. Shekaran, A. & García, A. J. Extracellular matrix-mimetic adhesive biomaterials for bone repair. *J. Biomed. Mater. Res. Part A* **96A**, 261–272 (2011).

177. Pountos, I. *et al.* The role of peptides in bone healing and regeneration: A systematic review. *BMC Med.* **14**, 103 (2016).

178. Shadish, J. A. & Deforest, C. A. Site-Selective Protein Modification : From Functionalized Proteins to Functional Biomaterials. *Matter* **2**, 50–77 (2020).

179. Hatzenpichler, R. *et al.* In situ visualization of newly synthesized proteins in environmental microbes using amino acid tagging and click chemistry. *Environ. Microbiol.* **16**, 2568–2590 (2014).

180. Dieterich, D. C., Link, A. J., Graumann, J., Tirrell, D. A. & Schuman, E. M. Selective identification of newly synthesized proteins in mammalian cells using bioorthogonal noncanonical amino acid tagging (BONCAT). *Proc. Natl. Acad. Sci. U. S. A.* **103**, 9482–9487 (2006).

181. Kiick, K. L., Saxon, E., Tirrell, D. A. & Bertozzi, C. R. Incorporation of azides into recombinant proteins for chemoselective modification by the Staudinger ligation. *Proc. Natl. Acad. Sci. U. S. A.* **99**, 19–24 (2002).

182. Loebel, C. *et al.* Metabolic Labeling to Probe the Spatiotemporal Accumulation of Matrix at the Chondrocyte–Hydrogel Interface. *Adv. Funct. Mater.* **1909802**, 1–10

(2020).

183. Nichol, J. W. *et al.* Cell-laden microengineered gelatin methacrylate hydrogels. *Biomaterials* **31**, 5536–5544 (2010).

184. McNeill, E. P. *et al.* Three-dimensional in vitro modeling of malignant bone disease recapitulates experimentally accessible mechanisms of osteoinhibition. *Cell Death Dis.* **9**, (2018).

185. Yue, K. *et al.* Synthesis, properties, and biomedical applications of gelatin methacryloyl (GelMA) hydrogels. *Biomaterials* **73**, 254–271 (2015).

186. Gao, Q. *et al.* 3D printing of complex GelMA-based scaffolds with nanoclay. *Biofabrication* **11**, 035006 (2019).

187. Dvorakova, V. *et al.* An advanced conjugation strategy for the preparation of quantum dot-antibody immunoprobes. *Anal. Methods* **9**, 1991–1997 (2017).

188. Liu, E. Y., Jung, S. & Yi, H. Improved Protein Conjugation with Uniform, Macroporous Poly(acrylamide-co-acrylic acid) Hydrogel Microspheres via EDC/NHS Chemistry. *Langmuir* **32**, 11043–11054 (2016).

189. Meghani, N. M. *et al.* Design and evaluation of clickable gelatin-oleic nanoparticles using fattigation-platform for cancer therapy. *Int. J. Pharm.* **545**, 101–112 (2018).

190. Toyo'oka, T. Fluorescent tagging of physiologically important carboxylic acids, including fatty acids, for their detection in liquid chromatography. *Anal. Chim. Acta* **465**, 111–130 (2002).

191. Erdmann, I. *et al.* Cell-selective labelling of proteomes in Drosophila

melanogaster. *Nat. Commun.* **6**, (2015).

192. Saleh, A. M., Jacobson, K. R., Kinzer-Ursem, T. L. & Calve, S. Dynamics of Non-Canonical Amino Acid-Labeled Intra- and Extracellular Proteins in the Developing Mouse. *Cell. Mol. Bioeng.* **12**, 495–509 (2019).

193. Gentleman, E. *et al.* Comparative materials differences revealed in engineered bone as a function of cell-specific differentiation. *Nat. Mater.* **8**, 763–770 (2009).

194. Yang, S. T., Lim, S. I., Kiessling, V., Kwon, I. & Tamm, L. K. Site-specific fluorescent labeling to visualize membrane translocation of a myristoyl switch protein. *Sci. Rep.* **6**, 1–13 (2016).

195. Wang, L., Brock, A., Herberich, B. & Schultz, P. G. Expanding the genetic code of Escherichia coli. *Science* **292**, 498–500 (2001).

196. Sletten, E. M. & Bertozzi, C. R. Bioorthogonal chemistry: Fishing for selectivity in a sea of functionality. *Angew. Chemie - Int. Ed.* **48**, 6974–6998 (2009).

197. Zhang, X., Lu, W., Kwan, K., Bhattacharyya, D. & Wei, Y. Dual-Functional-Tag-Facilitated Protein Labeling and Immobilization. *ACS Omega* **2**, 522–528 (2017).

198. Osugi, M. *et al.* Conditioned Media from Mesenchymal Stem Cells Enhanced Bone Regeneration in Rat Calvarial Bone Defects. *Tissue Eng. - Part A* **18**, 1479–1489 (2012).

199. Sriramulu, S. *et al.* Concise review on clinical applications of conditioned medium derived from human umbilical cord-mesenchymal stem cells (UC-MSCS). *Int. J. Hematol. Stem Cell Res.* **12**, 229–233 (2018).

200. Hofer, H. R. & Tuan, R. S. Secreted trophic factors of mesenchymal stem cells

support neurovascular and musculoskeletal therapies. *Stem Cell Res. Ther.* **7**, 1–14 (2016).

201. Fu, Y. *et al.* Trophic Effects of Mesenchymal Stem Cells in Tissue Regeneration. *Tissue Eng. Part B Rev.* **23**, 515–528 (2017).

APPENDIX A

A.1 Supplementary Figures and Tables for Section 2

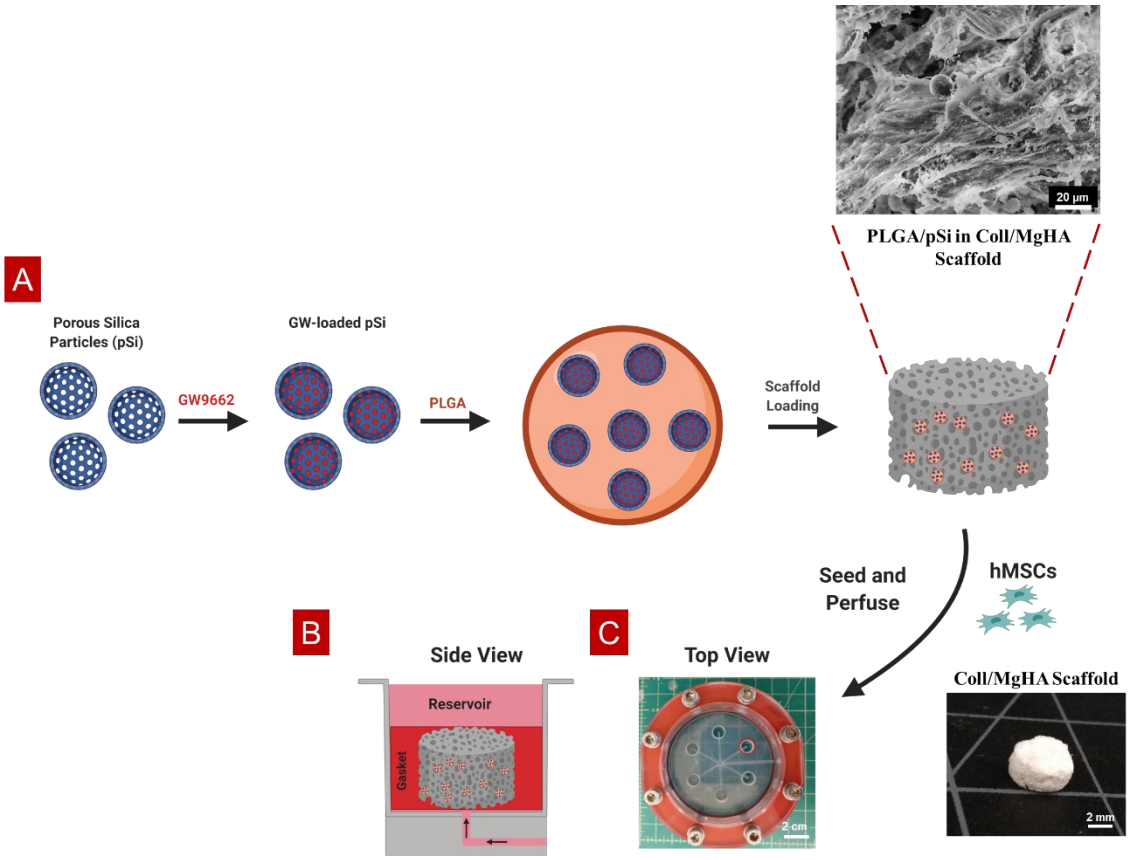

Figure Appendix 1: (A) Schematic illustrating the fabrication of PLGA/pSi microspheres in Coll/MgHA scaffolds. (B) Cross sectional diagram indicates culture media flows from bottom to top through a porous scaffold, as indicated by the arrows. (C) Top view of the perfusion bioreactor, which is capable of culturing six constructs simultaneously.

Target	Sequence
Human GAPDH	Forward: ctctctgctcctcctgttcgac Reverse: tgagcgatgtggctcggct
Human Collagen VI	Forward: ccatcgtgcgcagcc Reverse: tgcgccgactcgtgc
Human Collagen XII	Forward: cttccattgaggcagaagtt Reverse: agacacaagagcagcaatga
Human BMP2	Forward: cccagcgtgaaaagagagac Reverse: gagaccgcagtccgtctaag
Human ALP	Forward: gacccttgacccccacaat Reverse: gctcgtactgcatgtcccct
Human OCN	Forward: tcacactcctcgccctattg Reverse: ctcttcactacctcgctgcc
Human OPN	Forward: catcacctgtgccataccagtt Reverse: ttggaagggtctgtggggcta

Table Appendix 1: Primer sequences utilized for qRT-PCR analysis.

Scaffold/Culture Condition	DF	Variance	χ^2	P Value
CCM/Static	7	6.44E+09	10.7985	0.14765
DMSO/Static		4.45E+09		
pSi/Static		3.45E+09		
GW/Static		6.57E+07		
CCM/Perfused		9.40E+08		
DMSO/Perfused		1.03E+09		
pSi/Perfused		1.19E+08		
GW/Perfused		2.05E+09		

Table Appendix 2: Bartlett's test for homogeneity of variances on calculated cell number for all scaffold and media formulations.

ANOVA table	SS	DF	MS	F (DFn, DFd)	P value
Interaction	2015562891	3	671854297	F (3, 16) = 0.4348	P=0.7311
Scaffold/Culture Media	185357046568	3	61785682189	F (3, 16) = 39.99	P<0.0001
Perfusion	51029447337	1	51029447337	F (1, 16) = 33.03	P<0.0001
Residual	24722643661	16	1545165229		

Table Appendix 3: Two-way ANOVA table for the calculated cell number for all scaffold and media formulations.

Tukey's multiple comparisons test	Mean 1	Mean 2	Mean Diff.	95.00% CI of diff.	Adjusted P Value
DMSO:Static vs. DMSO:Perfused	84268	146683	-62415	-173534 to 48704	0.5430
DMSO:Static vs. pSi:Static	84268	163278	-79010	-190129 to 32109	0.2778
DMSO:Static vs. pSi:Perfused	84268	269831	-185563	-296682 to -74444	0.0006
DMSO:Static vs. GW:Static	84268	132434	-48166	-159285 to 62953	0.7966
DMSO:Static vs. GW:Perfused	84268	240461	-156193	-267312 to -45074	0.0033
DMSO:Static vs. CCM:Static	84268	311292	-227024	-338143 to -115905	<0.0001
DMSO:Static vs. CCM:Perfused	84268	403185	-318917	-430036 to -207799	<0.0001
DMSO:Perfused vs. pSi:Static	146683	163278	-16595	-127714 to 94524	0.9994
DMSO:Perfused vs. pSi:Perfused	146683	269831	-123148	-234266 to -12029	0.0245
DMSO:Perfused vs. GW:Static	146683	132434	14249	-96870 to 125368	0.9998
DMSO:Perfused vs. GW:Perfused	146683	240461	-93778	-204896 to 17341	0.1325
DMSO:Perfused vs. CCM:Static	146683	311292	-164609	-275727 to -53490	0.0020
DMSO:Perfused vs. CCM:Perfused	146683	403185	-256502	-367621 to -145383	<0.0001
pSi:Static vs. pSi:Perfused	163278	269831	-106553	-217672 to 4566	0.0651
pSi:Static vs. GW:Static	163278	132434	30844	-80275 to 141963	0.9739
pSi:Static vs. GW:Perfused	163278	240461	-77183	-188302 to 33936	0.3020
pSi:Static vs. CCM:Static	163278	311292	-148014	-259133 to -36895	0.0054
pSi:Static vs. CCM:Perfused	163278	403185	-239907	-351026 to -128789	<0.0001
pSi:Perfused vs. GW:Static	269831	132434	137397	26278 to 248515	0.0104
pSi:Perfused vs. GW:Perfused	269831	240461	29370	-81749 to 140489	0.9800
pSi:Perfused vs. CCM:Static	269831	311292	-41461	-152580 to 69658	0.8892
pSi:Perfused vs. CCM:Perfused	269831	403185	-133355	-244473 to -22236	0.0132
GW:Static vs. GW:Perfused	132434	240461	-108027	-219145 to 3092	0.0598
GW:Static vs. CCM:Static	132434	311292	-178858	-289976 to -67739	0.0009
GW:Static vs. CCM:Perfused	132434	403185	-270751	-381870 to -159632	<0.0001
GW:Perfused vs. CCM:Static	240461	311292	-70831	-181950 to 40288	0.3967
GW:Perfused vs. CCM:Perfused	240461	403185	-162725	-273843 to -51606	0.0022
CCM:Static vs. CCM:Perfused	311292	403185	-91894	-203012 to 19225	0.1464

Table Appendix 4: Tukey-multiple comparison results between calculated cell number for all scaffold and media formulations.

Gene	DF	Variances of Ct							χ^2	P Value
		CCM Monolayer	DMSO Static	pSi Static	GW Static	DMSO Perfused	pSi Perfused	GW Perfused		
GAPDH (Day 8)	6	0.040915	0.043722	0.012726	0.008238	0.027559	0.001815	0.00081	8.4176	0.20905
Coll VI (Day 8)	6	0.091026	0.003855	0.022544	0.04407	0.048581	0.187793	0.04922	5.69369	0.45836
Coll XII (Day 8)	6	0.925951	0.062559	0.094248	0.190015	0.151693	0.580326	0.47209	4.76457	0.57434
ALP (Day 8)	6	0.109881	0.053793	0.010559	0.008893	0.027848	0.030492	0.05182	3.81929	0.70111
BMP2 (Day 8)	6	0.332015	0.026678	0.104059	0.4476	0.004559	0.15927	0.017878	10.3546	0.11049
GAPDH (Day 21)	6	0.058337	0.000144	0.040959	0.041181	0.098233	0.006381	0.026181	10.8626	0.09272
OPN (Day 21)	6	0.006004	0.021264	0.320164	0.035093	0.118517	0.229544	0.071987	7.76493	0.25584
OCN (Day 21)	6	1.578033	0.129744	1.605737	0.060859	0.146293	0.15957	0.037544	11.1802	0.08296

Table Appendix 5: Bartlett's test for homogeneity of variances for the C_T values for all genes/times points.

ANOVA table	SS	DF	MS	F (DFn, DFd)	P value
Interaction	0.6261	2	0.3131	F (2, 12) = 6.567	P=0.0118
Presence/Source of GW	1.981	2	0.9903	F (2, 12) = 20.77	P=0.0001
Perfusion	4.688	1	4.688	F (1, 12) = 98.34	P<0.0001
Residual	0.5720	12	0.04767		

Table Appendix 6: Two-way ANOVA table results for the Coll VI $\Delta\Delta C_T$ values.

Tukey's multiple comparisons test	Mean 1	Mean 2	Mean Diff.	95.00% CI of diff.	Adjusted P Value
DMSO:Static vs. DMSO:Perfused	-0.9200	-2.326	1.406	0.8072 to 2.005	<0.0001
DMSO:Static vs. pSi:Static	-0.9200	-1.360	0.4400	-0.1588 to 1.039	0.1951
DMSO:Static vs. pSi:Perfused	-0.9200	-2.500	1.580	0.9812 to 2.179	<0.0001
DMSO:Static vs. GW:Static	-0.9200	-2.170	1.250	0.6512 to 1.849	0.0001
DMSO:Static vs. GW:Perfused	-0.9200	-2.686	1.766	1.167 to 2.365	<0.0001
DMSO:Perfused vs. pSi:Static	-2.326	-1.360	-0.9660	-1.565 to -0.3672	0.0014
DMSO:Perfused vs. pSi:Perfused	-2.326	-2.500	0.1740	-0.4248 to 0.7728	0.9115
DMSO:Perfused vs. GW:Static	-2.326	-2.170	-0.1560	-0.7548 to 0.4428	0.9417
DMSO:Perfused vs. GW:Perfused	-2.326	-2.686	0.3600	-0.2388 to 0.9588	0.3691
pSi:Static vs. pSi:Perfused	-1.360	-2.500	1.140	0.5412 to 1.739	0.0003
pSi:Static vs. GW:Static	-1.360	-2.170	0.8100	0.2112 to 1.409	0.0060
pSi:Static vs. GW:Perfused	-1.360	-2.686	1.326	0.7272 to 1.925	<0.0001
pSi:Perfused vs. GW:Static	-2.500	-2.170	-0.3300	-0.9288 to 0.2688	0.4549
pSi:Perfused vs. GW:Perfused	-2.500	-2.686	0.1860	-0.4128 to 0.7848	0.8873
GW:Static vs. GW:Perfused	-2.170	-2.686	0.5160	-0.08280 to 1.115	0.0990

Table Appendix 7: Tukey-multiple comparison results between $\Delta\Delta C_T$ for Coll VI.

ANOVA table	SS	DF	MS	F (DFn, DFd)	P value
Interaction	3.739	2	1.869	F (2, 12) = 10.36	P=0.0024
Presence/Source of GW	8.110	2	4.055	F (2, 12) = 22.47	P<0.0001
Perfusion	7.805	1	7.805	F (1, 12) = 43.24	P<0.0001
Residual	2.166	12	0.1805		

Table Appendix 8: Two-way ANOVA table results for the Coll XII $\Delta\Delta C_T$ values.

Tukey's multiple comparisons test	Mean 1	Mean 2	Mean Diff.	95.00% CI of diff.	Adjusted P Value
DMSO:Static vs. DMSO:Perfused	-2.602	-2.530	-0.07200	-1.237 to 1.093	>0.9999
DMSO:Static vs. pSi:Static	-2.602	-4.740	2.138	0.9729 to 3.303	0.0005
DMSO:Static vs. pSi:Perfused	-2.602	-3.090	0.4880	-0.6771 to 1.653	0.7230
DMSO:Static vs. GW:Static	-2.602	-5.169	2.567	1.402 to 3.732	<0.0001
DMSO:Static vs. GW:Perfused	-2.602	-2.940	0.3380	-0.8271 to 1.503	0.9176
DMSO:Perfused vs. pSi:Static	-2.530	-4.740	2.210	1.045 to 3.375	0.0004
DMSO:Perfused vs. pSi:Perfused	-2.530	-3.090	0.5600	-0.6051 to 1.725	0.6052
DMSO:Perfused vs. GW:Static	-2.530	-5.169	2.639	1.474 to 3.804	<0.0001
DMSO:Perfused vs. GW:Perfused	-2.530	-2.940	0.4100	-0.7551 to 1.575	0.8371
pSi:Static vs. pSi:Perfused	-4.740	-3.090	-1.650	-2.815 to -0.4849	0.0048
pSi:Static vs. GW:Static	-4.740	-5.169	0.4290	-0.7361 to 1.594	0.8114
pSi:Static vs. GW:Perfused	-4.740	-2.940	-1.800	-2.965 to -0.6349	0.0024
pSi:Perfused vs. GW:Static	-3.090	-5.169	2.079	0.9139 to 3.244	0.0007
pSi:Perfused vs. GW:Perfused	-3.090	-2.940	-0.1500	-1.315 to 1.015	0.9976
GW:Static vs. GW:Perfused	-5.169	-2.940	-2.229	-3.394 to -1.064	0.0004

Table Appendix 9: Tukey-multiple comparison results between $\Delta\Delta C_T$ for Coll XII.

ANOVA table	SS	DF	MS	F (DFn, DFd)	P value
Interaction	0.02014	2	0.01007	F (2, 12) = 0.1161	P=0.8914
Presence/Source of GW	5.275	2	2.638	F (2, 12) = 30.41	P<0.0001
Perfusion	5.438	1	5.438	F (1, 12) = 62.71	P<0.0001
Residual	1.041	12	0.08673		

Table Appendix 10: Two-way ANOVA table results for the ALP $\Delta\Delta C_T$ values.

Tukey's multiple comparisons test	Mean 1	Mean 2	Mean Diff.	95.00% CI of diff.	Adjusted P Value
DMSO:Static vs. DMSO:Perfused	-2.278	-3.454	1.176	0.3683 to 1.984	0.0039
DMSO:Static vs. pSi:Static	-2.278	-3.294	1.016	0.2083 to 1.824	0.0116
DMSO:Static vs. pSi:Perfused	-2.278	-4.307	2.029	1.221 to 2.837	<0.0001
DMSO:Static vs. GW:Static	-2.278	-1.964	-0.3140	-1.122 to 0.4937	0.7769
DMSO:Static vs. GW:Perfused	-2.278	-3.073	0.7950	-0.01267 to 1.603	0.0546
DMSO:Perfused vs. pSi:Static	-3.454	-3.294	-0.1600	-0.9677 to 0.6477	0.9826
DMSO:Perfused vs. pSi:Perfused	-3.454	-4.307	0.8530	0.04533 to 1.661	0.0364
DMSO:Perfused vs. GW:Static	-3.454	-1.964	-1.490	-2.298 to -0.6823	0.0005
DMSO:Perfused vs. GW:Perfused	-3.454	-3.073	-0.3810	-1.189 to 0.4267	0.6224
pSi:Static vs. pSi:Perfused	-3.294	-4.307	1.013	0.2053 to 1.821	0.0118
pSi:Static vs. GW:Static	-3.294	-1.964	-1.330	-2.138 to -0.5223	0.0014
pSi:Static vs. GW:Perfused	-3.294	-3.073	-0.2210	-1.029 to 0.5867	0.9341
pSi:Perfused vs. GW:Static	-4.307	-1.964	-2.343	-3.151 to -1.535	<0.0001
pSi:Perfused vs. GW:Perfused	-4.307	-3.073	-1.234	-2.042 to -0.4263	0.0026
GW:Static vs. GW:Perfused	-1.964	-3.073	1.109	0.3013 to 1.917	0.0061

Table Appendix 11: Tukey-multiple comparison results between $\Delta\Delta C_T$ for ALP.

ANOVA table	SS	DF	MS	F (DFn, DFd)	P value
Interaction	13.19	2	6.595	F (2, 12) = 71.24	P<0.0001
Presence/Source of GW	0.4836	2	0.2418	F (2, 12) = 2.612	P=0.1144
Perfusion	0.03125	1	0.03125	F (1, 12) = 0.3375	P=0.5720
Residual	1.111	12	0.09258		

Table Appendix 12: Two-way ANOVA table results for the BMP2 $\Delta\Delta C_T$ values.

Tukey's multiple comparisons test	Mean 1	Mean 2	Mean Diff.	95.00% CI of diff.	Adjusted P Value
DMSO:Static vs. DMSO:Perfused	-5.330	-7.580	2.250	1.416 to 3.084	<0.0001
DMSO:Static vs. pSi:Static	-5.330	-7.170	1.840	1.006 to 2.674	<0.0001
DMSO:Static vs. pSi:Perfused	-5.330	-6.480	1.150	0.3155 to 1.984	0.0059
DMSO:Static vs. GW:Static	-5.330	-7.410	2.080	1.246 to 2.914	<0.0001
DMSO:Static vs. GW:Perfused	-5.330	-5.600	0.2700	-0.5645 to 1.104	0.8776
DMSO:Perfused vs. pSi:Static	-7.580	-7.170	-0.4100	-1.244 to 0.4245	0.5845
DMSO:Perfused vs. pSi:Perfused	-7.580	-6.480	-1.100	-1.934 to -0.2655	0.0083
DMSO:Perfused vs. GW:Static	-7.580	-7.410	-0.1700	-1.004 to 0.6645	0.9804
DMSO:Perfused vs. GW:Perfused	-7.580	-5.600	-1.980	-2.814 to -1.146	<0.0001
pSi:Static vs. pSi:Perfused	-7.170	-6.480	-0.6900	-1.524 to 0.1445	0.1295
pSi:Static vs. GW:Static	-7.170	-7.410	0.2400	-0.5945 to 1.074	0.9202
pSi:Static vs. GW:Perfused	-7.170	-5.600	-1.570	-2.404 to -0.7355	0.0004
pSi:Perfused vs. GW:Static	-6.480	-7.410	0.9300	0.09551 to 1.764	0.0262
pSi:Perfused vs. GW:Perfused	-6.480	-5.600	-0.8800	-1.714 to -0.04551	0.0367
GW:Static vs. GW:Perfused	-7.410	-5.600	-1.810	-2.644 to -0.9755	0.0001

Table Appendix 13: Tukey-multiple comparison results between $\Delta\Delta C_T$ for BMP2.

ANOVA table	SS	DF	MS	F (DFn, DFd)	P value
Interaction	0.08392	2	0.04196	F (2, 12) = 0.3769	P=0.6938
Presence/Source of GW	3.637	2	1.818	F (2, 12) = 16.33	P=0.0004
Perfusion	4.107	1	4.107	F (1, 12) = 36.89	P<0.0001
Residual	1.336	12	0.1113		

Table Appendix 14: Two-way ANOVA table results for the OPN $\Delta\Delta C_T$ values.

Tukey's multiple comparisons test	Mean 1	Mean 2	Mean Diff.	95.00% CI of diff.	Adjusted P Value
DMSO:Static vs. DMSO:Perfused	-2.003	-2.801	0.7980	-0.1170 to 1.713	0.1016
DMSO:Static vs. pSi:Static	-2.003	-2.682	0.6790	-0.2360 to 1.594	0.2007
DMSO:Static vs. pSi:Perfused	-2.003	-3.619	1.616	0.7010 to 2.531	0.0008
DMSO:Static vs. GW:Static	-2.003	-2.910	0.9070	-0.008046 to 1.822	0.0525
DMSO:Static vs. GW:Perfused	-2.003	-4.041	2.038	1.123 to 2.953	<0.0001
DMSO:Perfused vs. pSi:Static	-2.801	-2.682	-0.1190	-1.034 to 0.7960	0.9975
DMSO:Perfused vs. pSi:Perfused	-2.801	-3.619	0.8180	-0.09705 to 1.733	0.0902
DMSO:Perfused vs. GW:Static	-2.801	-2.910	0.1090	-0.8060 to 1.024	0.9983
DMSO:Perfused vs. GW:Perfused	-2.801	-4.041	1.240	0.3250 to 2.155	0.0067
pSi:Static vs. pSi:Perfused	-2.682	-3.619	0.9370	0.02195 to 1.852	0.0437
pSi:Static vs. GW:Static	-2.682	-2.910	0.2280	-0.6870 to 1.143	0.9545
pSi:Static vs. GW:Perfused	-2.682	-4.041	1.359	0.4440 to 2.274	0.0033
pSi:Perfused vs. GW:Static	-3.619	-2.910	-0.7090	-1.624 to 0.2060	0.1700
pSi:Perfused vs. GW:Perfused	-3.619	-4.041	0.4220	-0.4930 to 1.337	0.6427
GW:Static vs. GW:Perfused	-2.910	-4.041	1.131	0.2160 to 2.046	0.0131

Table Appendix 15: Tukey-multiple comparison results between $\Delta\Delta C_T$ for OPN.

ANOVA table	SS	DF	MS	F (DFn, DFd)	P value
Interaction	7.223	2	3.612	F (2, 12) = 49.19	P<0.0001
Presence/Source of GW	12.42	2	6.210	F (2, 12) = 84.58	P<0.0001
Perfusion	2.431	1	2.431	F (1, 12) = 33.11	P<0.0001
Residual	0.8811	12	0.07342		

Table Appendix 16: Two-way ANOVA table results for the OCN $\Delta\Delta C_T$ values.

Tukey's multiple comparisons test	Mean 1	Mean 2	Mean Diff.	95.00% CI of diff.	Adjusted P Value
DMSO:Static vs. DMSO:Perfused	-1.434	-2.950	1.516	0.7729 to 2.259	0.0002
DMSO:Static vs. pSi:Static	-1.434	-2.217	0.7830	0.03987 to 1.526	0.0369
DMSO:Static vs. pSi:Perfused	-1.434	-3.958	2.524	1.781 to 3.267	<0.0001
DMSO:Static vs. GW:Static	-1.434	-4.748	3.314	2.571 to 4.057	<0.0001
DMSO:Static vs. GW:Perfused	-1.434	-3.696	2.262	1.519 to 3.005	<0.0001
DMSO:Perfused vs. pSi:Static	-2.950	-2.217	-0.7330	-1.476 to 0.01013	0.0540
DMSO:Perfused vs. pSi:Perfused	-2.950	-3.958	1.008	0.2649 to 1.751	0.0067
DMSO:Perfused vs. GW:Static	-2.950	-4.748	1.798	1.055 to 2.541	<0.0001
DMSO:Perfused vs. GW:Perfused	-2.950	-3.696	0.7460	0.002870 to 1.489	0.0489
pSi:Static vs. pSi:Perfused	-2.217	-3.958	1.741	0.9979 to 2.484	<0.0001
pSi:Static vs. GW:Static	-2.217	-4.748	2.531	1.788 to 3.274	<0.0001
pSi:Static vs. GW:Perfused	-2.217	-3.696	1.479	0.7359 to 2.222	0.0003
pSi:Perfused vs. GW:Static	-3.958	-4.748	0.7900	0.04687 to 1.533	0.0350
pSi:Perfused vs. GW:Perfused	-3.958	-3.696	-0.2620	-1.005 to 0.4811	0.8361
GW:Static vs. GW:Perfused	-4.748	-3.696	-1.052	-1.795 to -0.3089	0.0048

Table Appendix 17: Tukey-multiple comparison results between $\Delta\Delta C_T$ for OCN.

Scaffold/Culture Condition	DF	Variance	χ^2	P Value
DMSO/Static	5	2.41E-04	5.59439	0.3477
pSi/Static		1.52E-04		
GW/Static		3.33E-04		
DMSO/Perfused		1.46E-04		
pSi/Perfused		5.72E-05		
GW/Perfused		5.38E-06		

Table Appendix 18: Bartlett's test for homogeneity on variances of bone mineral density (g/cm^3).

ANOVA table	SS	DF	MS	F (DFn, DFd)	P value
Interaction	7.847e-005	2	3.924e-005	F (2, 12) = 0.3776	P=0.6934
Presence/Source of GW	0.01246	2	0.006232	F (2, 12) = 59.98	P<0.0001
Perfusion	0.004984	1	0.004984	F (1, 12) = 47.96	P<0.0001
Residual	0.001247	12	0.0001039		

Table Appendix 19: Two-way ANOVA table results for the bone mineral density (BMD) (g/cm^3) values.

Tukey's multiple comparisons test	Mean 1	Mean 2	Mean Diff.	95.00% CI of diff.	Adjusted P Value
DMSO:Static vs. DMSO:Perfused	0.03501	0.07331	-0.03831	-0.06626 to -0.01035	0.0062
DMSO:Static vs. pSi:Static	0.03501	0.07719	-0.04219	-0.07014 to -0.01423	0.0029
DMSO:Static vs. pSi:Perfused	0.03501	0.1053	-0.07027	-0.09823 to -0.04232	<0.0001
DMSO:Static vs. GW:Static	0.03501	0.1016	-0.06663	-0.09459 to -0.03868	<0.0001
DMSO:Static vs. GW:Perfused	0.03501	0.1351	-0.1001	-0.1280 to -0.07212	<0.0001
DMSO:Perfused vs. pSi:Static	0.07331	0.07719	-0.003880	-0.03184 to 0.02408	0.9965
DMSO:Perfused vs. pSi:Perfused	0.07331	0.1053	-0.03196	-0.05992 to -0.004008	0.0222
DMSO:Perfused vs. GW:Static	0.07331	0.1016	-0.02832	-0.05628 to -0.0003680	0.0464
DMSO:Perfused vs. GW:Perfused	0.07331	0.1351	-0.06177	-0.08972 to -0.03381	<0.0001
pSi:Static vs. pSi:Perfused	0.07719	0.1053	-0.02808	-0.05604 to -0.0001280	0.0487
pSi:Static vs. GW:Static	0.07719	0.1016	-0.02444	-0.05240 to 0.003512	0.1003
pSi:Static vs. GW:Perfused	0.07719	0.1351	-0.05789	-0.08584 to -0.02993	0.0002
pSi:Perfused vs. GW:Static	0.1053	0.1016	0.003640	-0.02432 to 0.03160	0.9974
pSi:Perfused vs. GW:Perfused	0.1053	0.1351	-0.02980	-0.05776 to -0.001848	0.0344
GW:Static vs. GW:Perfused	0.1016	0.1351	-0.03344	-0.06140 to -0.005488	0.0164

Table Appendix 20: Tukey-multiple comparison results for BMD (g/cm^3) values.

Scaffold/Culture Condition	DF	Variance	χ^2	P Value
DMSO/Static	5	7.70E+03	14.704	0.0117
pSi/Static		5.38E+04		
GW/Static		2.16E+05		
DMSO/Perfused		1.63E+04		
pSi/Perfused		9.61E+05		
GW/Perfused		1.19E+04		

Table Appendix 21: Bartlett's test for homogeneity on variances of compressive modulus (KPa).

ANOVA table	SS	DF	MS	F (DFn, DFd)	P value
Interaction	319707	2	159853	F (2, 12) = 0.7578	P=0.4899
Presence/Source of GW	2631396	2	1315698	F (2, 12) = 6.237	P=0.0139
Perfusion	4896900	1	4896900	F (1, 12) = 23.21	P=0.0004
Residual	2531261	12	210938		

Table Appendix 22: Two-way ANOVA table results for the compressive modulus (KPa).

Tukey's multiple comparisons test	Mean 1	Mean 2	Mean Diff.	95.00% CI of diff.	Adjusted P Value
DMSO:Static vs. DMSO:Perfused	779.2	1667	-887.7	-2147 to 371.9	0.2412
DMSO:Static vs. pSi:Static	779.2	1387	-607.9	-1868 to 651.7	0.6013
DMSO:Static vs. pSi:Perfused	779.2	2805	-2026	-3286 to -766.6	0.0017
DMSO:Static vs. GW:Static	779.2	1541	-761.8	-2021 to 497.8	0.3802
DMSO:Static vs. GW:Perfused	779.2	2365	-1585	-2845 to -325.8	0.0116
DMSO:Perfused vs. pSi:Static	1667	1387	279.7	-979.9 to 1539	0.9717
DMSO:Perfused vs. pSi:Perfused	1667	2805	-1139	-2398 to 121.0	0.0854
DMSO:Perfused vs. GW:Static	1667	1541	125.8	-1134 to 1385	0.9993
DMSO:Perfused vs. GW:Perfused	1667	2365	-697.7	-1957 to 561.9	0.4672
pSi:Static vs. pSi:Perfused	1387	2805	-1418	-2678 to -158.7	0.0245
pSi:Static vs. GW:Static	1387	1541	-153.9	-1414 to 1106	0.9981
pSi:Static vs. GW:Perfused	1387	2365	-977.5	-2237 to 282.1	0.1689
pSi:Perfused vs. GW:Static	2805	1541	1264	4.765 to 2524	0.0489
pSi:Perfused vs. GW:Perfused	2805	2365	440.8	-818.8 to 1700	0.8401
GW:Static vs. GW:Perfused	1541	2365	-823.6	-2083 to 436.0	0.3064

Table Appendix 23: Tukey-multiple comparison results for compressive modulus (KPa).

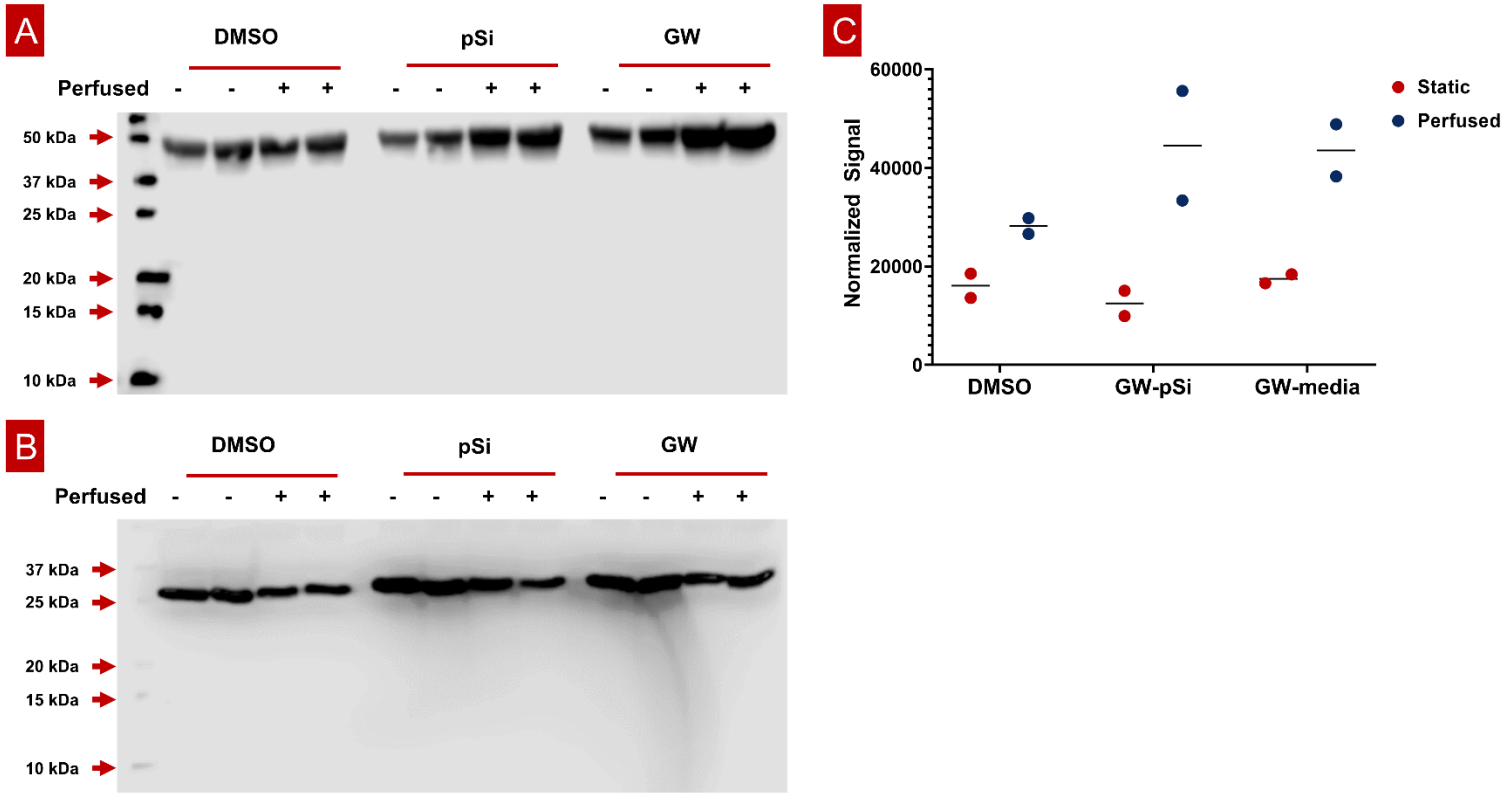

Figure Appendix 2: Immunoblotting of extracted proteins from various hMSCs/scaffolds combinations after 8 days of culture for A) BMP2 and B) GAPDH. C) Densitometric measurement of BMP2 signal normalized to corresponding GAPDH signal.

A.2 Supplementary Figures and Tables for Section 3

ANOVA table	SS	DF	MS	F (DFn, DFd)	P value
nSi Percentage	0.001128	2	0.0005638	F (2, 24) = 31.54	P<0.0001
nSi Pretreatment	0.004021	1	0.004021	F (1, 24) = 225.0	P<0.0001
Silicone Support	0.0007231	1	0.0007231	F (1, 24) = 40.46	P<0.0001
nSi Percentage x nSi Pretreatment	4.506e-005	2	2.253e-005	F (2, 24) = 1.261	P=0.3016
nSi Percentage x Silicone Support	0.0001955	2	9.774e-005	F (2, 24) = 5.468	P=0.0110
nSi Pretreatment x Silicone Support	9.416e-005	1	9.416e-005	F (1, 24) = 5.268	P=0.0308
nSi Percentage x nSi Pretreatment x Silicone Support	6.177e-005	2	3.089e-005	F (2, 24) = 1.728	P=0.1990
Residual	0.0004290	24	1.787e-005		

Table Appendix 24: ANOVA table for three-way analysis of ALP activity of hMSCs after 8 day s of culture in Coll-nSi nanocomposite hydrogels.

ANOVA table	SS	DF	MS	F (DFn, DFd)	P value
nSi Percentage	377.7	2	188.9	F (2, 24) = 87.04	P<0.0001
nSi Pretreatment	86.08	1	86.08	F (1, 24) = 39.67	P<0.0001
Silicone Support	83.46	1	83.46	F (1, 24) = 38.46	P<0.0001
nSi Percentage x nSi Pretreatment	3.175	2	1.587	F (2, 24) = 0.7315	P=0.4916
nSi Percentage x Silicone Support	29.46	2	14.73	F (2, 24) = 6.789	P=0.0046
nSi Pretretment x Silicone Support	8.322	1	8.322	F (1, 24) = 3.835	P=0.0619
nSi Percentage x nSi Pretreatment x Silicone Support	8.478	2	4.239	F (2, 24) = 1.954	P=0.1637
Residual	52.08	24	2.170		

Table Appendix 25: ANOVA table for three-way analysis of ALP activity of hMSCs after 8 day s of culture in Coll-nSi nanocomposite hydrogels.

A.3 Supplementary Figures and Tables for Section 4

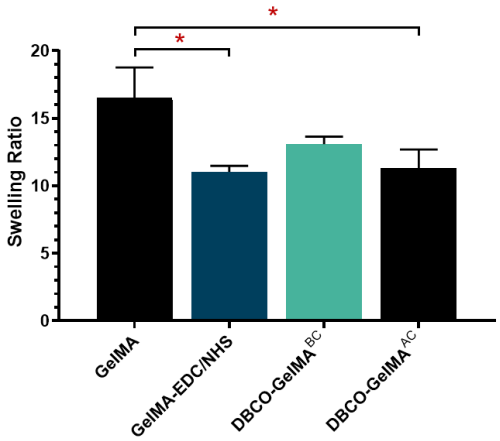

Figure Appendix 3: Hydrogel swelling ratio affected by EDC/NHS chemistry. Statistical analysis was performed by one-way ANOVA, followed by a Tukey's multiple comparison. Error bars depict standard deviation (n=3), and asterisks signify a significant difference ($p<0.05$).

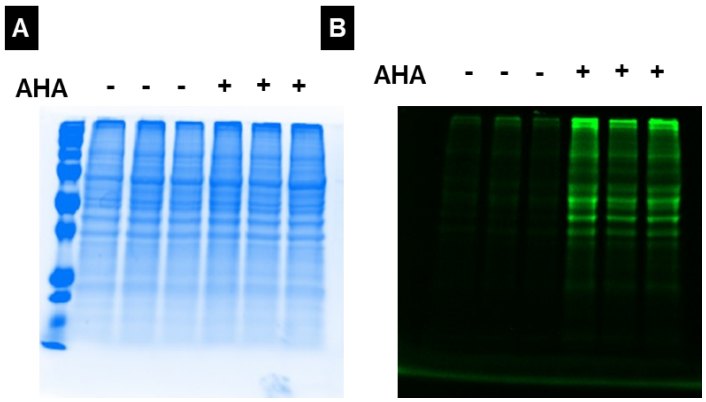

Figure Appendix 4: Coomassie-stain of protein lysates from iP-hMSCs monolayers cultured in the absence (−) or presence (+) of AHA for 10 days show similar band patterns, indicating that AHA does not interfere with the translational machinery. B) iP-hMSCs incorporate AHA intro translated proteins, as indicated by DBCO-488 tag conjugated to proteins containing AHA.

Protein ID	Methionine Content (%)
Coll VI, α1	0.99
Coll VI α2	1.20
Coll VI α3	1.14
Coll VI α4	1.62
Coll VI α5	2.08
Coll VI α6	1.44
Coll XII α1	1.15

Table Appendix 26: Percentage of methionine content for Coll VI and Coll XII subunits. Using the UniProtKB/Swiss-Prot database, the methionine content was calculated by counting the number of methionine residues relative to the number of total amino acids UniProtKB verified subunits, excluding the signal peptide sequence.